Lowe, Rodney William (2004) *Development of a novel rotationally moulded solar hot water system.* Masters (Research) thesis, James Cook University.

DEVELOPMENT OF A NOVEL ROTATIONALLY MOULDED SOLAR HOT WATER SYSTEM

A thesis submitted by

Rodney William Lowe

Bachelor of Engineering (Hons) - Mechanical

Graduate Member – Institution of Engineers Australia

in March, 2004

to fulfil the requirements for the degree of

Master of Engineering Science

in the School of Engineering

James Cook University

Townsville, Australia 4814

STATEMENT OF ACCESS

I, the undersigned, author of this work, understand that James Cook University will make this thesis available for use within the University Library and, via the Australian Digital Theses network, for use elsewhere.

I understand that, as an unpublished work, a thesis has significant protection under the Copyright Act and;

I wish this work to be embargoed until : March 11, 2009

___________________________ _______________

Signature Date

ABSTRACT

The objective of this thesis is to outline the development of a novel rotationally moulded solar water heater. It will describe the underlying principles that make the system unique and conclude with the industrial development of a commercial version of the heater. The solar water heater is of the integral collector-storage type. The most unique feature of the water heater is that the collector glazing system also forms a transparent upper surface of the storage tank. The highly efficient top cover system provides the maximum possible use of available solar radiation, although some penalty is imposed through relatively large night time heat losses. The top cover system is a prime consideration in this thesis and the principles of solar transmission and thermal insulation are discussed in detail. Mains pressure hot water supply is achieved by passing the mains pressure cold water through a finned heat exchange tube that is submerged in the water storage chamber. The water exits the tube at a temperature close to that of the stored heat transfer medium in the collector/storage chamber. Careful consideration was given to design of the heat exchange circuit to optimise extraction of energy from the solar water heater.

The collector is composed of three main components that have been developed to suit manufacturing from plastic using the rotational moulding process. The absorber/storage component houses the heat exchange tube, inner glazing and 150 litres of water which is heated by solar radiation. The top cover houses the upper transparent insulation, the outer glazing and provides additional side insulation. A mounting tray that facilitates permanent attachment of the collector assembly to the roof of a dwelling or suitable intermediate framework is the final component. The heater is now ready for production and is an Australian and New Zealand Standards, AS/NZS 2712-2002 approved system.

ACKNOWLEDGEMENTS

The author wishes to express his sincere gratitude to the following people:

Dr Harry Suehrcke (James Cook University) and Dr Jonathan Harris (Maunsell Australia Pty Ltd), who as supervisors of this project have offered guidance, assistance and constructive criticism.

Mr Andrew Gough, Mr Ian Gough and Mr Simon Gough (Directors of Gough Plastics), who have offered their combined experience and knowledge of the rotational moulding process.

Finally the author would like to thank his family for their continued support and encouragement throughout the course of this thesis.

TABLE OF CONTENTS

LIST OF ILLUSRATIONS AND DIAGRAMS

LIST OF TABLES

STATEMENT OF SOURCES

DECLARATION

I declare that this thesis is my own work and has not been submitted in any form for another degree or diploma at any university or other institution of tertiary education. Information derived from the published or unpublished work of others has been acknowledged in the text and a list of references is given.

Signature　　　　　　　　　　Date

ELECTRONIC COPY

I, the undersigned, the author of this work, declare that the electronic copy of this thesis provided to the James Cook University Library is an accurate copy of the print thesis submitted, within the limits of the technology available.

Signature　　　　　　　　　　Date

ADDITIONAL THESIS INFORMATION

During the course of this thesis the author has contributed to two published conference papers and an international journal article related to the thesis topic:

Suehrcke, H., Lowe, R. W. and Harris, J. A. (2000), *Effect of Wall Emissivity on the Coupled Radiative and Conductive Heat Transfer Across Honeycomb Transparent Insulation*. Proc. 7th Australasian Heat and Mass Transfer Conference, 3-6 July, Townsville, Chalkface Press, Western Australia, pp. 301-307.

Suehrcke, H., Däldehög, D., Harris, J. A. and Lowe, R. W. (2001), *Heat Transfer across Transparent Zigzag Sheets*. Proc. International Solar Energy Society 2001 Solar World Congress, 25-30 November, Adelaide, Published by Australia and New Zealand Solar Energy Society (2003), pp. 2057-2062.

Suehrcke, H., Däldehög, D., Harris, J. A. and Lowe, R. W. (2004), *Heat Transfer across Corrugated Sheets and Honeycomb Transparent Insulation*, Solar Energy, Volume 76, Numbers 1-3, pp. 351 – 358.

1. INTRODUCTION

The provision of domestic hot water is taken for granted in developed countries throughout the world. In Australia, approximately 60% of hot water supply is achieved by electrically heated storage water heaters (Mark Ellis and Associates, 2001), which may account for 25 to 50% of domestic electricity consumption (Australian Green House Office, 2003). Other sources of energy for domestic water heating include gas and solar. The proportion of water heaters using electricity, gas and solar in Australia is shown in Figure 1.1. Alternative energy sources for domestic water heating have been available long before the invention of domestic electricity, but have not been widely adopted due to inconvenience or high cost of implementation. The introduction of the Kyoto Protocol has led many researchers, designers and inventors to develop economically feasible means of using alternative energy sources for domestic water heating.

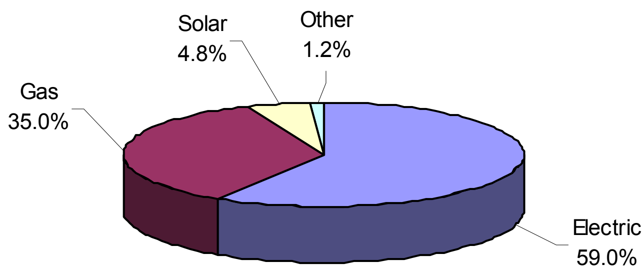

Figure 1.1. Breakdown of energy sources used for domestic water heating. Percentage values taken from Mark Ellis and Associates (2001).

Most commercially available solar water heaters have a separate collector and storage tank that may be either close-coupled or remote from each other. The collector array generally contains only a very small volume of water that is circulated to the storage vessel either by thermosyphon or mechanical pumping. These types of water heaters can be very efficient, but are often expensive and not aesthetically pleasing to many householders. A photograph of a typical close-coupled collector storage solar hot water system may be seen in Figure 1.2.

Figure 1.2. Photograph of a typical close-coupled collector storage solar water heater. Australian and New Zealand Solar Energy Society, 2002

The factors of cost and aesthetics are the two main reasons that solar water heating has not achieved a very large portion of the domestic water heating market in Australia, e.g. less than 6% uptake in Queensland (Mark Ellis and Associates, 2001). Clearly, there is large potential for a cost effective solar water heater that has pleasing aesthetics to achieve wide acceptance by the Australian community. There is also large potential for a low cost solar water heater in the local Asia and Pacific region as well as possibilities of an export market to Europe, where solar water heating is already widely accepted, but very expensive.

The concept of developing an integral collector/storage solar water heater with a transparent upper surface was mooted by Dr Harry Suehrcke of James Cook University in 1995. Suehrcke performed a simple experiment that confirmed increased efficiency in heating a large volume of water. The experiment was conducted using two clear plastic bottles, which were painted black on one side only. A photograph of the experimental bottles may be seen in Figure 1.3.

The two bottles were placed laying down in a metal tray lined with insulation to halfway up the bottles. The bottle with the painted surface below the water body achieved a 38% larger temperature rise when exposed to solar radiation than the bottle with the painted surface above the water body (Suehrcke *et al.,* 2003). Further discussion of the principles underlying the experiment will be given in a later chapter of this thesis.

Figure 1.3. Experimental apparatus used by Suehrcke in 1995

Suehrcke then began to search for the most practical way to proceed with development of this concept. An alliance was struck with Gough Plastics, a Townsville based manufacturer of rotationally moulded products. Gough Plastics' products range from four wheel drive accessories to large volume water storage tanks and also the range of 'Hybrid Toilets', an environmentally sensitive human waste treatment system.

An application was made in 1998 for an AusIndustry START grant to investigate the feasibility of commercially producing a rotationally moulded integral collector storage solar water heater. When the grant was approved, the author was approached to undertake the commercial feasibility study on a full-time basis and also complete this thesis on a part-time basis. During the course of the two year START program it was recognised that with the use of emerging technologies, a very efficient water heater could be developed. Patent searches were performed to ensure that there would be no opposition to releasing the product on the Australian solar water heater market. An application was made to the Australian Greenhouse Office in 2000 for funding under Round 4 of the Renewable Energy Commercialisation Program. The grant was approved for a three year program of industrial development with the goal of reaching volume production at the end of 2003. A patent for an integral collector/storage water heater was applied for in 1998, was modified in 2001, and was granted in 2002. The product has undergone constant transformation as problems were encountered and improvements became apparent. The principle of operation remains the same as with the original prototype, but has been refined to optimise the benefits of, and overcome the limitations of manufacture by, the rotational moulding process.

The objective of this thesis is to document the development of a novel rotationally moulded integral collector/storage solar water heater as follows:

- Realisation of the need for a low cost, high efficiency solar water heater
- A review of integral collector/storage solar water heater technologies
- The development of key components of this solar water heater design
- The principles of operation of this solar water heater design
- The industrial design and development for manufacture of a low cost, mains pressure, integral collector/storage solar water heater with major components produced by rotational moulding

The proposed water heater is based on the principles developed by Suehrcke and has three major components that perform the collection, storage and transfer of energy to the mains pressure potable water supply. The three components are listed below and are shown schematically in Figure 1.4.

- Solar energy absorber and storage chamber - the chamber is filled with heat transfer fluid (water) - insulated on the underside and sides
- Transparent insulation system - allows penetration of solar radiation into the absorber chamber and reduces heat loss to surroundings
- Heat exchange tube – allows mains pressure potable hot water supply to be delivered to the consumer

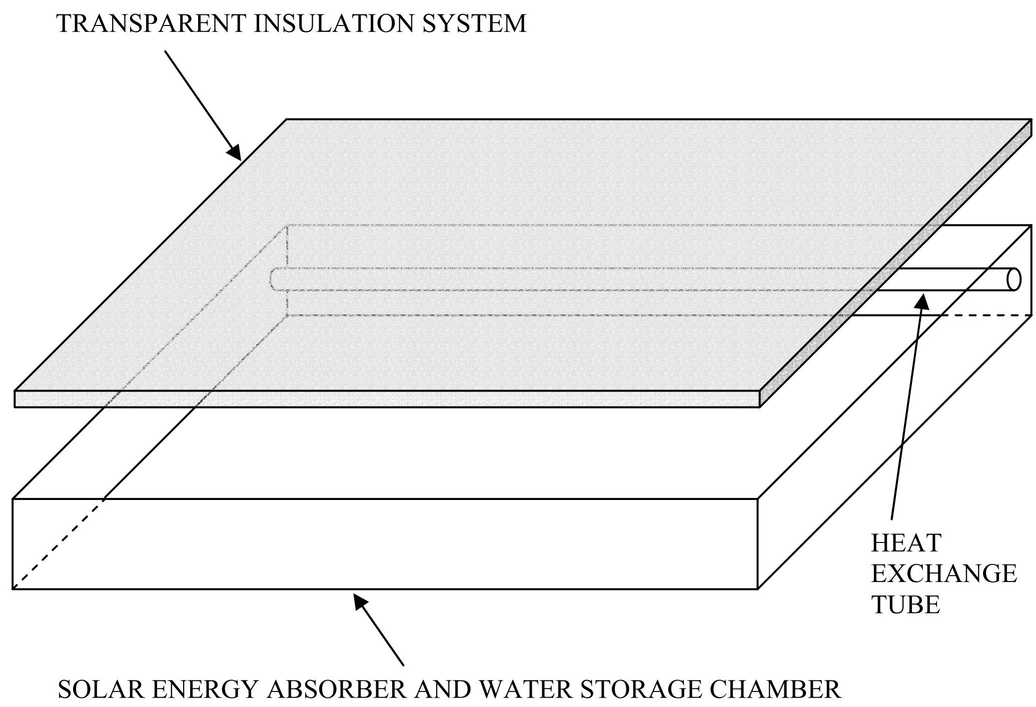

Figure 1.4 Schematic diagram of proposed solar water heater

A detailed discussion of the major components and the principles of operation of the heater are described in subsequent chapters of this thesis.

2. LITERATURE REVIEW

This chapter covers some history of integral collector-storage solar water heaters and introduces the background knowledge acquired during the course of this thesis. The review concentrates on the advantages and limitations of this type of water heater. A general concept for a heater that capitalises on the advantages and reduces the effect of the limitations is discussed. The difference between a traditional solar water heater and an integral collector-storage heater are highlighted in schematic Figure 2.1. The integral collector-storage heater combines the functions of solar collector and storage into a single unit. Unlike conventional solar hot water systems there is no separate solar collector and storage tank.

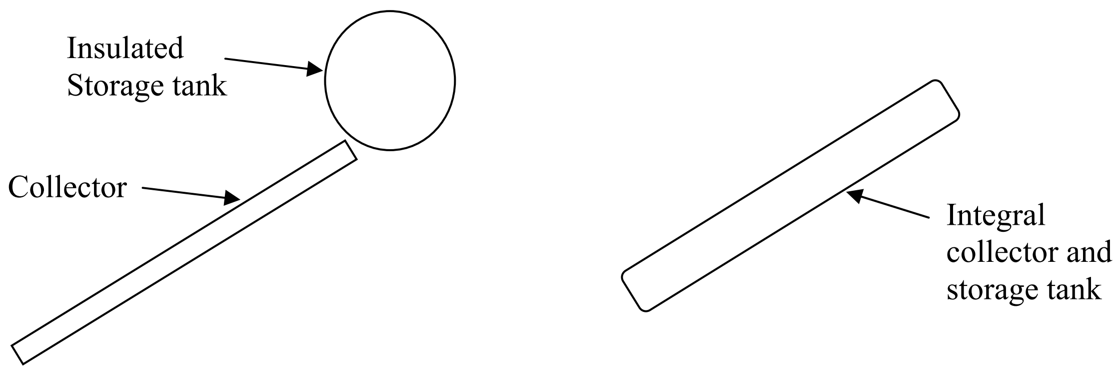

Figure 2.1 Schematic diagram of traditional and integral solar water heaters

2.1. Overview of integral collector/storage solar water heaters

Integral collector-storage water heaters were the first patented solar water heaters to be used, in California, in 1891. The 'CLIMAX' solar water heater, patented by Clarence M. Kemp of Baltimore, consisted of four blackened metal water tanks, lying horizontally, enclosed in a pine box with a single glass top cover. By 1897, 30% of homes in Pasadena, California had solar water heaters. Those collectors were only useful during the afternoon and early evening as the very high heat loss from the top cover caused long warm up periods in the morning and quickly allowed the water to cool to air temperature soon after dusk (Butti and Perlin, 1977).

The development of solar water heaters by various companies saw tremendous growth until the Los Angeles natural gas basin was discovered in the mid 1920's. Sales of solar hot water systems plummeted while the gas storage water heater industry boomed because of the relative low purchase price and running costs. The solar water heater industry was very small, but survived until the American government restricted the use of copper for any non-military purposes at the beginning of World War II. After the war, the solar water heater industry re-kindled itself at reduced capacity because cheap electricity had come to be the common water heating energy source. Many of the solar water heater designs were separate collector and storage types (Butti and Perlin, 1977).

A simple integral collector-storage heater was developed in rural Japan directly after World War II. The heater was a basin in which water was stored, with a glass cover to keep out most of the dust, and placed in the sun. This type of heater spread it presence throughout Japan very quickly, but only provided warm water for bathing. The basin water heater was referred to as a Type 1 heater. (Tanishita, 1970).

Soon afterwards, a solar water heating industry emerged in Japan that provided users with hotter water, free from dust and algae. These were referred to as closed type heaters, and were most commonly of the integral collector-storage type. Two main forms of closed type heater existed, those being a closed membrane type; and the closed type with pipe internals. The closed membrane type consisted of a vinyl membrane pillow into which water was placed and allowed to be heated by the sun. This type of heater has the same disadvantage as the Type 1 heater in that it has to be placed on a horizontal surface, thus limiting its exposure to sunshine during the winter months. The heater also had no facility for mains pressure water delivery, so a suitable site that provided sufficient gravity head was required. The advantage of the heater was its selling price of around $10, even though the life expectancy of the heater was only 2-3 years. The remaining closed type heaters were constructed from tubes, positioned vertically and attached in parallel via manifolds at the top and bottom. The tubes were manufactured from glass, plastic, stainless steel or iron. These integral collector-storage heaters were equipped with a glass outer cover over the tubes to prevent deterioration by the elements and reduce heat loss. The tube heaters could also be tilted towards the sun. (Tanishita, 1970). A diagram of the typical tube construction may be seen in Figure 2.2.

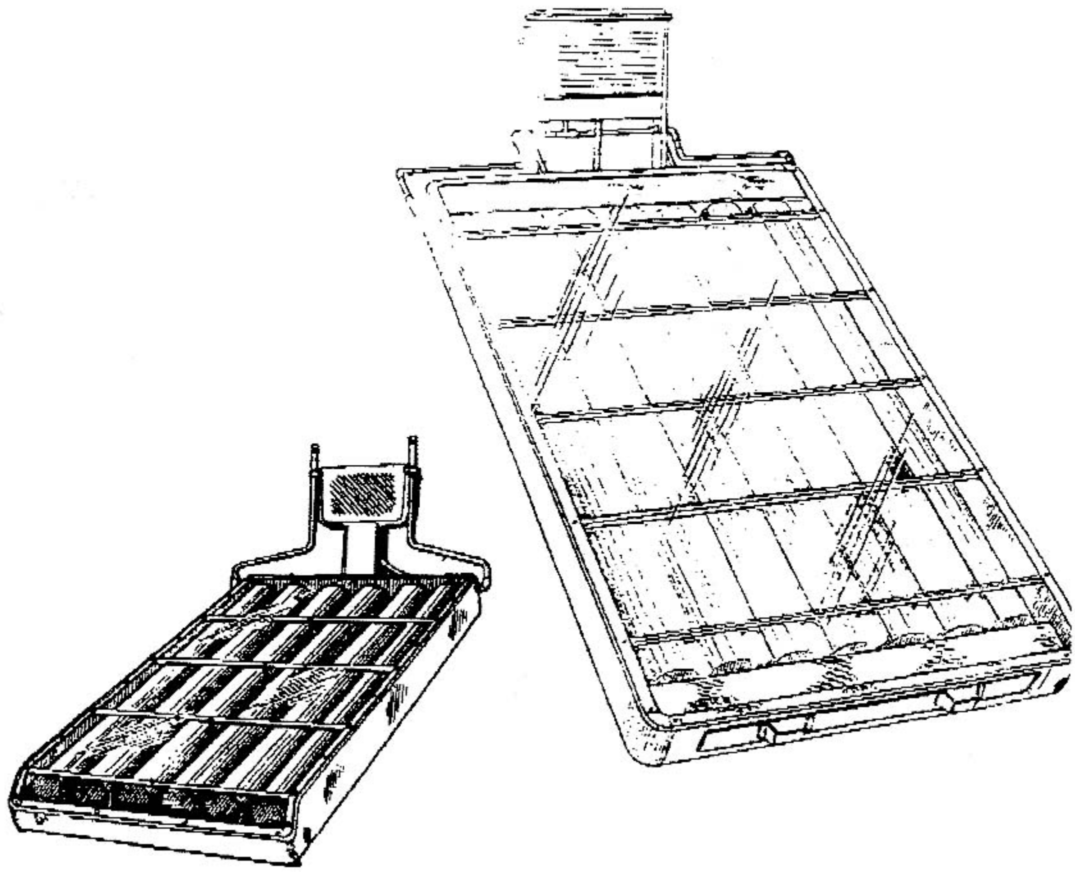

Figure 2.2 Diagram of typical tube type water heaters developed in Japan, (Tanishita, 1970).

The solar water heater industry in Japan reached its peak production in the 1960's after which cheap fuels, such as propane gas and off-peak electricity, provided energy for water heating requirements. The production of closed membrane type heaters peaked at approximately 240 000 installations per year in 1963, while the sum of all other closed type heaters peaked at almost 300 000 installations per year in 1966 (Tanishita, 1970).

Both of the above references indicate that modern technology and fuel prices have restricted the market for integral collector-storage solar water heaters. An Internet search determined there is currently only one integral collector-storage water heater manufactured in Australia, the Solahart 'Hot Top'. A picture of the 'Hot Top' water heater may be seen in Figure 2.3. The limited number of commercially produced integral collector/storage heaters may be explained in the following section of this thesis where the problems associated with integral collector storage heaters are discussed.

Figure 2.3 Picture of a Solahart 'Hot Top' integral collector-storage solar water heater.

2.2 Problems with integral collector/storage solar water heaters

There are numerous thermosyphon, pumped circulation and heat pump water heaters available that take advantage of the sunshine abundant Australian climate. The key to success for all of these heater configurations is the availability of a well insulated hot water storage vessel which is separate to the solar collector (see Figure 2.1). This storage vessel allows energy to be carried over the night period and is available to the user in the morning before the solar collection process has begun with the new day. The ability to collect and store energy from the sun is also possible using an integral collector-storage water heater, however the challenges faced in maintaining the energy collected are more pronounced when the contents are stored directly adjacent to the exposed collector aperture.

The first and foremost challenge facing the solar engineer when considering an integral collector-storage heater is how to reduce the heat loss coefficient of the collector aperture such that useful, unused energy will be maintained at least until the following day. The sides and underside of an integral collector-storage heater may be insulated very well using economic, commercially available processes. At the top surface a balance must be struck between effective collection of solar radiation and effective insulation. As more transparent material is placed between the absorber and its outer glazing, the transmission of solar radiation will naturally trend downwards.

A study of transparent insulation materials was carried out to determine the most cost efficient method of minimising the heat loss from a collector while maximising the energy gained through solar radiation transmission. The most simple of the transparent insulation materials investigated was multiple flat sheets of transparent material, spaced parallel to the absorber surface. A detailed analysis of the multiple parallel transparent sheet insulation is given by Duffie and Beckman (1991).

Another material worthy of consideration is a vee-corrugated (pleated) intermediate cover patented by Hollands and Sibbitt (1978). This material has good insulating properties and excellent solar radiation transmission. Unfortunately the material is not commercially available and appears difficult to manufacture. A honeycomb structure formed from transparent film was investigated by Hollands *et al.* (1992) which was shown to provide very good insulation and also excellent transmission of solar radiation. A detailed analysis of the performance characteristics of the above materials is presented in chapters 3 and 4 of this thesis.

The collectors researched by Butti and Perlin, (1977) and the closed type collectors developed by the Japanese (Tanishita, 1970) solved this problem by storing the water in an array of pipes. This solution is practical but does not make full utilisation of the collector volume for storage and it is difficult to provide adequate collector aperture insulation. The parallel pipes increase the surface area subject to convection heat loss. A requirement for mains water pressure is also recognised as opposed to delivering water at the dynamic head pressure due to a small elevation of the system above the point of use. The mains pressure supply may be contained within a robust heat exchange device. The selection of a suitable heat exchange device is detailed in chapter 5 of this thesis.

Tanishita (1970) found some of the closed membrane type heaters were constructed entirely from black material. However, others were constructed with the upper section from transparent material and the lower section from black material. A detailed discussion of this aspect is given in chapter 6 of this thesis.

The next design aspect when considering an integral collector-storage heater is how to construct a container that can be installed on an inclined surface without the resulting hydrostatic pressure of the contents causing damage to the container. The Solahart 'Hot Top' heater achieves this by construction from relatively thick steel sheet material, however the maximum operating pressure is specified as 120 kPa. Discussion of this aspect of the collector design is presented in chapter 7 and 8 of this thesis.

Success of a solar water heater in the Australian market place relies heavily on the product meeting relevant Australian Standards (AS/NZS 2712:2002). This allows the heater to be eligible for inclusion in the federal RECs scheme and local government rebates. The product certification process will be discussed in Chapter 9 of this thesis.

3. TRANSPARENT INSULATION MATERIALS - THEORY

This chapter describes the importance of a well insulating top cover system for integral collector-storage solar water heaters. The background theory for a selection of transparent insulation materials is discussed and a comparison of the expected performance characteristics of each is presented. Also presented are the benefits of selective surfaces applied to the absorber component of solar water heaters and used in conjunction with transparent insulation materials.

3.1 Overview of top cover system requirements

The most distinguishing performance feature that sets integral collector-storage solar water heaters apart from traditional heaters with separate collector and storage is the heat loss characteristics. Integral collector-storage water heaters have the entire aperture area and thus the heated, stored water exposed to ambient conditions through the top cover system. This exposure leads to significantly high energy loss from the contents during night time, potentially leaving little useful energy available the following morning. To minimise heat losses through the top cover it is important the transparent top cover has the highest insulation possible. Additional heat losses from the sides and back of the integral collector-storage heater may be minimised by the use of well insulating products such as mineral wool or two-part polyurethane foam.

A high level of heat loss would be acceptable in the collector of a thermosyphon type solar water heater with separate collector and well insulated storage tank, as only the fluid in the collector passage ways looses energy at a high rate. The heated water in the storage tank is well protected from heat loss and maintains temperature very well for extended periods.

In addition to efficient insulation, it is desirable that the top cover provides maximum transmission of solar insolation. A top cover system with very low heat loss is not beneficial if the transmission characteristics are poor and do not allow much energy to be collected during day time. Hence, it can be seen that there is a limit to both the insulation properties and the solar transmission of a top cover that achieves an optimum outcome in the overall performance of the water heater.

Consider a top cover system for an integral collector-storage solar water heater that has a flat sheet of transparent material at the upper surface, and a solar absorber below. The flat sheet at the upper surface protects the remaining components inside the cover system from the elements, has a smooth finish to avoid dust and debris build up and would ideally have the highest practical solar transmission characteristics. The single top cover sheet is usually all that is required on traditional heaters with separate collector and storage tank.

However, the integral collector-storage water heater requires much lower heat loss than a single flat sheet cover can provide, with typical effective heat transfer coefficient 6.6 W/m^2K (Duffie and Beckman, 1991), to achieve even mediocre overall performance without the use of a selective absorber surface. This may be compared with an effective heat transfer coefficient of approximately 0.75 W/m^2K for a well insulated cylindrical storage tank (Fairman *et al.* 2001). The heat loss characteristic of the top cover system can be improved by placing some intermediate transparent insulation material between the outer flat sheet and the absorber as shown in Figure 3.1. A selective surface may also be applied to the solar absorber that has low emittance of thermal (long wave) radiation to reduce heat loss, while it also has high absorptance of solar (short wave) radiation.

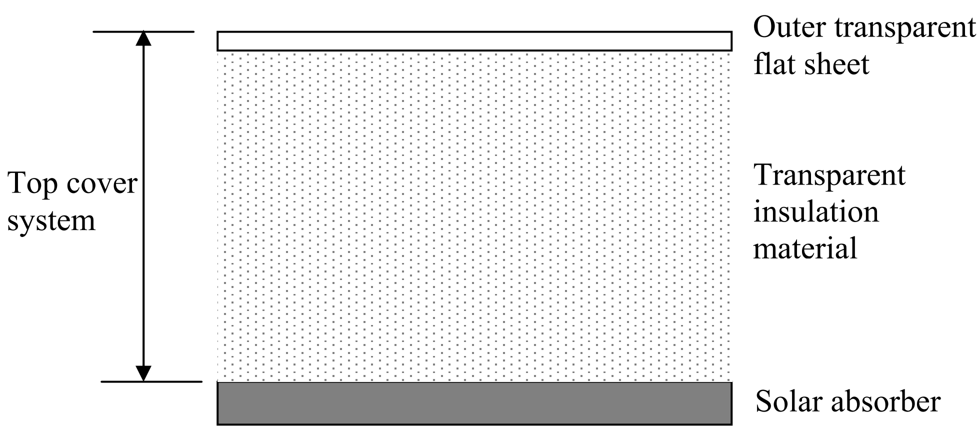

Figure 3.1 Transparent insulation material between outer flat sheet and solar absorber

Assuming the absorber is at the same temperature as the body of water contained in the integral collector-storage heater, the rate of energy lost from the water body is equal to the rate of energy lost from the solar absorber (plus a small amount of parasitic side and back heat loss). The energy lost from the absorber may be due to heat transfer by conduction, convection, thermal radiation or a combination of these. The relative contribution of each of the heat transfer mechanisms is dependent on the configuration of the collector in question.

Three forms of top cover system will be presented along with the background theory describing the performance characteristics of each. They are;

- Twin parallel transparent flat plates cover system
  - an intermediate transparent flat plate increases insulation by reducing convection
  - radiation is reduced by absorbing radiation from the absorber and emitting radiation at a temperature lower than that of the absorber
  - a selective surface on the absorber may also be employed to reduce radiation

- Transparent vee-corrugated sheet with flat plate cover system
  - where a layer of transparent material made from thin sheet in a corrugated form increases insulation by suppressing convection
  - the intermediate material reduces radiation heat loss by a similar mechanism as with the intermediate transparent sheet

- Transparent honeycomb with flat plate cover system
  - where a honeycomb structure with vertical walled cells made from thin transparent sheet increases insulation by suppressing convection
  - the absorption and re-emittance of long wave radiation throughout the honeycomb structure provides good radiation suppression

3.2 Twin parallel transparent flat plates cover system

The twin parallel flat plates top cover system is possibly the most basic and simplest cover system to produce next to the single cover system. Figure 3.2 shows an example of a top cover system with two parallel acrylic plates, the intermediate cover plate being mounted midway between the absorber and the outer cover.

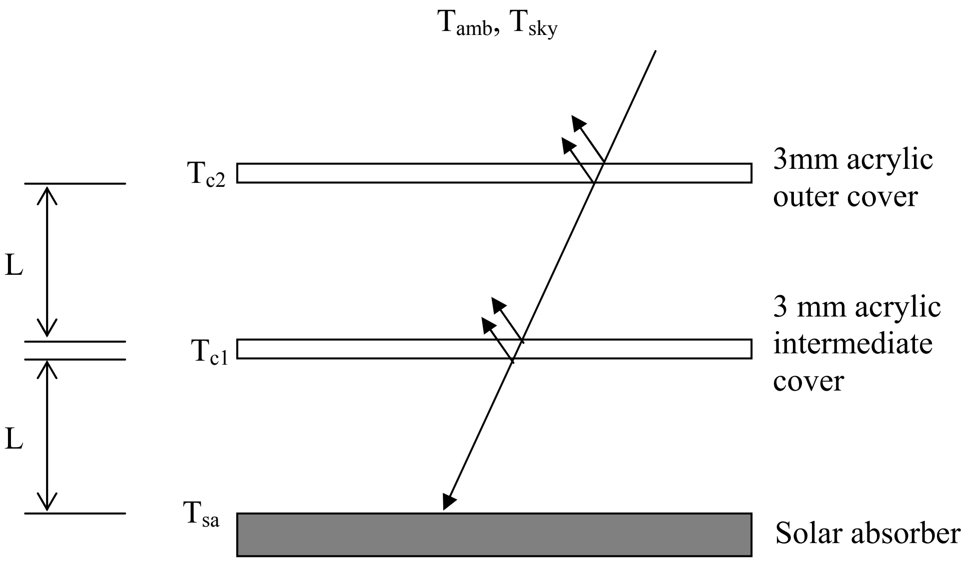

Figure 3.2 Example of twin parallel flat plates cover system, including first reflections of incident solar radiation

To determine the heat loss coefficient for the example cover system, the following assumptions are made;

- The system is at steady state
- The heat transfer through the cover system is one dimensional
- The absorber plate is at uniform temperature
- The cover plates have no temperature gradient through the thickness
- The cover plates are opaque to thermal radiation
- Material properties remain constant with temperature
- The sky may be considered as a black body for radiation heat transfer

The solution for calculating the heat transfer coefficient of an inclined twin parallel flat plate cover system is well known. Equations from Chapter 6 of Duffie and Beckman (1991) were adapted to develop a model in Engineering Equation Solver (Klein and Alvarado, 1999) an iterative solver computer program. A copy of the program and results for the theoretical solution may be seen in Appendix A. The solution requires the user to perform numerous iterations, by estimating the intermediate and outer cover plate temperatures for each successive calculation, if access to an iterative solver computer program is not available. Note the theoretical solution employs an empirical calculation of the Nusselt number between the cover plates.

The program was run with the following input parameters, representative of typical conditions for a cover system;

T_{sa} = 100 ^{o}C {solar absorber temperature}
T_{amb} = 10 ^{o}C {ambient temperature}
T_{sky} = 10 ^{o}C {effective sky temperature}
h_w = 10 W/m^{2}K {wind convection heat transfer coefficient}
β = 45^o {tilt angle of collector}
ε_{ac} = 0.88 {emittance of acrylic cover plates}
ε_{sa} = variable value – see Table 3.1 {emittance of absorber plate}
L = 25 mm {separation distance between plates}

The overall heat loss coefficient for the twin parallel plate cover system was calculated for absorber plates with various emittances. The results are shown in Table 3.1.

In 1979, Klein developed an empirical equation (3.1) to calculate the heat transfer coefficient for a cover system with one or more flat plates (Duffie and Beckman, 1991).

$$U_t = \left\{ \frac{N}{\dfrac{C}{T_{sa}}\left[\dfrac{(T_{sa}-T_{amb})}{N+f}\right]^e} + \frac{1}{h_w} \right\}^{-1} + \frac{\sigma(T_{sa}+T_{amb})(T_{sa}^{\;2}+T_{amb}^{\;2})}{(\varepsilon_{sa}+0.00591Nh_w)^{-1} + \dfrac{2N+f-1+0.133\varepsilon_{sa}}{\varepsilon_{ac}} - N} \tag{3.1}$$

where the notation is as for the exact solution and additional parameters are:

N = number of covers (2 in this case)
f = $(1+0.089h_w - 0.1166h_w\varepsilon_{sa})(1 + 0.07866N)$
$C = 520(1 - 0.000051\beta^2)$ for 0^o < β < 70^o. For 70^o < β < 90^o use β = 70^o
$e = 0.430(1 - 100/T_{sa})$

$\sigma = 5.67x\ 10^{-8}\ W/m^2K$ {Stefan-Boltzmann constant}

Equation (3.1) provides a useful heat transfer coefficient within $\pm$ 0.3 W/m^{2}K for absorber temperatures from ambient to 200^{o}C (Duffie and Beckman, 1991). A program was developed in Engineering Equation Solver (Klein and Alvarado, 1999) to calculate results for comparison with the theoretical solution and shows very good agreement. A copy of the EES program may be seen in Appendix B. The overall heat loss coefficient for the top cover system was calculated for various emittances of the absorber plate. The results are shown in Table 3.1.

Table 3.1. Heat Transfer Coefficient for Various Absorber Emittances

Twin Parallel Flat Plates - Heat Transfer Coefficient U_t [W/m^{2}K]			
Result	**Absorber Emittance (ε_{sa})**		
	$\varepsilon_{sa} = 0.95$	$\varepsilon_{sa} = 0.10$	$\varepsilon_{sa} = 0.06$
Heat transfer solution	3.878	2.411	2.294
Empirical solution (Klien, 1979)	3.876	2.401	2.284

Note that the two cover system shown in Table 3.1 with a high absorber emittance, has a higher heat transfer coefficient (3.9 W/m^{2}K) than a single cover system with selective surface absorber U_T = 3.6 W/m^{2}K (Duffie and Beckman, 1991). There is considerable benefit in using a low emittance surface on the solar absorber. In most cases the presence of a low emittance surface would also mean the surface has low absorptance of incident radiation. There are some special material combinations that have been developed for solar absorbers called selective surfaces. The surfaces combine very low values of emittance for thermal (long wave) radiation with high values of absorptance for solar (short wave) radiation to gain maximum energy with minimal heat loss.

It should also be noted that the transmission of normal incidence solar radiation for a two cover system of approximately 83% is lower than that of a single cover of similar material which is approximately 90% (for glass with refractive index of 1.526 (Duffie and Beckman, 1991)).

3.3 Vee-corrugated sheet / flat plate cover system

The possibility of using a vee-corrugated sheet formed from transparent film was recognised by Suehrcke and the author during a regular thesis progress meeting. The sheet will suppress convection and thermal radiation while maintaining high transmission of short wave solar radiation. Upon searching for previous investigations, it was found there is considerable information available. Hollands and Sibbitt (1978) gained a patent for a vee-corrugated cover sheet for a flat plate collector. Wright and Hollands (1989) concluded that to achieve best thermal performance from a vee-corrugated sheet as an intermediate transparent insulation, an air gap must be left between the tips of the sheet and the bounding absorber and outer cover. A substantially greater effect on the performance of the vee-corrugated transparent insulation system was to apply a high absorptance, low emittance selective surface to the lower hot plate. The experimental apparatus used by Hollands and Sibbit to reach these conclusions was similar to that described by Suehrcke *et al.*, (2001).

A schematic diagram of a vee-corrugated sheet in a test apparatus is shown in Figure 3.3 below. A description of the type of apparatus used for the experiments is presented in Chapter 4 of this thesis.

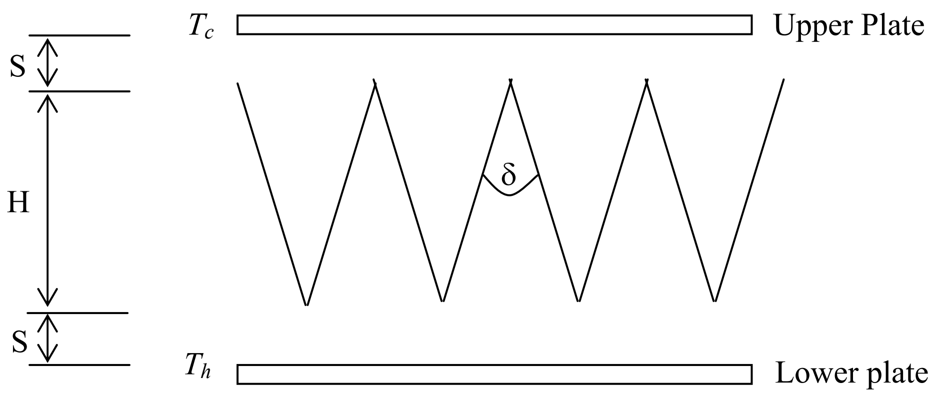

Figure 3.3 Sketch of vee-corrugated sheet intermediate cover

Heat transfer coefficient values measured by Wright and Hollands, (1989) for a vee-corrugated plastic sheet as described in Figure 3.3 are shown in Table 3.2.

Table 3.2. Selected results from Wright and Hollands (1989) experimental data

Vee-corrugated sheet - Heat Transfer Coefficient U_t [W/m^{2}K]			
S/H [-]	**Upper Plate Emittance [-]**	**Lower Plate Emittance [-]**	**U_t [W/m^{2}K]**
0	0.88	0.88	4.98
0.38	0.88	0.88	4.15
0	0.88	0.06	2.68
0.38	0.88	0.06	1.5

The material used for the vee–corrugated by Wright and Hollands, (1989) to obtain the above results was fluorinated ethylene polypropylene (FEP) which has relatively high transmission of thermal radiation. The included angle (δ) for all configurations was 30^o and the vee-corrugated sheet height (H) was 25 mm. The experiment was performed with nominal temperatures of 35^{o}C for the lower hot plate (T_h) and 25^{o}C for the cold upper plate (T_c).

Vee-corrugated sheet allows higher solar transmission than a flat sheet of the same material. Sibbitt and Hollands (1978) reported an increase in normal incidence solar transmission from 90% for a flat sheet to 97% for vee-corrugated sheet with an included angle of 30^o. This high transparency is due to forward reflection of the incident radiation by the steeply inclined walls of the cover material. A schematic representation of the forward reflection effect may be seen in Figure 3.4 below.

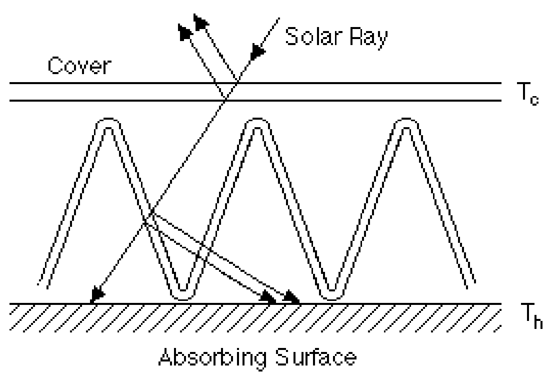

Figure 3.4 Solar ray path through vee–corrugated sheet including first reflections of incident solar radiation (Redrawn from: Sibbitt and Hollands (1978), by Suehrcke *et. al.* (2001))

3.4 Honeycomb / flat plate cover system

Honeycomb is a cellular insulation material constructed from thin transparent plastic film. It has very high transparency for solar radiation while eliminating convection heat transfer and suppressing thermal radiation heat transfer. To effectively eliminate convective heat transfer the honeycomb cell size may be as large as 10 mm. By selecting a suitable material, honeycomb may also suppress a large portion of thermal heat transfer, and smaller cell sizes further reduce radiative heat loss. A photograph of a section of honeycomb being installed in a prototype collector may be seen in Figure 3.5.

Figure 3.5. 50 mm high honeycomb material in cutaway section of a solar collector

The bulk of the following section is taken from work by Dr. Harry Suehrcke, Mr. David Däldehög, Dr. Jonathan Harris and the author of this thesis for an article appearing in the 'Solar Energy' journal (Suehrcke et al., 2004). The main focus of this section is the implementation of a honeycomb model from Hollands *et al*. (1984). The model is used to evaluate the performance of the cellulose acetate honeycomb listed in Table 3.3 and may provide the basis for the development of a model for the vee-corrugated sheet. This section draws and expands on the numerical honeycomb model already described by Suehrcke *et al*. (2000), and expanded upon by Suehrcke *et al.* (2004). For the model development it is assumed that the bounding surfaces (the hot and cold plate) are diffuse grey surfaces and that specular reflection of thermal radiation only occurs at the vertical honeycomb walls.

The model of Hollands *et al*. exploits the symmetry between the honeycomb cells and the fact that the cell diameter is relatively small compared to the honeycomb panel. For every thermal radiation ray transmitted through a honeycomb cell wall there is an equivalent ray transmitted back into the cell from a neighbouring one. Hence, a cell wall may be modelled as being opaque and the transmitted radiation may be treated as reflected radiation in addition to the radiation actually reflected within the cell walls. Moreover, the mid-cell wall point can be regarded as adiabatic so that it is sufficient to analyse a single honeycomb cell with equivalent opaque and adiabatic walls of thickness equal to half the actual wall thickness (Hollands *et al*., 1984).

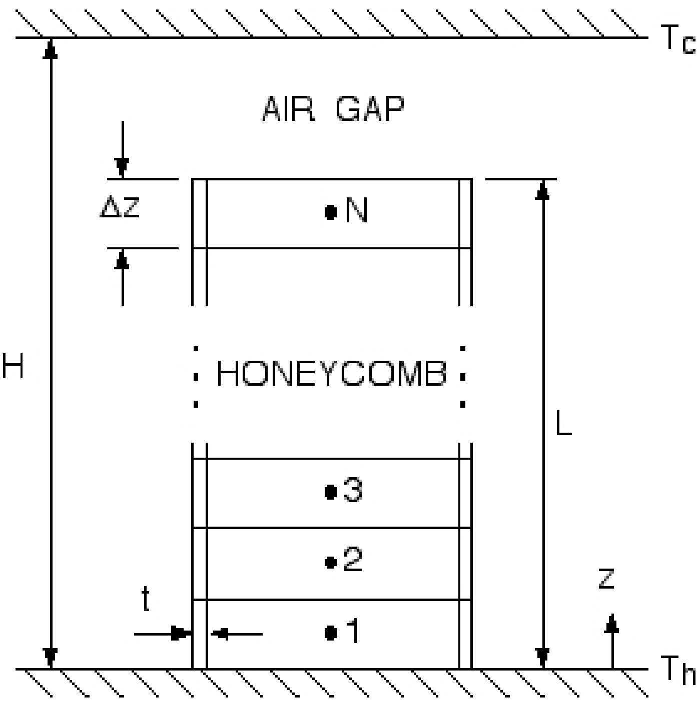

Figure 3.6 Grid for the numerical finite volume model of a single honeycomb cell with air gap. (After: Suehrcke *et al*., 2003).

The governing equations used for the numerical solution are a discretised one-dimensional version of the integral equations presented by Hollands *et al*. (1984). The only difference here is that our equations include the effect of an air gap between the honeycomb and the cold plate. The grid of finite volumes used for the numerical analysis is shown in Figure 3.6.

The energy equation for coupled radiative and conductive heat transfer in an interior volume i, which relates the net energy conducted into the volume to the net energy radiated away from the inner walls of the volume, is given by equation (3.2).

$$\frac{k_e(R+t)^2}{2R}\frac{T_w[i+1]-2T_w[i]+T_w[i-1]}{\Delta z^2}=\varepsilon_w\left(\sigma T_w{}^4[i]-J_hF_{wh}[i]-J_cF_{wc}[i]-\sum_{j=1}^{N}J_w[i]F_{ww'}[i,j]\right) \tag{3.2}$$

The diffuse radiosities J_h, J_c and $J_w[i]$, which represent the outgoing radiation from the hot and cold plates and the volume elements due to surface emission and diffuse reflection, are given below.

$$J_w[i]=\varepsilon_w\sigma T_w{}^4+(1-\varepsilon_w)\left(J_hF_{wh}[i]+J_cF_{wc}[i]+\sum_{j=1}^{N}J_w[j]F_{ww'}[i,j]\right)\delta_{n1} \tag{3.3}$$

$$J_h=\varepsilon_h\sigma T_h^4+(1-\varepsilon_h)\left(J_c F_{hc}+\sum_{i=1}^{N}J_w[i]F_{hw}[i]\right) \tag{3.4}$$

$$J_c=\varepsilon_c\sigma T_c^4+(1-\varepsilon_c)\left(J_h F_{ch}+\sum_{i=1}^{N}J_w[i]F_{cw}[i]\right) \tag{3.5}$$

In the above equations k_e denotes the effective thermal conductivity due to conduction in the air and the honeycomb walls (Hollands *et al.*, 1984), R denotes the honeycomb equivalent cell radius (Hollands *et al.*, 1984), t the honeycomb half-wall thickness (25 μm here), T the temperature, Δz the element size, σ the Stefan-Boltzmann constant and F_{xy} the diffuse or specular radiation view factors from surface x to surface y. The Kronecker delta δ_{n1} sets the diffuse reflectance of the cell walls to zero when the walls are specularly reflecting (n = 1 for diffuse reflectance and n = 2 for specular reflectance). Note that when the walls are specularly reflecting every ray needs to be tracked from the emitting surface and that background information about the above equations can be found in Siegel and Howell, 1972 (Chapt. 9) and in the excellent paper of Hollands *et al*., (1984).

Equations (3.2) and (3.3) provide two equations for the unknown element temperatures and radiosities at each element and equations (3.4) and (3.5) determine the plate radiosities from the given hot and cold plate temperatures.
For the boundary elements a special formulation of equation (3.2) is required. For the hot plate in contact with the honeycomb walls the energy balance equation becomes:

$$\frac{(R+t)^2}{2R}\frac{\left(\frac{T_w[2]-T_w[1]}{\Delta z/k_e}-\frac{T_w[1]-T_h}{\Delta z/(2k_e)}\right)}{\Delta z}= \varepsilon_w\left(\sigma T_w^{\,4}[1]-J_hF_{wh}[1]-J_cF_{wc}[1]-\sum_{j=1}^{N}J_w[1]F_{ww'}[1,j]\right) \tag{3.6}$$

For the cold plate with air gap between the plate and honeycomb the energy balance, on the other hand is:

$$\frac{(R+t)^2}{2R}\frac{\left(\frac{T_c-T_w[N]}{L_{air}/k_{air}+\Delta z/(2k_e)}-\frac{T_w[N]-T_w[N-1]}{\Delta z/k_e}\right)}{\Delta z}= \varepsilon_w\left(\sigma T_w^{\,4}[N]-J_hF_{wh}[N]-J_cF_{wc}[N]-\sum_{j=1}^{N}J_w[N]F_{ww'}[N,j]\right) \tag{3.7}$$

The formulation of the LHS of equations (3.6) and (3.7) allows for modifications when the air gap is on the hot side rather than the cold side or when there are air gaps on both sides.

The above equations were solved using Engineering Equations Solver (Klein and Alvarado, 1999), in a program written by Suehrcke, (2000) which employs Newton's method to solve a set of non-linear equations. A copy of the program may be seen in Appendix C.

Moreover, the equations can be applied for both diffuse and specular wall reflectance. For the case of specular wall reflectance, unlike for diffuse reflectance where the prior history of any ray striking a surface is obliterated (Lin and Sparrow, 1965), one has to keep track of all specularly reflected rays. Therefore the main difficulty in solving equations (3.1) to (3.6) for specular reflection is the determination of the radiation view factors. The view factor between two ring elements, $F_{ww'}$, has been determined from Siegel and Howell (1972, pp. 313-315), while the view factor between a wall element and the cylinder endplates, F_{wc} and F_{wh}, was obtained from Perlmutter and Siegel (1963). All other radiation view factors can be determined from the reciprocity theorem and the summation rule.

Prior to the calculation of the heat transfer coefficient for the honeycomb of interest, the numerical solution was validated against the numerical result by Hollands *et al*. (1984). For 32 finite volumes, agreement with Hollands' solution was achieved to within approximately 1% for both diffuse and specular honeycomb wall reflectance. The result of the numerical solution, assuming that 95% of thermal radiation reflection at the cell walls is specular[1], is shown in Table 3.3.

Table 3.3. Heat Transfer Coefficient for Various Absorber Emmitances with Honeycomb Transparent Insulation Material

Cellulose Acetate Honeycomb - Heat Transfer Coefficient U_t [W/m^{2}K]			
Honeycomb Height	**Absorber Emittance (ε_{sa})**		
	$\varepsilon_{sa} = 0.95$	$\varepsilon_{sa} = 0.10$	$\varepsilon_{sa} = 0.06$
30mm Honeycomb	2.56	2.24	2.22
40 mm Honeycomb	2.07	1.86	1.84
50 mm Honeycomb	1.75	1.59	1.58

The simulations were performed with nominal temperatures of 35°C for the lower hot plate (T_h) and 25°C for the cold upper plate (T_c). The honeycomb wall emissivity used to obtain the above results is 0.65. The emissivity of the upper cold plate is 0.88.

[1] The heat transfer coefficient was calculated from honeycomb heat transfer coefficients for diffuse and specular reflection as: $0.05\ h_{t,diff} + 0.95\ h_{t,spec}$.

Although many assumptions that apply for the heat transfer through a honeycomb cannot be applied for a vee-corrugated sheet, the above solution may provide a starting point for the development of a vee-corrugated sheet model.

4. TRANSPARENT INSULATION MATERIALS – EXPERIMENTAL

As with Section 4 of Chapter 3, the bulk of the following section is taken from work by Dr. Harry Suehrcke, Mr. David Däldehög, Dr. Jonathan Harris and the author of this thesis for an article appearing in the 'Solar Energy' journal (Suehrcke et al., 2004). The design of the experimental apparatus formed part of Mr. David Däldehög's (2002) undergraduate thesis which was supervised by Dr. Harry Suehrcke.

This chapter describes the design of a simple guarded hot-plate apparatus for the measurement of heat transfer across transparent insulation, particularly the vee-corrugated sheet for which there is at present no analytical or numerical solution. The apparatus is used to measure the heat transfer coefficient across flat sheets, a transparent corrugated (zigzag) sheet and honeycomb transparent insulation. The sheet and honeycomb are made from cellulose acetate (CA) film, which has high absorptance for long-wave thermal radiation and high transmittance for short-wave solar radiation. The corrugated sheet performs well, however, honeycomb transparent insulation of the same height and material appears to be superior to due to greater thermal radiation blockage and better solar transmission characteristics. A numerical model for a honeycomb developed in Chapter 3 shows good agreement with the experimentally measured results.

4.1. Experimental apparatus description

Heat flux measurements were carried out using the guarded hot plate method. An electrically heated plate, called the 'metering plate', is embedded in an aluminium guarding plate (see Figure 4.1). By adjusting the power to the metering plate for a fixed power input to the hot plate, the temperatures of the electrical metering plate and the guarding hot plate can be equalised. Under this condition there is no heat flow between the metering plate and the guarding hot plate, and all (electrical) power dissipated in the metering plate flows through the sample space above the plate. A measurement of the power then enables the heat flow through the sample to be determined.

The apparatus shown in Figure 4.1 is similar to that used by Hollands (1973) except for the heating and cooling methods of the hot and cold plates. The guarding hot plate is a 300 × 300 mm aluminium plate, 16 mm thick, and is heated from below by an electrical heater mat. The metering plate consists of an electrical heater plate sandwiched between two thin aluminium plates and is located in a central recess 10 mm deep and 104 mm square. The metering plate is clamped to the guarding hot plate with four Teflon screws. A heat flux meter is placed in between the metering plate and guarding hot plate to sense the heat flow between the plates.

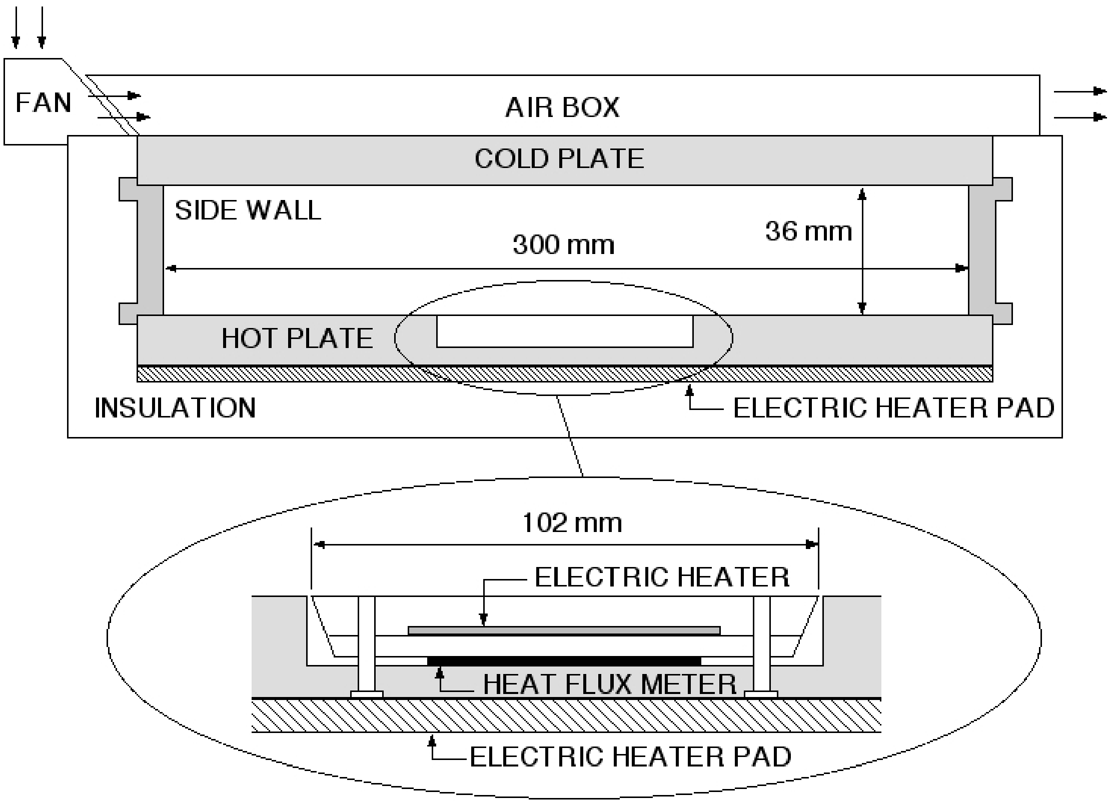

Figure 4.1. Schematic diagram of guarded hot-plate apparatus for heat transfer rate measurement.

The cold plate is a 300 × 300 mm aluminium plate of 8 mm thickness. A cylindrical centrifugal air fan from a photocopy machine is used to ensure even heat removal from the cold plate and maintain the cold plate at a constant lower temperature, approximately equal to the ambient temperature in the air-conditioned room. An air box is used to establish an even airflow (approximately 10 m/s) over the entire plate as shown in Figure 4.1. The hot and the cold plates are separated by a 1.2 mm thick stainless steel sidewall, which is insulated with 25 mm polystyrene insulation on the outside. The conducting sidewall provides an approximation to a linear temperature gradient boundary condition. The sidewall height is 36 mm, giving a sample space of 36 × 300 × 300 mm.

Surface temperatures of the metering plate and the cold plate are measured with K-type thermocouples embedded under the surface of the plates and arranged to measure the temperature difference using a digital differential thermometer. The hot and cold plate surfaces are painted with flat black enamel paint, whose approximate emittance will be determined in Section 4.3. The stainless steel sidewalls, on the other hand, have a rough sandpaper finish and a thermal emissivity of approximately 0.22 (Incropera and DeWitt, 1996). The guarding hot plate is heated to a temperature of approximately 50°C, and the cold plate is maintained near room temperature (approximately 25°C), giving a temperature difference of about 25 K between the hot and cold plates (actual temperatures are indicated in Section 4.4).

The heat transfer coefficient, h_t, is calculated by dividing the electrical power dissipated in the metering plate (product of direct current, I_{el}, and voltage, U_{el}) by the temperature difference between the metering plate and the cold plate ($T_h - T_c$) and the metering plate area, A, as shown in equation (4.1).

$$h_t = \frac{I_{el}\,U_{el}}{A\,(T_h - T_c)} \tag{4.1}$$

4.2. Experimental apparatus design calculations

In the design of the apparatus several calculations were carried out to quantify its thermal characteristics (Däldehög, 2002). In order to check the surface temperature uniformity a two-dimensional numerical simulation of the heat conduction in the hot plate was performed. To this end a finite difference solution (Bejan, 1993) for the hot plate temperature distribution was obtained on a 2 mm square grid using Engineering Equation Solver (Klein *et al*., 1997).

Assuming experimental conditions similar to those for the air only case with heating from below (see Table 4.1) suggested that the temperature of the hot plate at the sample space surface decreases by 0.31 K towards the outer edge (Däldehög, 2002). Furthermore the simulation suggested that the hot plate temperature just below the centre of the heat flux meter is approximately 0.17 K above the maximum hot plate temperature at the sample space surface. Although the simulated 2 D case does not fully represent the actual 3 D apparatus, it still provides an estimate of the uniformity of the hot plate temperature.

The choice of sidewall thickness is necessarily a compromise between achieving linearity in the sidewall temperature profile and minimising the "short circuit" heat flow between the hot and cold plate. For the case simulated above, the 1.2 mm stainless steel sidewalls conducts about 1/3 of the heat generated by electrical heater mat to the cold plate. The apparatus sidewall temperature linearity was checked by modelling the sidewall as a fin with prescribed boundary conditions (T_h and T_c). The calculation indicated that for 25 mm polystyrene insulation the difference from temperature linearity is no more than 0.5%. The result is similar to that previously obtained by McBain, 1996.

The transient behaviour of the apparatus was also investigated. Using the approach of Suehrcke (2001), the main apparatus components (test plate, hot plate, sidewall, cold plate and sample air space) were modelled as thermal network of lumped masses whose heat flow interaction is described by thermal conductances. The sample air space was assumed to be transparent to thermal radiation and the thermal radiation exchange between the apparatus components was simplified as black body radiation exchange. The model results showed that the apparatus time constant is about 1.5 h or that it takes approximately 5 h for the apparatus to reach steady state. In subsequent measurements the apparatus was considered to be at steady state when there was no notable change in the plate temperatures and when the change in the heat flux meter output was less than 0.01 W/m^2.K over a 15 minute period.

4.3 Experimental apparatus calibration

The heat transfer apparatus was calibrated by performing a test with air only (no sample), with the apparatus inverted and heated from above. In this case heat transfer is by conduction and radiation only (no convection), and may be accurately calculated from heat transfer theory. Comparing the result calculated from theory with the corresponding measured result allows the unknown cold and hot plate emissivities to be determined.

The downward conduction heat transfer component from the test plate was calculated from the one-dimensional form of Fourier's law, which is permissible due to the linear temperature sidewall boundary conditions. The radiative heat transfer component, which is not quite equal to the radiative heat transfer between plane infinite parallel plates, required special consideration of the finite apparatus dimensions. The test plate, which measures the overall heat transfer rate, will emit a small portion of radiation onto the apparatus sidewalls. As the average sidewall temperature is higher than that of the cold plate, this has the effect of (slightly) reducing the radiative heat transfer component over the case of infinite parallel plates.

The reduction in thermal radiation heat transfer due to the sidewalls was quantified by modelling the sample space as a four surface enclosure. For this purpose a standard radiation heat exchange calculation for a diffuse grey enclosure (Incropera and Dewitt, 1996) was performed, where the expression by Crawford (1972) was used for the radiation view factor between the 102 mm square test plate and 300 mm square cold plate. Assuming diffusely reflecting sidewalls with surface emittance of 0.22, the result of this analysis showed the radiative heat transfer is 1.6% lower than that for infinite plates.

Using the experimental data from Table 4.1 for the air only case with heating from above and equating the heat transfer coefficient between measurement and theory, yielded an emittance for the hot and cold plates of 0.92. There was no information available from the paint manufacturer to confirm this value, however, a plot of the emittance of flat black enamel spray paint was found on a NASA website (2003) which in the region of 8 to 15 μm suggested a similar value.

4.4 Heat transfer measurements

During the experiments the heat transfer surfaces were horizontal, with the heater plate at the bottom, the only exception being the air only calibration measurement where the heater plate was at the top. Experimental results were obtained for (i) air only with heating from above and below, (ii) a 3 mm thick acrylic sheet placed horizontally at mid-height in the sample space, (iii) a flat film of 50 μm cellulose acetate placed horizontally at mid-height, (iv) a corrugated sheet of 30 mm height with 20° included angle and (v) a honeycomb sheet of 30 mm height and 9 × 9 mm cell size. For cases (iv) and (v) the sample rested on the bottom plate and there was a 6 mm air gap between the top of the sample and the cold plate.

The corrugated and the flat test sheets were assembled from 3 pieces of a roll of 50 μm thick CA film. In both cases the central 120 mm wide piece covering the test plate area had an overlap of approximately 5 mm with the outer pieces. The results of the heat transfer measurements are shown in Table 4.1.

Table 4.1. Results of Heat Transfer Measurements and Modelling ($\varepsilon_h \approx 0.92$, $\varepsilon_c \approx 0.92$, $T_a \approx 22^oC$).

Sample	I_{el} [A]	U_{el} [V]	T_h [°C]	T_c [°C]	h_t measured [W/m^2.K]	h_t modelled [W/m^2.K]
Air only Heated from above	0.269	6.01	52.5	29.0	6.61 ± 0.35	6.61
Air only Heated from below	0.292	6.55	48.6	28.1	8.97 ± 0.45	8.56
3 mm Acrylic sheet Placed mid height	0.235	5.25	54.0	26.3	4.28 ± 0.20	4.42
50 μm Flat CA film Placed mid height	0.246	5.51	52.9	27.4	5.11 ± 0.25	5.07
20° CA Zigzag sheet 30 mm height	0.230	5.15	54.2	25.9	4.02 ± 0.20	-
9 × 9 mm CA Honeycomb 30 mm height	0.201	4.49	51.1	26.4	3.51 ± 0.20	3.60

As already discussed for the air only cases the measured heat transfer coefficients do not quite correspond to the case of infinite parallel plates, due to sidewall reducing the radiative heat transfer component by approximately 1.6%. However, for the case of intermediate flat sheets, where the effective sidewall height is about half that for the air only case, and in particular for the corrugated sheet and honeycomb, the sidewall influence was neglected.

An uncertainty analysis of the measured quantities in equation (4.1) shows the root-mean-square uncertainty level in the measured heat transfer coefficients is approximately 5%, and individual uncertainty values calculated are listed in Table 4.1. The uncertainty is dominated by the uncertainty in the measurement of the temperature difference, and could be improved by use of thermopiles or RTDs (resistance temperature devices) rather than single thermocouples. Also the (small) sidewall influence could almost completely be eliminated by covering the sidewalls with specularly reflecting (polished) aluminium foil.

4.5. Discussion of experimental results

The experimental apparatus described in Section 4.1 represents a significant simplification over a conventional guarded hot-plate apparatus. Instead of heat exchange with temperature-controlled water at the cold and hot plates, the cooling and heating is accomplished through air convection and resistive electric heating. The associated simplification in experimental set up and cost savings should make the apparatus suitable for the heat transfer measurement of transparent insulation materials as used in solar collectors. The only requirement is that the experiment is conducted in a room whose temperature will not change significantly (less than $1^{o}C$) over the measurement period.

The results of the experimental testing are shown in Table 4.1. The results of the numerical simulations lie within the experimental uncertainty. All three modes of heat transfer (conduction, convection and radiation) are active to some extent in each case, with radiation being the dominant component. The honeycomb and corrugated sheet effectively suppress convection throughout the sample space, and hence largely eliminate one mode of heat transfer. This is evident for the honeycomb by the agreement between experimental and model results.

For the chosen dimensions the heat loss through a corrugated sheet is only slightly lower than through a flat acrylic sheet (the latter being opaque to thermal radiation), but significantly lower than a flat sheet of the same material. When making this comparison it must be remembered that the heat loss characteristic is not the only performance parameter, and one must take into account the solar transmittance. As already mentioned in Section 3.2, the solar transmittance of the corrugated sheet is significantly higher than for a flat transparent sheet (up to 10 percent). Hence, for a blackened solar absorber where light concentrations and incident angle changes are not important, a corrugated sheet should have a performance advantage over an intermediate (thermally opaque) flat sheet.

The honeycomb has a lower heat loss than the corrugated sheet. This may be understood from the construction of the two transparent insulation materials. The honeycomb has vertical walls in two directions whereas a corrugated sheet has "vertical" walls only along one axis. This means that a honeycomb more effectively blocks thermal radiation through the greater number of interfering walls. In addition the honeycomb more evenly channels light towards the absorber surface and is not as prone to dust accumulation as may occur in the "valleys" of corrugated sheets. Moreover, the corrugated sheet is not self-supporting and some of the convection suppression properties of a corrugated sheet may be lost when the sheet folds are not oriented horizontally (i.e. there could be convection in the direction of the long axis of the "valley" or "peak" spaces).

The experimental results obtained for the honeycomb and corrugated sheet highlight the outstanding thermal radiation suppression characteristics of cellulose acetate film. In fact when the results are compared to those of Wright and Hollands (1989) the improvement of cellulose acetate material over FEP (Teflon) material becomes apparent. With the use of cellulose acetate material reasonable insulation may be achieved even with high emittance surfaces and without the need to suspend the transparent insulation.

When comparing the measured heat transfer coefficients results to other studies it must be remembered that the heat transfer coefficients are not independent of temperature (due to the dominant contribution of thermal radiation). In this context it should be noted that our coefficients were measured at a higher overall temperature level than those measured by Wright and Hollands (1989). The advantage of our study is that the various transparent insulation materials were investigated at approximately the same temperature level, which makes a performance comparison easier.

4.6. Significance of results

The results show that the use of cellulose acetate material for transparent insulation gives superior performance over FEP (Teflon) material due to its significantly higher absorptance for thermal radiation. Honeycombs, which have vertical walls in two directions, are more effective than corrugated sheets in reducing heat loss. The honeycomb model of Hollands *et al*. compares favourably with experimentally determined results, when the specular reflection along the honeycomb wall is considered.

A honeycomb manufactured from material with high absorptance of thermal radiation may be placed directly onto an absorber surface with relatively high emittance and still provide significant insulation. This combination overcomes the need to suspend honeycomb above a selective surface to achieve reasonable insulation.

5. HEAT EXCHANGER TUBE

This chapter describes the heat transfer process by which energy collected and stored by the integral collector-storage solar water heater is transferred to the mains pressure potable water supply. Calculated and experimental efficiencies are defined for the heat transfer process.

5.1 Principle of operation – heat transfer process

The provision of mains pressure hot water supply to domestic households is considered the industry standard by water heater manufacturers. Cistern fed, gravity pressure systems do exist, however, market acceptance of this configuration appears to be limited. To achieve mains pressure water supply with an integral collector, the absorber may be designed to either sustain the stresses imparted by high water pressure or be equipped with a heat exchanger device that separates the mains pressure water supply from the heat collection medium. A schematic diagram of the heat transfer process with a heat exchanger device may be seen in Figure 5.1.

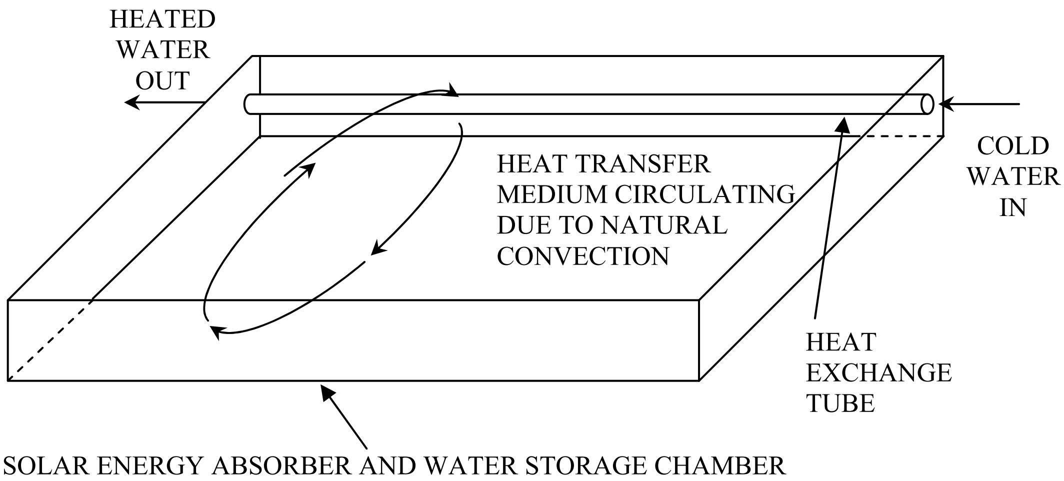

Figure 5.1. Schematic of heat transfer process in collector

Consider the absorber component of the proposed integral collector-storage water heater shown in Figure 1.4. The flat sided shape of the absorber does not lend itself readily to sustaining high internal pressures such as mains pressure at greater than 500 kPa.

A collector such as described may only be capable of sustaining less than 5 kPa of internal pressure due to the large flat panels (particularly the upper glazing) being subjected to excessive stress and deflection.

The proposed collector design incorporates a high efficiency heat exchange tube that is capable of easily withstanding mains water pressure. Energy stored within the hot water contained in the chamber of the absorber is transferred across the walls of the finned copper tube into the resident potable water supply. During periods of no water draw-off from the system, the temperature of the water contained in the tube approaches the temperature of the surrounding fluid. When demand is placed on the system, cold water enters the heat exchange tube and gains energy until it exits the heater at elevated temperature. To be practicable, the heat exchanger must be capable of heating the internal water to temperatures close to that of the surrounding heat transfer medium at a typical hot water flow rate 8 litres per minute. The heat transfer rates in this situation are typically 15 to 20 kilowatts depending on cold water inlet temperature.

Initially, selection of a suitable heat exchange tube was undertaken by gathering information from commercial suppliers on price, availability and performance of their stock range of tubes. A process of elimination based on the above considerations was used to select a medium height, finned, copper heat exchange to be included in the solar water heater design. A schematic of a section of heat exchanger tube and thermal resistance network may be seen in Figure 5.2.

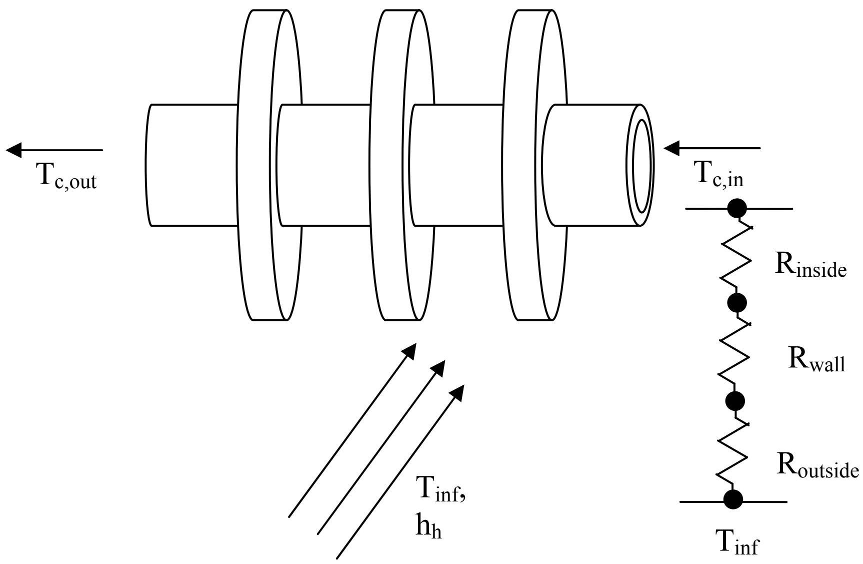

Figure 5.2. Schematic of finned heat exchanger tube

5.2 Heat exchange efficiency calculation

The heat transfer process across a tube wall with fluid on both sides is well known and can be found in most introductory heat transfer texts. An additional level of difficulty arises when the tube has thin fins incorporated onto the external tube surface and a wavy inner tube surface. Incropera and Dewitt (1996) present an excellent development of the theory for calculating heat transfer across the walls of an externally finned tube. The governing equations for calculating the efficiency of the heat transfer process across the heat exchanger tube may be seen below.

Consider the energy gained by the mains pressure water supply;

$$q_{tube} = \dot{m}_{tube} \cdot C_p \cdot \left(T_{c,out} - T_{c,in}\right) \tag{5.1}$$

where, q_{tube} = energy gained by the water in the heat exchanger tube in W

$\dot{m}_{tube}$ = mass flow rate of water through the heat exchanger tube in kg/s

C_p = specific heat of the water in the heat exchanger tube in J/kg.K

$T_{c,out}$ = temperature of the water exiting the heat exchanger tube in K

$T_{c,in}$ = temperature of the water entering the heat exchanger tube in K

The maximum amount of energy that may be gained by the water in the heat exchanger tube is limited by temperature of the heat transfer medium in the collector;

$$q_{\max} = \dot{m}_{tube} \cdot C_p \cdot \left(T_{\inf} - T_{c,in}\right) \tag{5.2}$$

where, q_{max} = the maximum energy that may be gained by the water in the heat exchanger tube in W

T_{inf} = temperature of the heat exchange medium surrounding the tube in K

The overall efficiency of the heat transfer process may be defined as;

$$\eta_{hx} = \frac{q_{tube}}{q_{\max}} \tag{5.3}$$

where, η_{hx} = the overall heat exchanger efficiency.

By substituting equations. (5.1) and (5.2) into equation (5.3) and reducing, the overall heat exchanger efficiency may be written in terms of measurable temperatures;

$$\eta_{hx} = \frac{T_{c,out} - T_{c,in}}{T_{\inf} - T_{c,in}} \tag{5.4}$$

An Engineering Equation Solver (Klein et al., 1999) computer program was written to establish the heat transfer across the tube walls to the mains pressure water supply and the heat exchanger efficiency as shown in Figure 5.3. A copy of the program with results may be viewed in Appendix D. User input variables are initial bulk temperature of the heat transfer medium, tube inner diameter, outer diameter, fin diameter, pitch and thickness, flow rate and mains water supply inlet temperature. The program computes the internal, wall and external resistances, R_{inside}, R_{wall} and $R_{outside}$, respectively, and thereby determines the heat transfer rate. Note the relative magnitudes of thermal resistances shown in Figure 5.2. The thermal resistance across the tube wall R_{wall} is very small. The internal and external thermal resistances R_{inside} and $R_{outside}$ are similar. For a finned tube with no internal roughening, the internal thermal resistance R_{inside} is largest. The program also includes calculation of the pressure loss for the given configuration of tube. The governing equation for the heat transfer rate across the tube is given in equation (5.5).

$$q = \frac{\Delta T_{lm}}{R_T} \tag{5.5}$$

where, ΔT_{lm} = the log mean temperature difference across the tube wall in K

R_T = the total resistance to heat transfer across the tube wall in K/W

The total resistance to heat transfer across the tube walls is the sum of the radial thermal resistance components shown in Figure 5.2 and defined by equation (5.6).

$$R_T = R_{inside} + R_{wall} + R_{outside} \tag{5.6}$$

The internal thermal resistance is defined in equation (5.7);

$$R_{inside} = \frac{1}{\pi \cdot D_i \cdot L \cdot h_c} \tag{5.7}$$

where, D_i = the internal diameter of the heat exchanger tube in m

L = the length of the heat exchanger tube in m

h_c = the internal heat transfer coefficient in W/m^2.K

The thermal resistance across the tube wall is defined in equation (5.8);

$$R_{wall} = \frac{\ln\left[\frac{D_p}{D_i}\right]}{2 \cdot \pi \cdot L \cdot k_x} \tag{5.8}$$

where, D_p = the external diameter of the heat exchanger tube in m

k_x = the thermal conductivity of the heat exchanger tube in W/m.K

And the external resistance is defined by equation (5.9);

$$R_{outside} = \frac{1}{\eta_o \cdot A_t \cdot h_o} \tag{5.9}$$

where, η_o = the overall fin efficiency

A_T = the total external surface area of the finned tube in m^2

h_o = the external heat transfer coefficient in W/m^2.K

Expressions that define the terms used to calculate the thermal resistances may be seen in the EES program in Appendix D. The program uses an iterative solver technique to calculate the total resistance which then leads to a solution for the temperature of the mains supply water flowing through the heat exchanger tube.

A plot of calculated heat exchanger efficiency versus temperature difference (heat transfer medium temperature – heat exchanger tube inlet temperature) for the selected heat exchanger tube is shown in Figure 5.3.

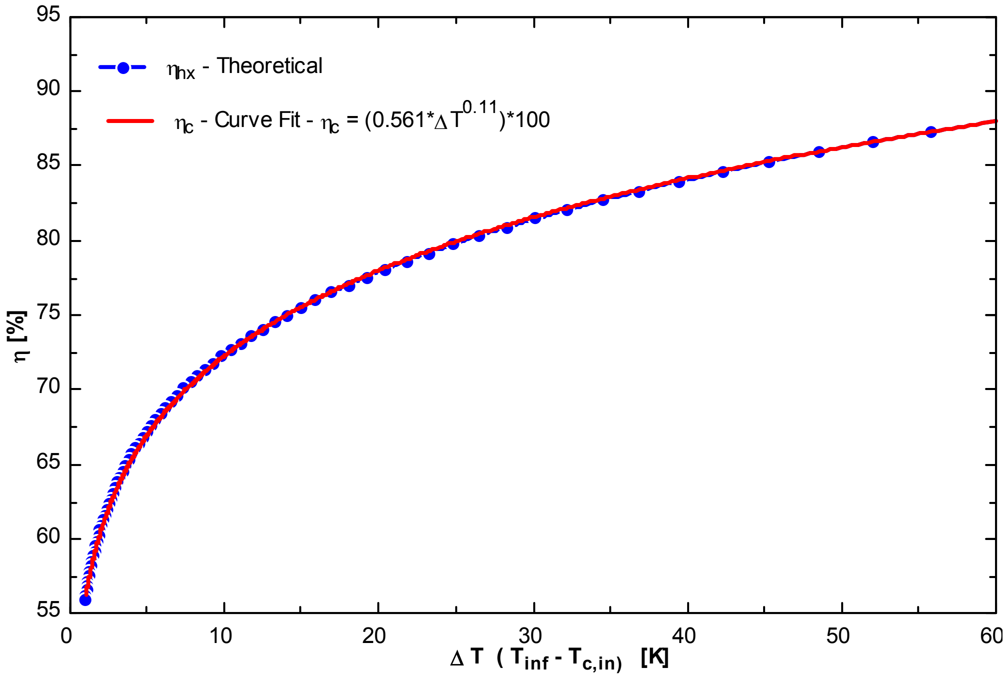

Figure 5.3. Plot of calculated heat exchanger efficiency versus temperature difference for 8 litres/minute flow rate

The selected finned heat exchanger tube has a very clever and unique feature. The medium height fins are formed on the tube in a process very similar to roll forging of a screw thread on a bolt. During the roll forging process, the inner surface of the tube is deformed, with a small ‘rifling’ like ridge with the same pitch as the tube fins appearing on the inner tube wall. The undulations on the inner tube surface enhance the heat transfer coefficient on the inside of the tube through promotion and enhancement of turbulence, which reduces the inner surface resistance R_{inside}. The wavy inner tube surface also promotes a self cleaning effect that limits fouling of the heat exchanger tube due to solid material depositing on the inner tube walls. A photograph showing the inner surface of the tube may be seen in Figure 5.4.

The manufacturer of the tube recommended that at typical flow rates of around 1 m/s, the internal heat transfer coefficient, h_c, appears to increase with flow velocity (Wieland, 2001).

Figure 5.4. Photograph showing undulating inner tube surface

To account for that effect, an effective internal heat transfer enhancement factor, f_{hc} was defined as;

$$f_{hc} = 1 + Vel \quad (5.10)$$

where, Vel = fluid flow velocity in the heat exchanger tube in m/s

So the modified internal heat transfer coefficient may be expressed as;

$$h_c = f_{hc} \cdot h_{ct} \quad (5.11)$$

where, h_{ct} = heat transfer coefficient as per Incropera and DeWitt (1996) theory in W/m^{2}K.

The heat exchanger efficiency calculation (with enhanced internal heat transfer coefficient) was crossed checked against experimentally determined values. The experiment and result comparisons are described in the following sections.

5.3 Experimentally determining heat exchange efficiency

A series of prototype collector-storage water heaters were mounted at a typical tilt angle of 25 degrees on a roof. Temperature sensors were fitted to measure the inlet temperature, the outlet temperature and the heat transfer medium temperature (3 sensors) for each collector. A 6 mm magnetic flow meter was installed to measure flow rate of the mains supply water. Other measured parameters were ambient temperature, solar radiation, the date and time of day. The above parameters were recorded using a Datataker - Model 605 data logger. The apparatus was also used to experimentally determine collector optical efficiency and standing heat loss coefficient. A photograph of the experimental set-up may be seen in Figure 5.5.

Figure 5.5. Experimental apparatus used to determine collector efficiency parameters

The collectors shown in Figure 5.5 are very early prototype heaters with sheet-metal outer casings and low iron glass outer covers.

5.4 Comparison of theory and experimental results

The theoretical solution for heat exchanger efficiency employs one assumption that causes difficulty in comparing results to experimental data. The calculation assumes the energy removed from the heat transfer medium results in a uniform temperature drop over the entire mass of heat transfer medium. During a draw-off period in the test apparatus temperature measurements at a series of points within the chamber showed that the temperature in the collector dropped from a uniform temperature throughout the chamber to a slightly stratified temperature profile. Considering the circulation currents formed in the collector (refer to Figure 5.1) there may be difficulty in determining the average or bulk temperature of the heat transfer medium. An average taken from the stratified temperature profile of the heat transfer medium showed the uniform temperature drop assumption produced reasonable results that may later be used in an entire system performance simulation.

A full scale test of the heat exchanger performance was undertaken to validate the simulation program for heat exchanger efficiency. A photograph of the full scale experimental arrangement is shown in Figure 5.5. The following parameters were measured during the test:

1. The time interval for which data has been collected;
2. The cold inlet water temperature profile;
3. The initial value for average heat transfer medium temperature

Figure 5.6 shows the theoretical and experimental values of heat exchanger efficiency for a 5 minute draw-off episode at approximately 8 litres per minute. This result was found to be typical over a wide range of initial heat transfer medium temperatures. The theoretical heat exchanger efficiency was calculated using the Engineering Equation Solver computer program in Appendix D.

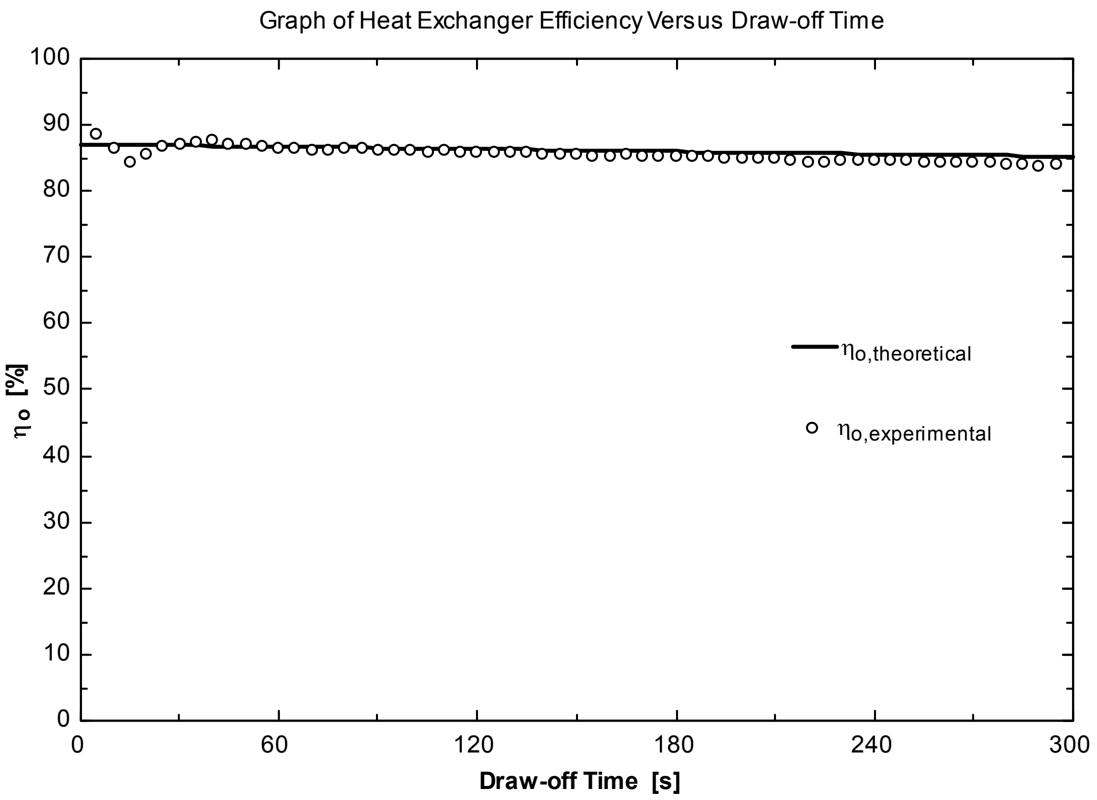

Figure 5.6. Graph of theoretical and experimental heat exchanger efficiency (for a typical draw-off period of 5 minutes)

The measured heat exchanger performance compares very well with the predicted performance for a 7.5 metre long heat exchanger tube. The high level of agreement shows the theoretical model developed, which includes the effect of enhanced heat transfer due to the internal tube roughening, performs well, and is suitably accurate for use in performance prediction calculations. The model for heat exchanger efficiency was used extensively in the overall collector design optimisation.

6. CLEAR TOP COVER VERSUS OPAQUE TOP COVER

This chapter details the performance difference between an integral collector-storage heater with a transparent upper surface on the collector chamber to that with an opaque upper surface. The bulk of the following section is taken from work by Dr. Harry Suehrcke, Dr. Jonathan Harris and the author of this thesis in preparation for a journal publication.

6.1 Overview of the heating process

There is a large body of literature on integral collector-storage heaters and horizontal shallow pond solar water heaters (e.g. see Clark and Dickinson, 1980 for shallow pond heaters), but only a limited account is given here. The two integral collector-storage water heater concepts investigated in this section are: a conventional integral collector-storage heater with blackened upper tank surface; and a glazed "shallow solar pond" heater capable of being mounted on a sloped roof. The latter design differs from common tiltable integral collector-storage heaters with blackened upper tank absorber surfaces[1], in that the upper water tank surface is transparent to solar radiation and that it can withstand the static fluid pressure due to tilt.

The essential difference between heaters with black and transparent tank tops is that for heaters of the former type the solar radiation is absorbed at the upper black tank surface, while for heaters with transparent top surface most sunlight is absorbed inside the water and at the tank bottom surface. This means that the water in the black unit is heated from above, while for the transparent unit the water is heated from within and below. As a consequence the surface temperature (and hence heat loss) of a tank with transparent upper surface is generally lower than that for the tank with blackened upper surface.

1. The use of non-transparent absorber surfaces for tiltable integral collector-storage heaters may be in part understood from the preference to use metal tanks, which offer good structural support against internal fluid pressures forces and which lends itself to the application of a selective surface to reduce thermal radiative heat loss. Moreover, unlike plastic materials, metal materials do not introduce significant thermal resistance in the tank absorber wall.

This performance advantage of the transparent design has already been noticed (Tanishita, 1970). However, it appears that only Lumsdaine (1969) has attempted to quantify the performance difference.

Lumsdaine (1969) developed a model in which the solar heating occurred through a plate in direct contact with a fluid. In the model the optical properties of the plate can range from opaque (e.g. black) to completely transparent. When the plate is opaque all solar radiation is either absorbed or reflected by the plate. When the plate is transparent the solar radiation is transmitted through the plate and is assumed to be completely absorbed by the fluid. Both plate and water in the model were treated as two lumped thermal masses of uniform temperature that were coupled via heat transfer coefficients to each other and the environment.

Using this simplified description, Lumsdaine obtained an analytical solution which describes the temperature variation of the plate and fluid as a function of the time varying solar radiation. After testing the model with experimental data from a shallow solar water pond covered with an acrylic sheet, Lumsdaine used the model to predict the temperature rise of heating oil covered with an acrylic and a copper plate. The results suggested that the oil that was heated through a transparent surface at the end of the day reached a temperature about 40% higher than the oil that was heated from above through a black copper plate.

While Lumsdaine's prediction that a heater with transparent upper tank surface has a performance advantage over one with opaque surface agrees with the observation of Tanishita (1970), it is not clear from Lumsdaine's simple model what the performance advantage will be for a tilted heater with a more conductive and less viscous fluid such as water. That is because a tilted heater will set up convection, and the water body will become stratified.

The performance gain of heater with a transparent upper surface over that of one with a black upper surface warrants further investigation. Moreover, it is well known that in shallow solar ponds there is no significant temperature variation (Sodha *et al*., 1980). It is of great interest to know if this also holds true for tilted “shallow solar pond’ heaters.

In this chapter a performance comparison between an integral collector-storage heater with black and transparent upper tank surfaces is carried out using numerical and experimental techniques. A schematic diagram of an experimental apparatus used and upon which mathematical models are based is presented in Figure 6.1. The aim of this work is to select and/or confirm the most efficient and practical top cover arrangement for the new integral collector-storage heater design. The first sections consider horizontal heaters as it is possible to develop analytical models of their behaviour. The latter sections consider tilted heaters using a combination of numerical analysis and experimental measurement.

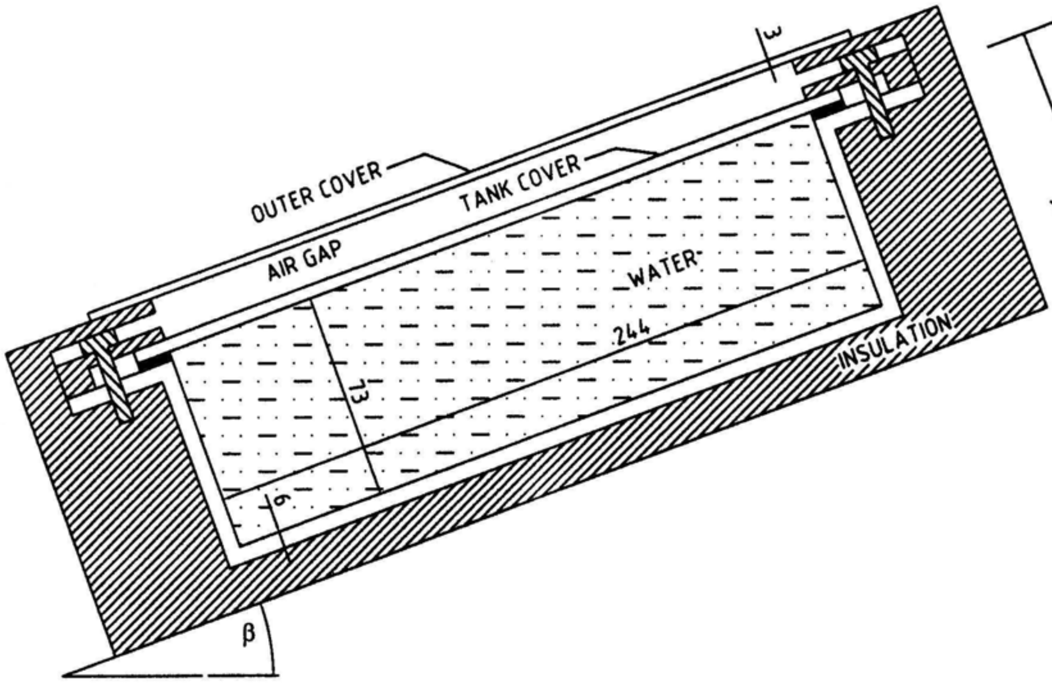

Figure 6.1 Schematic diagram of rectangular integral collector-storage heater (dimensions in mm)

6.2 Clear top cover versus opaque top cover – horizontal heaters

In this section we compare the transient behaviour of two horizontal integral collector-storage solar water heaters with flat rectangular storage tank and single glazing (see Figure 6.1, noting the tilt angle $\beta = 0^{o}$ for this case). The two heaters only differ in the upper tank cover - one of the heaters has a non-transparent blackened tank surface while the other heater has transparent tank cover.

The purpose of this analysis is to determine the effect of upper tank surface transparency on the water heating performance. For this analysis it is assumed that there is no water draw off from the heater during the heating period and that the solar radiation (G_T) in W/m^2 incident on the outer glazing is described by;

$$G_T = 1000\sin\left(\frac{\pi t}{12 \times 3600}\right) \tag{6.1}$$

where t denotes the time in seconds being zero at 6:00 a.m. The above expression gives a maximum incident radiation of 1000 W/m^2 at noon, representative of clear sky condition. Furthermore it is assumed that the top loss coefficient for both heaters is 7.0 W/K.m^2 and that the side and back loss total 2.36 W/K.m^2 with respect to the aperture or top loss area (based on heat transfer calculations for the materials used in the experimental apparatus).

6.2.1 Transparent upper tank surface

Using the observation by Sodha (1980) that there is no significant temperature variation within horizontal shallow solar ponds, the water in a heater with transparent upper tank surface can be approximated as a lumped mass of uniform temperature (this was later confirmed in our experiments). The governing energy balance equation for the fluid storage tank temperature for the heater with transparent upper surface is:

$$mC_p \frac{dT}{dt} = A_c[(\tau\alpha)G_T - U_L(T - T_a)] \tag{6.2}$$

where, m = mass of the storage fluid in kg

C_p = storage fluid specific heat in J/kg.K

T = storage fluid temperature in ^{o}C

t = time in s

A_c = collector (or aperture) area in m^2

$\tau\alpha$ = transmittance-absorptance product (see Duffie and Beckman, 1991 for definition)

U_L = total collector heat loss coefficient in W/m^2.K

T_a = ambient temperature in ^{o}C

Expressing $\theta = T - T_a$ as the excess temperature above ambient and approximating the transmittance-absorptance product ($\tau\alpha$), the collector heat loss coefficient U_L and the ambient temperature T_a as constants over the day, equation (6.2) can be solved in closed form (Suehrcke, 2000). For the initial condition that $T(t) = T_o$ at $t = 0$ (6:00 a.m.) and the driving solar radiation as given by equation (6.1), the solution for the horizontal heater with transparent upper tank surface is;

$$T = T_a + \frac{c\sin(bt - \phi)}{\sqrt{a^2 + b^2}} + d\exp(-at) \tag{6.3}$$

where, $a = \dfrac{A_c U_L}{mC_p}$ (6.4)

$$b = \frac{\pi}{43200} \tag{6.5}$$

$$c = \frac{A_c(\tau\alpha)G_{T,noon}}{mC_p} \tag{6.6}$$

$$\phi = \arctan\left(\frac{a}{b}\right) \tag{6.7}$$

$$d = T_o - T_a + \frac{cb}{a^2 + b^2} \tag{6.8}$$

The noon solar radiation, $G_{T,noon}$ is assumed to be 1000 W/m^2 as noted above. The analytical solution of the transparent top heater, describing the water temperature as a function of the incident solar radiation, is to be compared to that of the heater with black upper tank surface.

6.2.2 Opaque (black) upper tank surface

For the horizontal heater with black upper tank surface the storage tank temperature can no longer be assumed constant as the water is heated from above and the water has considerable thermal resistance.

For the horizontal heater position the heat flow is by conduction only and for a shallow heater tank this heat flow is essentially one-dimensional. The governing equation for one-dimensional heat conduction within the water body is (see Incropera and DeWitt, 1996);

$$\frac{\partial T}{\partial t} = \alpha \frac{\partial^2 T}{\partial x^2} \tag{6.9}$$

where, α = thermal diffusivity of the storage fluid in m^2/s

x = distance perpendicular to the tank upper surface in m

The boundary conditions for equation (6.9) defined at the top surface are through the absorbed solar radiation and the top heat loss coefficient U_t as:

$$-k\frac{\partial T}{\partial x}\bigg|_{x=0} = (\tau\alpha)G_T(t) + U_t(T|_{x=0} - T_a) \tag{6.10}$$

where, k = thermal conductivity of the storage fluid in W/m.K

Ut = top heat loss coefficient in $W/m^2.K$

and at the bottom surface through the back heat loss coefficient U_b as:

$$-k\frac{\partial T}{\partial x}\bigg|_{x=L} = U_b(T|_{x=L} - T_a) \tag{6.11}$$

where, U_b = bottom heat loss coefficient in $W/m^2.K$

Since the boundary conditions are time dependent, equation (6.9) cannot be solved easily in closed form and a numerical solution is most appropriate.

Following Bejan (1993) a finite difference solution of the transient heat conduction problem is carried out. For this purpose the governing equation (6.9) is discretised using equally spaced grid points 1 to N+1 with grid spacing $\Delta x = L/N$, where L is the height of the storage tank. The implicit formulation of the governing equation for interior node elements (i = 2 to N) is;

$$\frac{T_i^m - T_i^{m-1}}{\Delta t} = \alpha \frac{T_{i+1}^m + T_{i-1}^m - 2\,T_i^m}{\Delta x^2} \tag{6.12}$$

where Δt denotes the time step and T_i^m the temperature at interior node i and time m. At the boundary node elements the energy balances become;

$$\frac{T_1^m - T_1^{m-1}}{2\Delta t} = \alpha \frac{T_2^m - T_1^m}{\Delta x^2} + \frac{U_t(T_a - T_1)}{\rho Cp\,\Delta x} + \frac{S}{\rho\, Cp\,\Delta x} \tag{6.13}$$

and

$$\frac{T_{N+1}^m - T_{N+1}^{m-1}}{2\,\Delta t} = \alpha \frac{T_N^m - T_{N+1}^m}{\Delta x^2} + \frac{U_b(T_a - T_{N+1})}{\rho Cp\,\Delta x} \tag{6.14}$$

In equation (6.13) $S = \tau\alpha G_T$ is the rate of absorbed solar radiation at the blackened upper tank surface. For this model, $\tau\alpha$ has been assumed fixed at 0.85. U_t and U_b in equations (6.13) and (6.14) denote the top and back heat loss coefficient, respectively.

The implicit formulation of the governing finite difference equations makes the numerical solution unconditionally stable; i.e. independent of the size of the time step. The accuracy of the solution was tested for U_b = 0 by comparing its output to an analytical solution describing the wall centre plane temperature for a constant absorbed heat flux of 600 W/m^2. The numerical solution with the same boundary conditions agreed within 0.06 K with the analytical solution. Moreover the accuracy of the numerical solution was also tested by comparing it to the analytical solution for the heater with the clear top, equation (6.3), by using an artificially high fluid thermal conductivity of 10000 W/m.K. For a driving solar radiation as described by equation (6.1) both solutions for the fully mixed heater agreed to better than 0.52 K. Finally the grid and time step independence was tested by comparing the numerical solutions for 15 nodes and 120 s time step with that of an 8 node and 300 s time step solution. Both solutions agreed within 0.15 K of each other.

Using the two models for horizontal black top and clear top heaters the relative performance of the heaters may be compared. For the clear top heater the analytical solution equation (6.3) was used, with the following parameters:

m = 70 kg

C_p = 4181 J/kg.K

T_a = 25°C

A_c = 1.0 m^2

L = 0.07 m

$\tau\alpha$ = 0.85

U_b = 2.36 W/m^2.K

U_t = 7.0 W/m^2.K

U_L = $U_t + U_b$

For the black top heater, equations (6.12) to (6.14) were solved for an initial water temperature of 25°C, N = 15 nodes and time step Δt = 120 s using Engineering Equation Solver (Klein *et al.* 1999) with equation (6.1) for the driving solar radiation. Other parameters of the black top model were as stated above with the thermal diffusivity set to α = 1.5918 x 10^{-7} m^2/s. The predicted temperature of the horizontal black top and clear top heaters are compared in Figures 6.2 and 6.3.

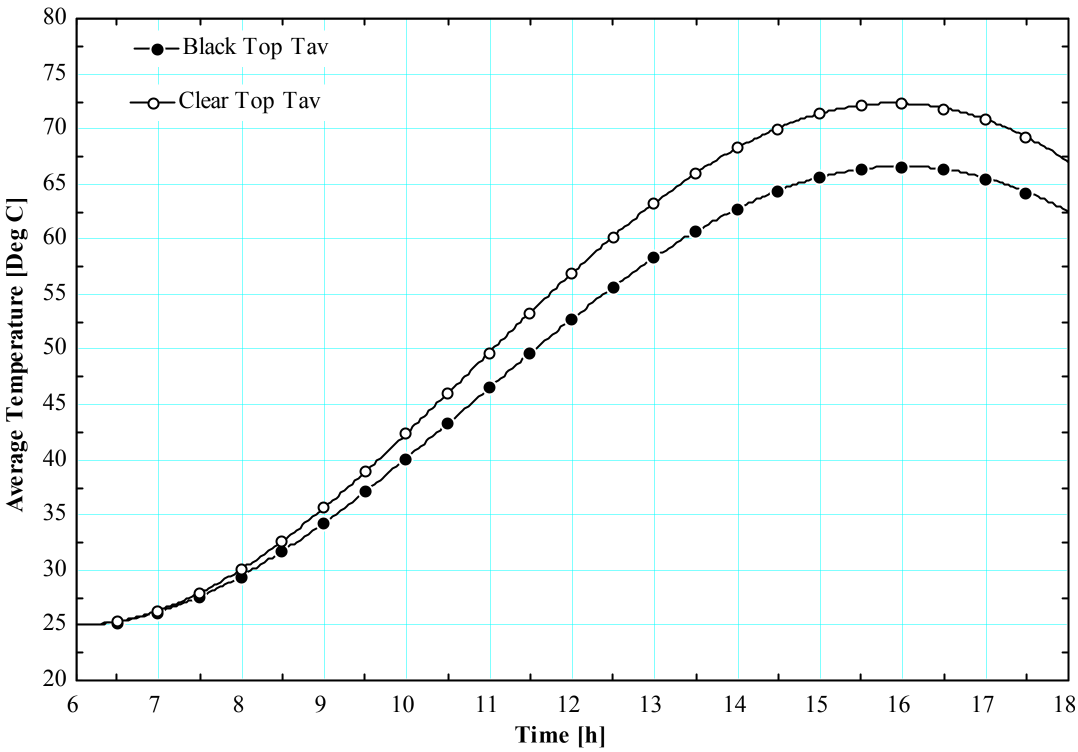

Figure 6.2 Graph of average temperature versus time for black top and clear top heaters (β = 0°)

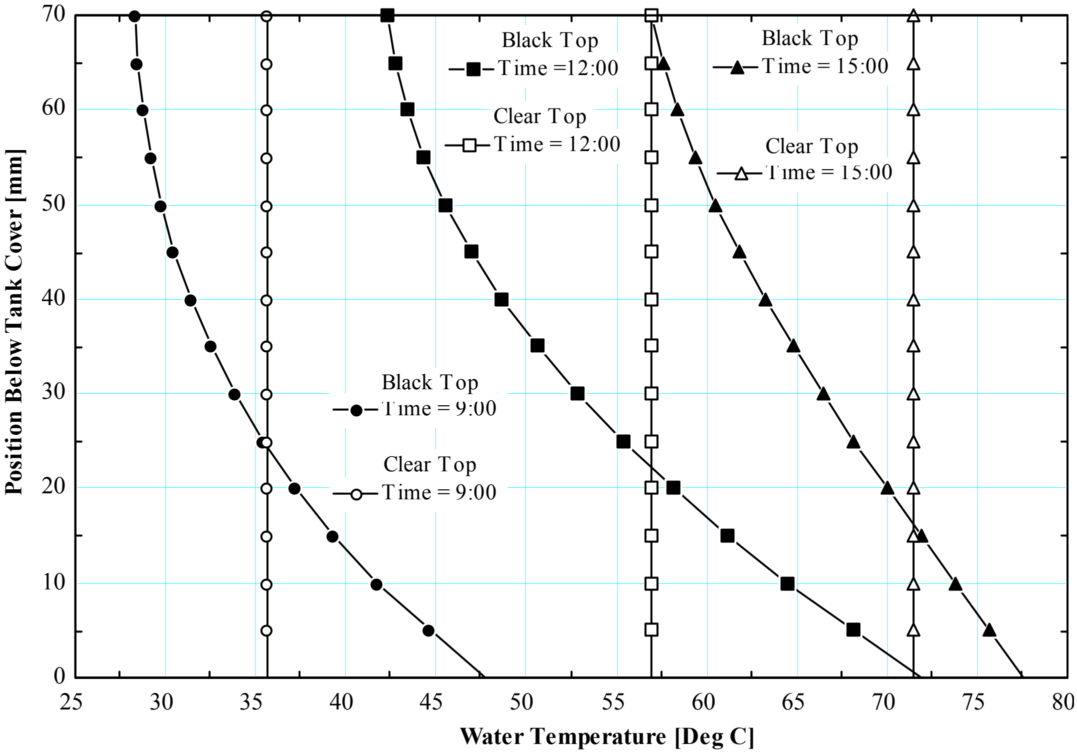

Figure 6.3 Graph of water temperature versus position (x) for black top and clear top heaters with time (tilt angle, $\beta = 0^o$)

Figure 6.2 compares the average water temperatures from for the heater with clear tank top with that for the heater with black tank top. The average water temperature for the heater with clear top was determined from equation (6.3), while for the heater with black top the average tank temperature at any given time is given by:

$$T_{ave} = \left(0.5 * T_1 + T_2 + \cdots + T_N + 0.5 * T_{N+1}\right) / N \qquad (6.15)$$

where the temperatures T_1, T_2, …, T_{N+1} are determined from the numerical solution of equations (6.12) to (6.14).

It is apparent from Figure 6.2 that the water heater with clear top at the end of the day has a performance advantage over the one with black top of approximately 12%, i.e. the water temperature rise in the heater with clear top is approximately 12% higher. The reason for this performance advantage can be explained from Figure 6.3, which shows that top surface heatloss of the black top heater is higher than that for the clear top one.

6.3 Clear top versus opaque top cover – tilted heaters

The analysis presented in the previous section assumes the collectors are positioned with the upper tank cover horizontal. This section considers the relative performance of tilted heaters with transparent and opaque top covers.

For a horizontal black top heater the water within the heater is stably stratified and stagnant, and heat transfer occurs by conduction only. For a relatively shallow horizontal clear top unit the water is heated from below and becomes unstable, resulting in thermal convection currents which mix the water and result in an almost uniform temperature in the unit as noted above. However, when the unit is tilted at a shallow angle (e.g. 20^o) to the horizontal the water in the tank is always in motion, driven by natural convection, regardless of whether the top of the unit is black or clear. Without further analysis it is not clear whether it is still permissible to assume a uniform temperature distribution within the water in the case of the clear top, and by how much the convection currents affect the stratification in the case of the black top. These questions are addressed by establishing a comprehensive two-dimensional model which solves for the flow field and temperature field as functions of space and time. Solutions were obtained for the same cases of black and clear top as considered in Section 6.2.

The model was established using the computational fluid dynamics (CFD) code CFX-4.3 by AEA Technologies. The model simultaneously solves equations describing conservation of mass, momentum and energy. The change in density with temperature was linearised over the range of temperatures studied, and the Boussinesq assumption was employed to simplify the coupling between the momentum and energy equations (Harris, 2000). All other properties, including thermal conductivity, specific heat, and viscosity, were assumed to be independent of temperature. In the clear top case a volumetric heating source term was incorporated into the energy equation to model the heat absorbed within the water column. Outputs from the model are the velocity field (horizontal and vertical components) and temperature field as functions of time.

The computational domain considered represents a cross-section of the water contained in the tank shown in Figure 6.1. No-slip (i.e. zero velocity) boundary conditions were used at all boundaries.

The two cases studied differ only in the top and bottom thermal boundary conditions and the source term required in the energy equation in the clear top case. In both cases the external heat losses through the top, side and back were represented using the same heat loss coefficients as for the horizontal cases considered in Section 6.2.

In the black top case all the incident thermal energy is absorbed at the upper tank surface. In the clear top case the incident thermal energy is partially absorbed within the water column (i.e. volumetric heating), with the remainder absorbed at the bottom of the tank.

For each case the model was run over a period of 24 hours, starting from initial conditions of uniform ambient temperature and zero velocity at 6 am. A time step of 1 s was used for the runs, and full dump files containing temperature and velocity fields were output every 600 s, resulting in a total of 144 sets of results for each case.

To illustrate the results obtained Figure 6.4 shows plots of the temperature and velocity fields at a time of 6 hours after start (i.e. 12 noon) for the black top and clear top cases. The striking feature about the black top case is the strong stratification (50 K temperature difference from top to bottom) and the extremely high temperature in the uppermost corner of the box. In contrast, the clear top case is very well mixed (only 4 K temperature difference), and the hottest temperatures at the base of the box are only a few degrees Kelvin above the mean temperature. Convection currents are evident in both cases; however, the velocities in the clear top case are more than 20 times as great as in the black top case due to the suppression of the motion by the stratification. Heat losses through the upper surface are considerably higher in the black top case compared with the clear top case.

To further illustrate the difference between the black top and clear top cases the mean, minimum and maximum temperatures were computed from each dump file and plotted as a function of time in Figure 6.5. The plot shows that the temperature distribution in the clear top case is very close to uniform, there being a maximum difference of only 4 K between the minimum and maximum temperatures at any time. On the other hand the black top case exhibits a large difference between minimum and maximum temperatures (up to 50 K temperature difference).

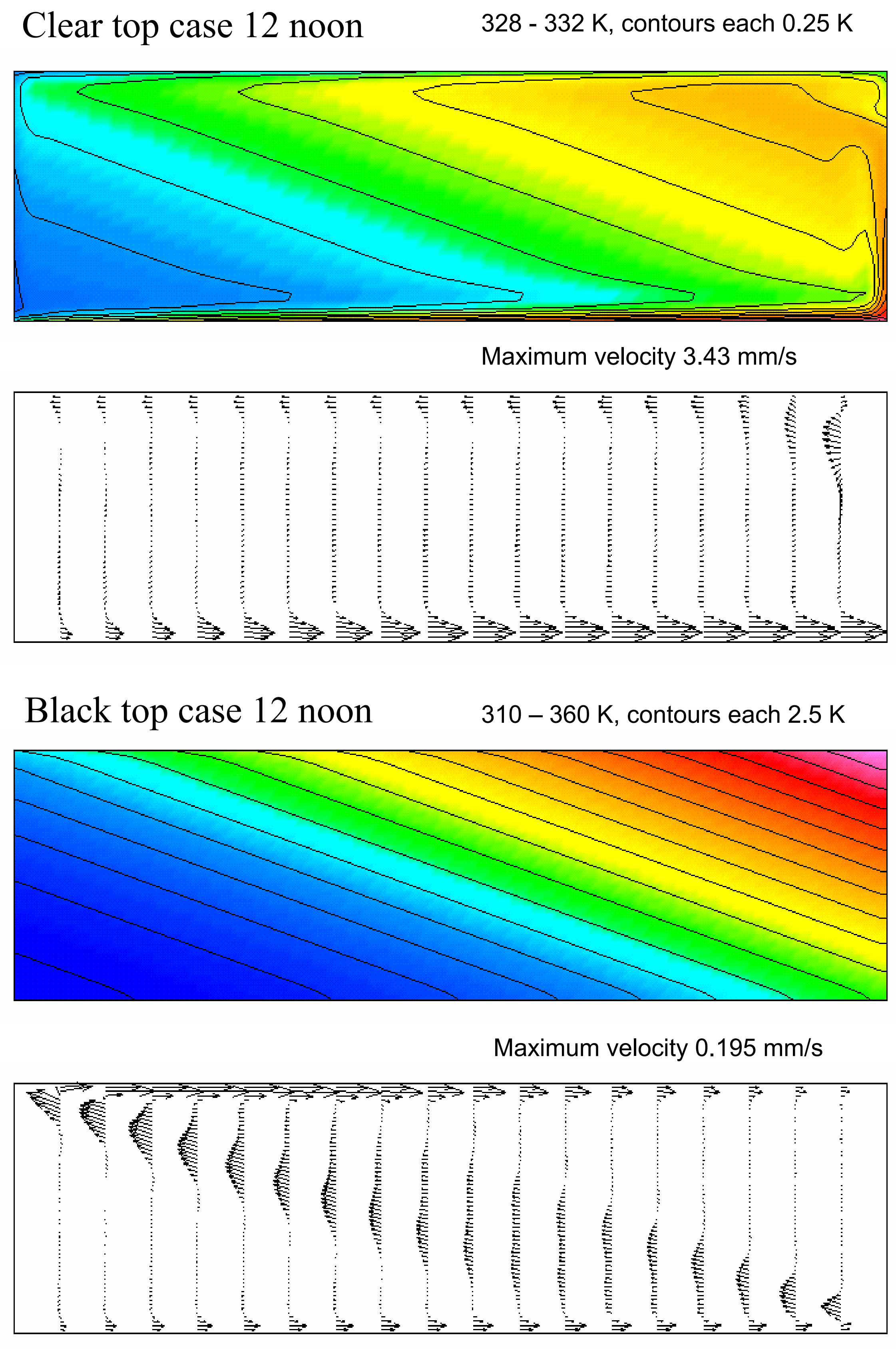

Figure 6.4 Contour plots from CFD analysis of clear top and black top tilted heaters (tilt angle , $\beta = 20^{o}$)

Since the temperature distribution in the clear top case is almost uniform, it is a good assumption to model the clear top unit using a simple lumped approach as presented in Section 6.2, provided one is not interested in the details of the flow pattern or temperature distribution within the unit. However, the simple lumped analysis is clearly inappropriate for the tilted black top case without modification to take account of the strong stratification.

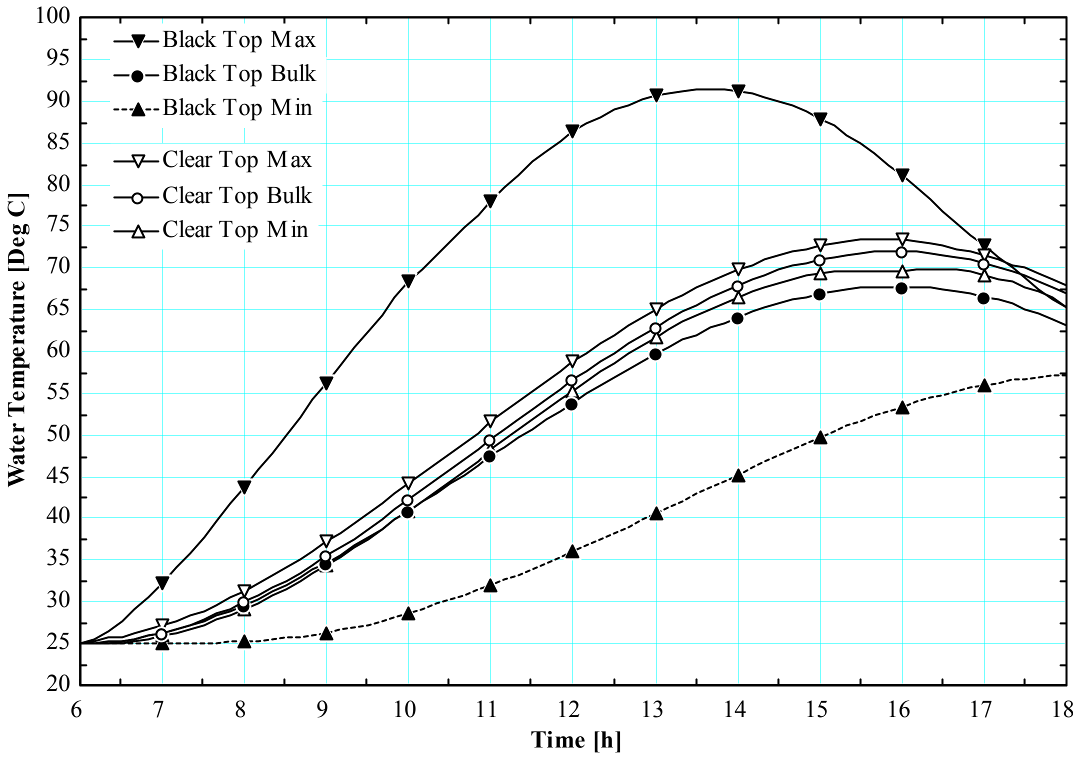

Figure 6.5. CFD temperature profiles for black top and clear top collectors (tilt angle, $\beta = 20^o$)

Figure 6.6 compares the temperature profiles at a line midway in the two cases at 12 noon. The temperature profile in the clear top case is almost uniform, except for a small increase near the bottom (due to absorption of energy at the base) and a small decrease at the top due to surface cooling. On the other hand, the temperature distribution in the black top case shows the strong stratification present. The temperature is elevated further at the top due to the energy absorption there, whereas the decrease in gradient at the base reflects the relatively small heat loss at that location.

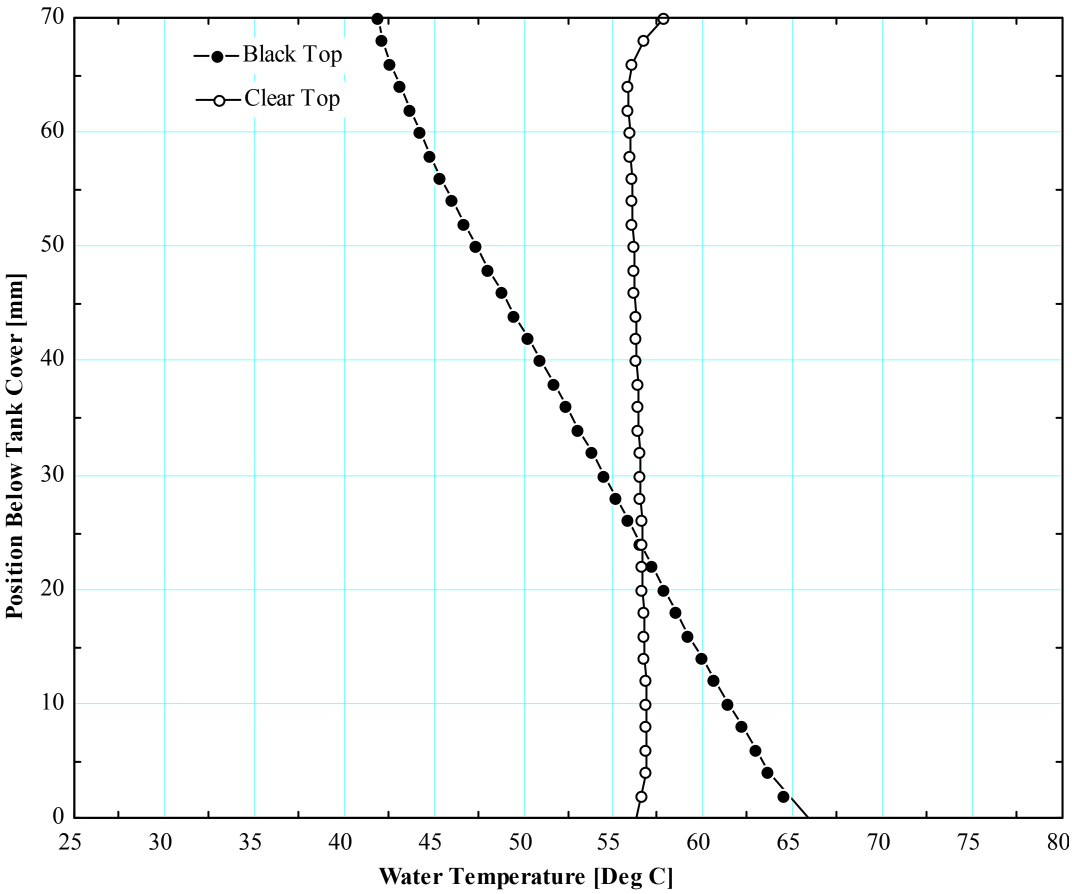

Figure 6.6. Temperature profiles at midpoint of heater at 12 noon for clear top and black top cases.

The temperature profiles in Figure 6.6 for a heater tilted at 20^{o} may be compared with those in Figure 6.3 for a horizontal heater. It can be seen that the temperature profiles exhibit similar characteristics. Overall, the average temperature rise achieved in the clear top unit is about 13% greater than the black top unit at this time of day, reflecting the increased energy absorbed. At the end of the 24 hour period the tilted clear top unit absorbs almost 7 % more energy than the black top unit, similar to the results found for the horizontal heaters.

Figure 6.7 compares the velocity distributions of the clear top and black top units at 12 noon. The higher velocities in the clear top case are clearly evident, with a strong current driven by energy absorption at the bottom surface. There is a reverse current at the surface due to surface cooling. In the black top case the velocities are much lower overall. There is a small rising current at the top of the unit as a result of the net energy absorption at that location.

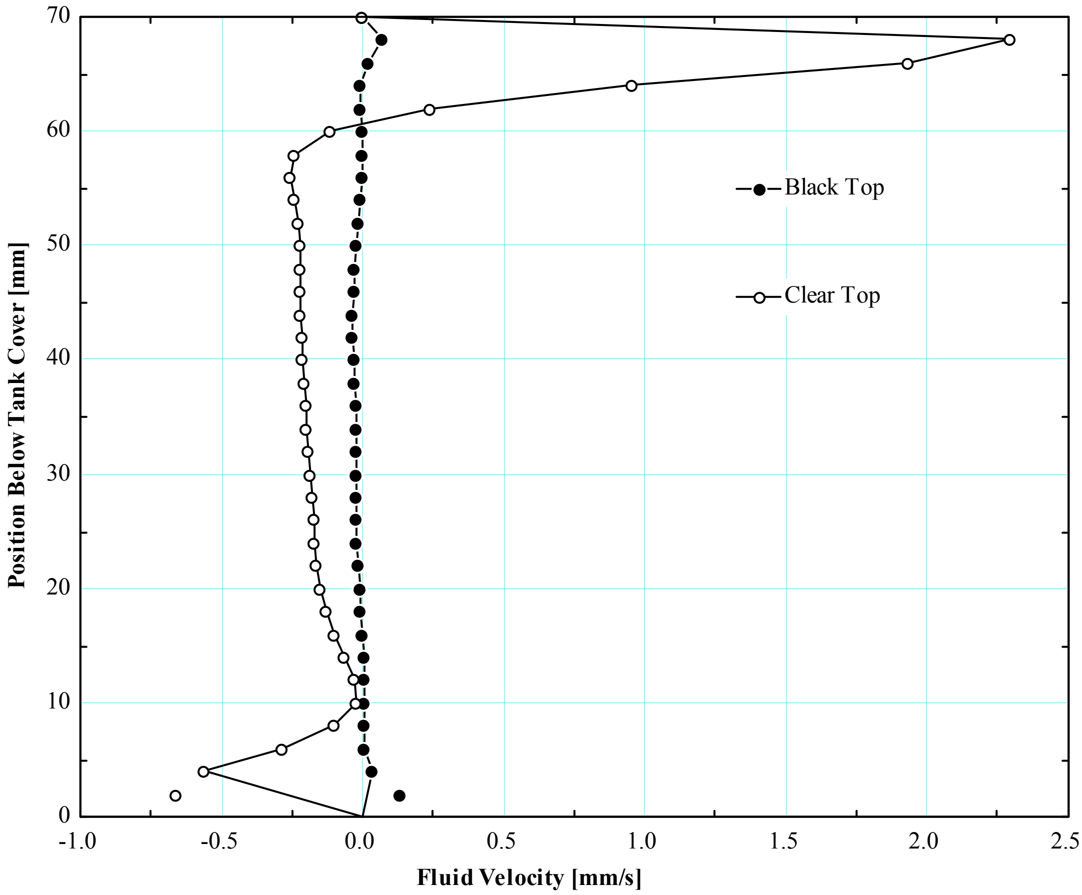

Figure 6.7. Velocity profiles at midpoint of heater at 12 noon for clear top and black top cases.

The following section describes an experimental process that further reinforces the advantages of an integral collector-storage water heater with a transparent top cover over a heater with an opaque top cover.

6.4 Clear top versus opaque top cover – Experimental

An experiment was conducted to confirm the results of the previous sections of this chapter. Two model heaters were constructed with dimensions corresponding to those shown in Figure 6.1. Each collector was fitted with a stainless steel probe containing three equally spaced T type thermocouples. The ambient air temperature was measured using a T type thermocouple fitted into a Stevenson screen. A Kipp & Zonen CM 21 thermal pyranometer was used to measure the incident solar radiation. A photograph of the experimental apparatus is shown in Figure 6.8.

Figure 6.8. General arrangement of experimental apparatus at 20^{o} tilt angle

The collectors are constructed from 6 mm acrylic sheet material. The black top collector absorber plate is made from 4.5 mm aluminium with matt black paint on the upper surface. The clear top collector upper plate is made from 4.5 mm clear acrylic with the inner surfaces of the collector painted matt black.

The outer casings are made of galvanised sheet steel lined with polyurethane foam. Both experimental collectors have a 3 mm clear acrylic outer cover which is separated from the upper plate by approximately 15 mm. The frame on which the collectors are mounted is adjustable from 0^o to 30^o tilt angle. Experiments were conducted at tilt angles of 0^o and 20^o. A plot of the average temperature throughout the day for 0^o and 20^o tilt angles are shown in Figure 6.9.

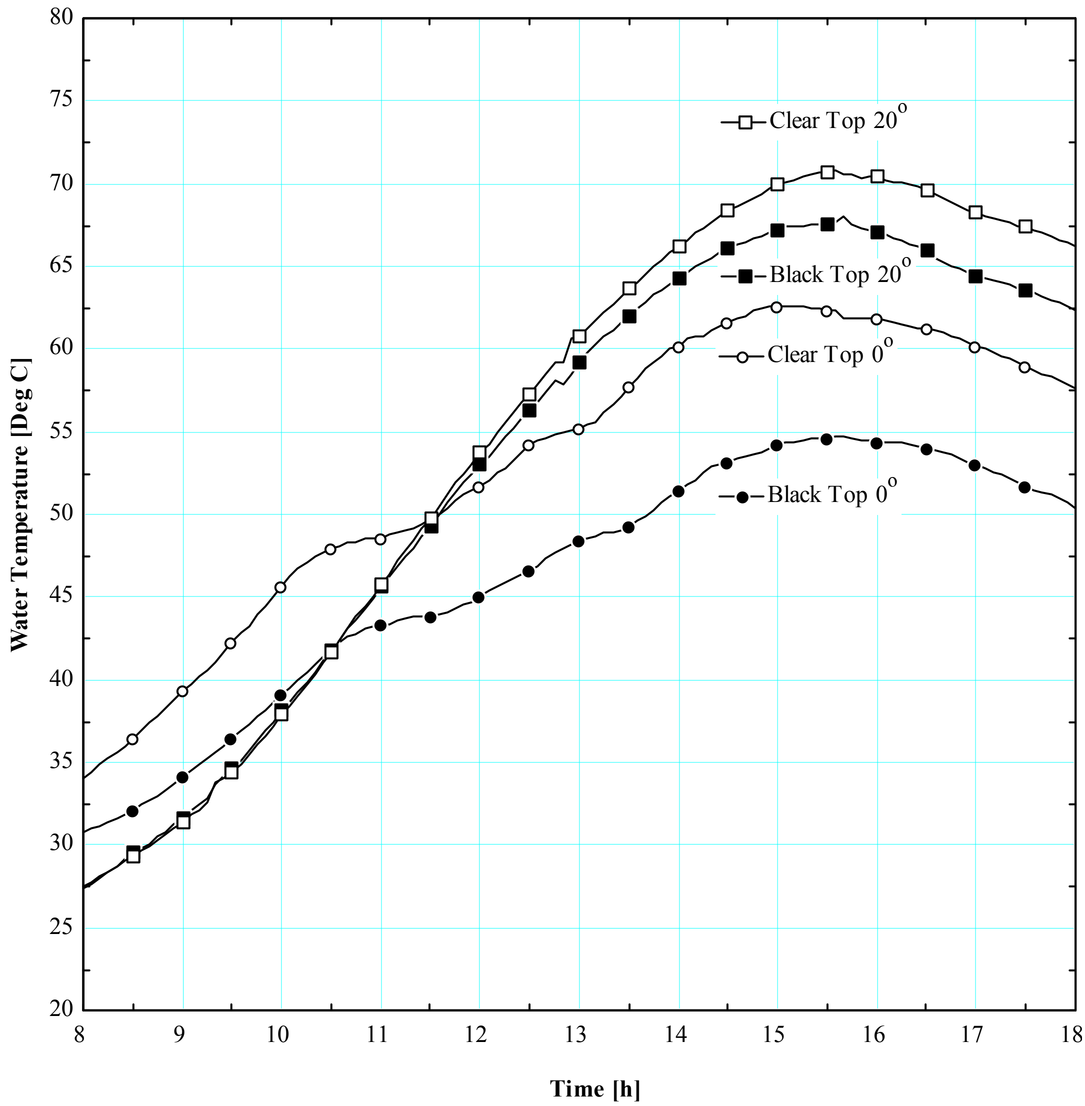

Figure 6.9. Experimental temperature profiles for clear and black top collectors ($\beta = 0^o$ and 20^o)

Although the experiment with 0^o tilt angle did not begin with both collectors at the same temperature, it can be clearly seen that the overall performance (i.e. temperature increase) for the clear top collector is superior to that of the black top collector.

Further experimental testing is required to definitely establish the percentage advantage of the clear top heater over the black top heater. Prior to further testing, the black painted aluminium absorber plate has been replaced with an acrylic sheet with black paint on the underside to ensure the heat loss characteristics of the two collectors is equal.

6.5 Discussion of results

Black top and clear top versions of integral collector-storage water heater have been investigated using a combination of analytical and numerical analysis, computational fluid dynamics and experimental measurements. The improvement in performance of a collector with a transparent upper surface to a collector with an opaque upper absorber surface has been highlighted.

The magnitude of the performance difference between the clear top and black top collectors will diminish if the cover heat loss coefficient can be lowered sufficiently. Transparent insulation materials are not yet available that are able produce the required insulation performance. The use of selective surfaces on the upper plate of an integral collector may assist in reducing the difference, yet this technology may be applied to both transparent and opaque materials with similar performance advantage.

For an integral collector-storage solar water heater it has been shown there are performance advantages in using a transparent upper surface instead of an opaque upper surface. In addition, when a transparent upper surface is used, the temperature distribution within the water body will be essentially uniform, allowing the use of a lumped mass analysis for performance prediction.

7. INDUSTRIAL DESIGN OF THE SOLAR WATER HEATER

This chapter defines the process by which the Hot Harry™ integral collector-storage solar water heater will be manufactured and explains the final design of the heater. Selection criteria such as practicability, availability and commercial pricing influence the specified combination of materials. As discussed in the introduction of this thesis, the major components of the proposed heater will be rotationally moulded. Rotational moulding is the core business of the author's employer, Gough Plastics Pty Ltd of Townsville.

7.1 The rotational moulding process

The rotational moulding process, also known as rotomoulding is a unique process and indeed a unique industry. Rotational moulding is used to manufacture hollow plastic parts as small and complex as a dolls head to as large and simple as a cylindrical 30 kL water tank. The process appears relatively unsophisticated and low technology but may be employed to produce parts that cannot be manufactured with any other process. There were 1410 rotational moulding companies world wide in 2000. It is predicted there will be approximately 1900 rotational moulding companies in the world by 2005 with around 200 operating in Australasia (Nugent, 2001).

A hollow mould of minimum two pieces is fabricated or cast to exactly reproduce the external (mould side) features of the desired part. Moulds for simpler components may be fabricated from sheet steel or aluminium. For more complex components, which require finer tolerances and surface finishes, cast aluminium moulds are used. The first stage in manufacturing a cast mould is to prepare a timber plug in the shape of the required component. A fibreglass pattern of the desired mould is then made on the surface of the plug. The fibreglass pattern is then used to create the sand mould into which the aluminium is cast at a foundry. The only difference between the inside of the mould and the outside of the plastic part is the mould is larger than the plastic part by 1.5 – 3% to allow for shrinkage when cooling. A photograph of a timber plug for a cast aluminium mould for the collector base is shown in Figure 7.1.

Figure 7.1. Photograph of a timber plug for a cast mould

Photographs of one half of the cast mould for the collector base and the first product from the mould are shown in Figure 7.2.

Figure 7.2. Photographs of the cast aluminium base mould and the first product from the mould

The mould is loaded with the required amount of powdered plastic resin and clamped or bolted closed in preparation for moulding. An example of a sheet steel mould for a water tank with the powdered resin loaded and ready for closing up may be seen in Figure 7.3.

Figure 7.3. Photograph of 9000 litre tank mould loaded with polyethylene resin

The mould is then heated by combustion of a fuel gas, electrically or by circulating heating oil through galleries in the mould walls. Gough Plastics use liquid propane gas fired ovens to heat moulds, as do the majority of rotational moulders across the world. During the cooking cycle the mould is rotated about one axis and rocked back and forth about the second axis perpendicular to the rotational axis. In such 'rock and roll' machines, it is necessary to allow some 'dwell' time in the rock cycle where the mould is forced to remain at the maximum rock angle for an extended period to ensure uniform powder distribution on the ends of the product. It is also usual for the direction of rotation to be reversed frequently during the cook cycle to enhance powder distribution. Some modern moulding machines are designed to rotate the mould completely about both axes. These types of machine are referred to as bi-axial rotation machines. A typical mould internal air temperature trace for a collector base component may be seen in Figure 7.4 (oven temperature approximately 300^{o}C).

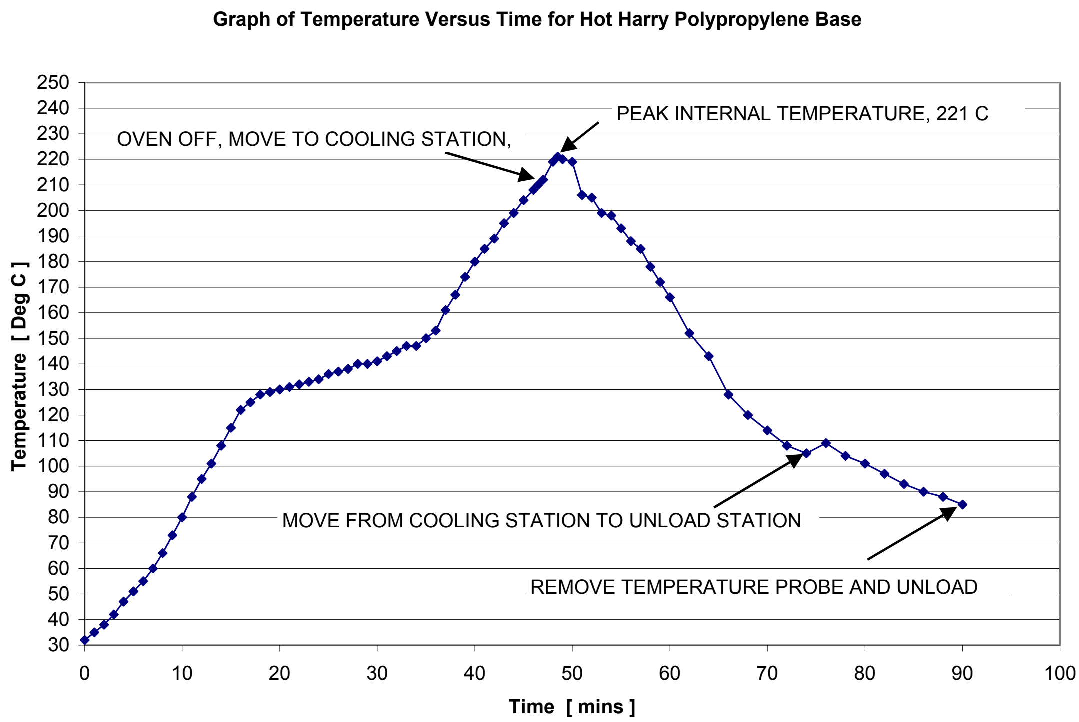

Figure 7.4. Typical mould internal air temperature trace

After sufficient time has been allowed (e.g. the first 18 minutes on trace shown), the resin 'lays up' against the mould walls (18 to 36 minutes on trace) and 'sinters', whereby the resin becomes a homogeneous layer of plastic (36 to 50 minutes on trace). The mould is then removed from the oven and allowed to cool while still rotating (50 to 90 minutes on trace). When the product is cool enough, the operators open the mould and remove the moulded part. The cycle is then repeated. The oven has a carousel with three trolleys, each with a different mould that undergoes the process described above in turn.

7.2 A proposed solution to heater design problems

The development of an integral collector- storage solar water heater presents numerous challenges to the design engineer when considering manufacture of the major components by rotational moulding. Restrictions such as the inability to mould undercuts, the relatively low rigidity and tensile strength of rotomoulding resins and the long term creep characteristics of plastic materials exclude many design features that may be implemented when using traditional materials and processes. In particular, much difficulty may be encountered when attempting to incorporate mechanical fasteners into a rotomoulded product. It is necessary to design the major components of the heater such that ancillary components may be integrated without placing significant stress on the rotomoulded parts. If these restrictions can be overcome, however, rotomoulding provides a very cost effective manufacturing process for relatively low volume production of components.

Other aspects of the solar water heater design are listed below.

- The heater will have a single collector-storage chamber to maximise storage volume.
- The heater will have a clear top surface bounding the storage volume.
- The internal lower surface and sides of the storage volume will be black to minimise reflection of incident radiation.
- The heater will require high performance transparent insulation above the collector-storage component to yield as high as possible performance.
- The heater will allow mains pressure operation in line with market requirements.
- The heater will include a mechanism which will prevent over pressurisation of the storage chamber.
- The heater will require a structure to support the outer cover of the collector and provide additional thermal insulation.
- The heater will have a low profile to be aesthetically pleasing to the eye.
- The outer visible sections of the heater other than the upper glazing will be manufactured in a variety of colours to blend in with the roofing of modern Australian homes.
- The heater will be suitable to be arranged in multiple ‘modules’ to satisfy various levels of demand for hot water.
- The initial model of the heater will not include an auxiliary energy source, such as an electric booster element, and will perform the function of a solar pre-heater.
- The heater will be certified to Australian and New Zealand Standard AS/NZS 2712-2002: Solar and Heat Pump Water Heaters – Design and Construction.

Product certification will allow the heater to be eligible for inclusion into the list of registered solar water heaters maintained by the Office of the Renewable Energy Regular. As such, purchasers of the water heater will be eligible to receive an allocation of Renewable Energy Certificates (RECs) that may be surrendered at the time of sale in lieu of a price rebate. The heater will then also qualify for the Queensland Government Solar Hot Water Rebate Scheme. Details of the product testing and certification process are discussed in Chapter 9 of this thesis.

7.3 System overview

The Hot Harry™ integral collector-storage solar water heater combines the functions of a solar collector and thermal storage container in one chamber. The basic working principle of the Hot Harry water pre-heater is simple. Solar energy is collected and stored within the main water body. A finned heat exchanger tube is immersed within the heat storage water and used to extract the stored energy. Cold water flowing through the heat exchanger tube is heated to a temperature approaching that of the stored water.

The heater is designed to be modular. That is, a system may be comprised of one or more heaters in series depending on performance requirements. Each module contains approximately 150 litres of heat transfer medium. The heat transfer medium specified in this design is water.

An open and in line for assembly drawing of the heater may be seen in Figure 7.5. Note there is no auxiliary energy source or 'booster element' shown in Figure 7.5. The heater is designed specifically to operate as pre-heater to a conventional hot water system, or an in-line instantaneous water heater.

ITEM NO.	QTY.	COMPONENT NAME.
1	1	BASE
2	1	HX INLET
3	2	HX OUTLET / DRAIN
4	2	HX TUBE FITTING
5	1	HX TUBE
6	1	GLASS SEAL
7	1	6mm GLASS
8	43	GLASS CLIP
9	1	1 1/2" UNI SEAL
10	1	CISTERN
11	1	FLOAT VALVE
12	1	FLOAT
13	1	FLOAT VALVE ADAPTOR
14	1	1/4" COMPRESSION FITTING
15	1	1/4" COPPER TUBE
16	22	25mm FOAMING PLUG
17	5	CLIP BACKING STRIP
18	1	HONEYCOMB
19	2	CENTRE POST
20	1	TOP COVER
21	1	RUBBER SEAL
22	1	DOUBLE SIDED TAPE
23	1	3mm ACRYLIC
24	1	CISTERN COVER
25	6	8g x 3/4" S/S PAN HEAD SCREW
26	32	50mm ROOFING SCREW
27	1	1/2" BUNG
28	1	2" UNI SEAL
29	1	50mm VENT
30	1	VENT SLEEVE
31	1	PTR VALVE
32	1	MOUNTING TRAY
33	12	25mm ROOFING SCREW

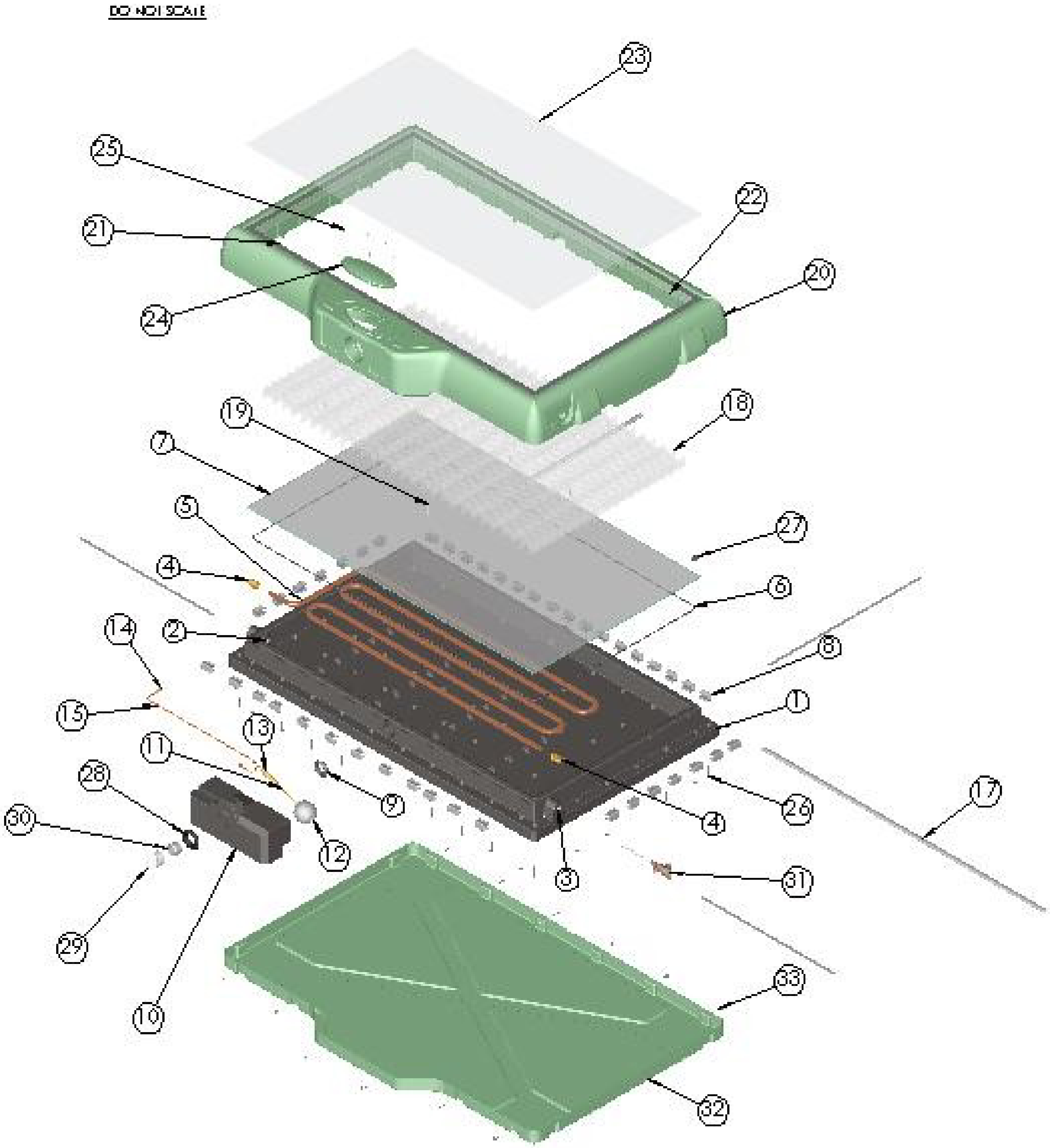

Figure 7.5 Open and in line for assembly drawing of Hot Harry™ heater

A schematic diagram of a typical pre-heater connection may be seen in Figure 7.6.

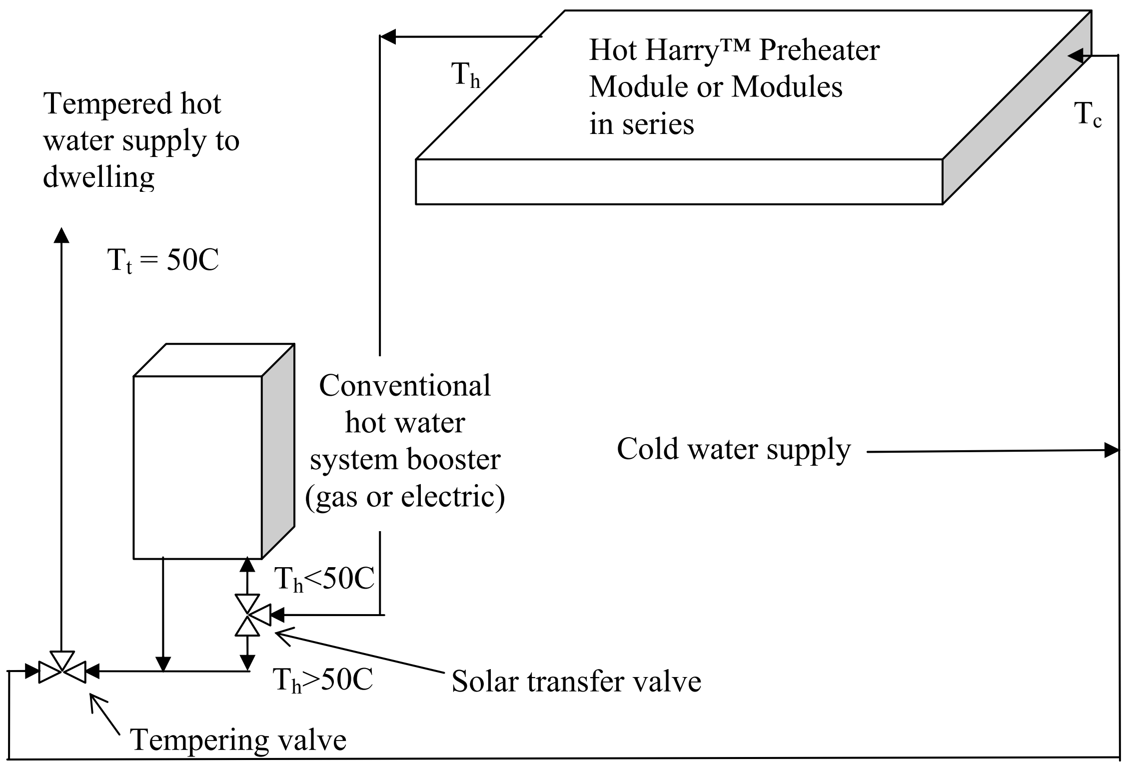

Figure 7.6. Schematic diagram of a typical solar pre-heater connection

One or more Hot Harry™ modules may be connected in series with a conventional gas fired or electrically heated hot water system. The system incorporates a solar transfer valve that may divert pre-heated water to the booster unit or otherwise bypass the booster unit and deliver directly to the tempering valve. The solar transfer valve is a temperature actuated mechanical device that changes modes of operation at approximately 50^{o}C.

A model of the Hot Harry™ has also been designed with an integrated 2400 W electric booster element. A decision was made not to pursue this model until the heat losses from the booster element can be limited to a satisfactory level.

7.4 System components

A brief discussion of the major system components will be given in this section. Interactions with surrounding components and operational issues are described such that materials selection and specification may be justified.

The collector base is black in colour to maximise absorption / minimise reflection of incident radiation. The base includes metallic threaded inserts such that heat exchanger tube connections may be made and a drain plug fitted to the base. A penetration is provided at the rear of the base to allow connection of an expansion reservoir. The base has moulded-in carriers for the heat exchanger tube. The upper and lower parts of the base floor are connected with "kiss-off" features to add stiffness to the product and reduce distortion in service. The base of the heater is rotationally moulded from polypropylene as it has much higher sustained temperature resistance than polyethylene (these two products are the mainstream plastic resins that are economically and commercially available to Australian rotational moulders). The hollow plastic part is insulated with foamed insitu two part polyurethane foam.

The heater operates on a heat exchange principle such that mains pressure water can be heated in a heat exchange tube that segregates it from the collector heat transfer medium. The heat transfer medium in this design is water. The heat exchanger tube is a medium height, finned copper tube that incorporates an undulating inner surface to promote heat transfer. The tube is connected to the inside of the collector base via dezincification resistant brass threaded adaptors. The tube is ordered from the supplier already bent in the serpentine configuration depicted in Figure 7.5. A detailed discussion of the heat exchange tube principles of operation were presented previously in Chapter 5 of this thesis.

A polypropylene expansion chamber that also acts as a make up water cistern is included in the design. The chamber has sufficient volume to allow for normal thermal expansion of the heat transfer medium. The chamber includes a brass float valve capable of automatically maintaining a minimum level of heat transfer fluid in the collector. The float valve has sufficient clearance above the natural overflow level of the chamber to satisfy break-tank air gap requirements as per AS 2845.2:1996.

The inner glazing of the heater will be manufactured from 6 mm thick toughened clear float glass. This is the minimum thickness of toughened glass that may be used in a heater tilted to 30 degrees inclination and maintain the stress in the glass to below the maximum required stress as per AS1288-1994: Glass in buildings – Selection and installation. The glass will be sealed to the base via a 6 mm EPDM o-ring.

The inner glazing is retained on the collector base using 0.8 mm spring steel clips. The design of the clips is similar to a 50 mm fold back paper clip. The clips apply a minimum of 205 N/clip of clamping force on the glazing and base component. A detailed discussion of the design of the spring clips is given in Chapter 8 of this thesis.

A 50 mm high cellulose acetate honeycomb provides the transparent insulation for the collector aperture. The honeycomb sits directly on the 6 mm inner glazing. There is a 5 mm air gap between the honeycomb material and the 3 mm acrylic outer glazing. As shown in Chapter 3 of this thesis, that material combination will afford good thermal insulation as well as very high solar radiation transmission. Support posts made from 10 mm diameter polypropylene rod are used to maintain the 5 mm air gap above the honeycomb.

The top cover of the system shelters the base and transparent insulation system from the elements including hail. It houses the 3 mm high impact acrylic outer glazing. The top cover also houses the vent flap at the rear of the heater. The acrylic sheet is attached to the top cover via a custom designed 'Santoprene' rubber extrusion. The top cover is labelled with all relevant information as required by Standards Australia International Global for compliance with Product Certification guidelines. The cover also carries the product logo at the front of the product. The cover is rotationally moulded from polyethylene and is available in all 'BHP Colorbond' colours to suit Australian roofing systems. Polyethylene is relatively inexpensive (~ ½ price) compared to polypropylene and has excellent resistance to degradation by UV light. As the upper cover is not directly subjected to the high temperatures in the collector-storage tank, polyethylene is suitable for the application. The hollow plastic upper cover part is insulated with foamed insitu two part polyurethane foam to provide further thermal insulation.

8. DEVELOPMENT OF THE INNER GLAZING SPRING CLIPS

The purpose of this chapter is to summarise the development of retaining spring clips for the inner glazing of the Hot Harry™ integral collector-storage solar water heater.

The need to use an elastic or spring type fastening to retain the inner glazing of the collector was recognised during early product trials which incorporated bolted clamps to retain the inner glazing. After a short period in service, it was found that the plastic part deformed around the bolts due to plastic creep under the stress of bolt tension. This deformation caused a reduction in the clamping force applied by the bolts, resulting in water leaking past the glazing seal. A photograph of one of the early trials may be seen in Figure 8.1. Also recognised was the need to design the retaining system such that strain due to load imparted would be kept to the minimum necessary, thus reducing the effect of plastic creep.

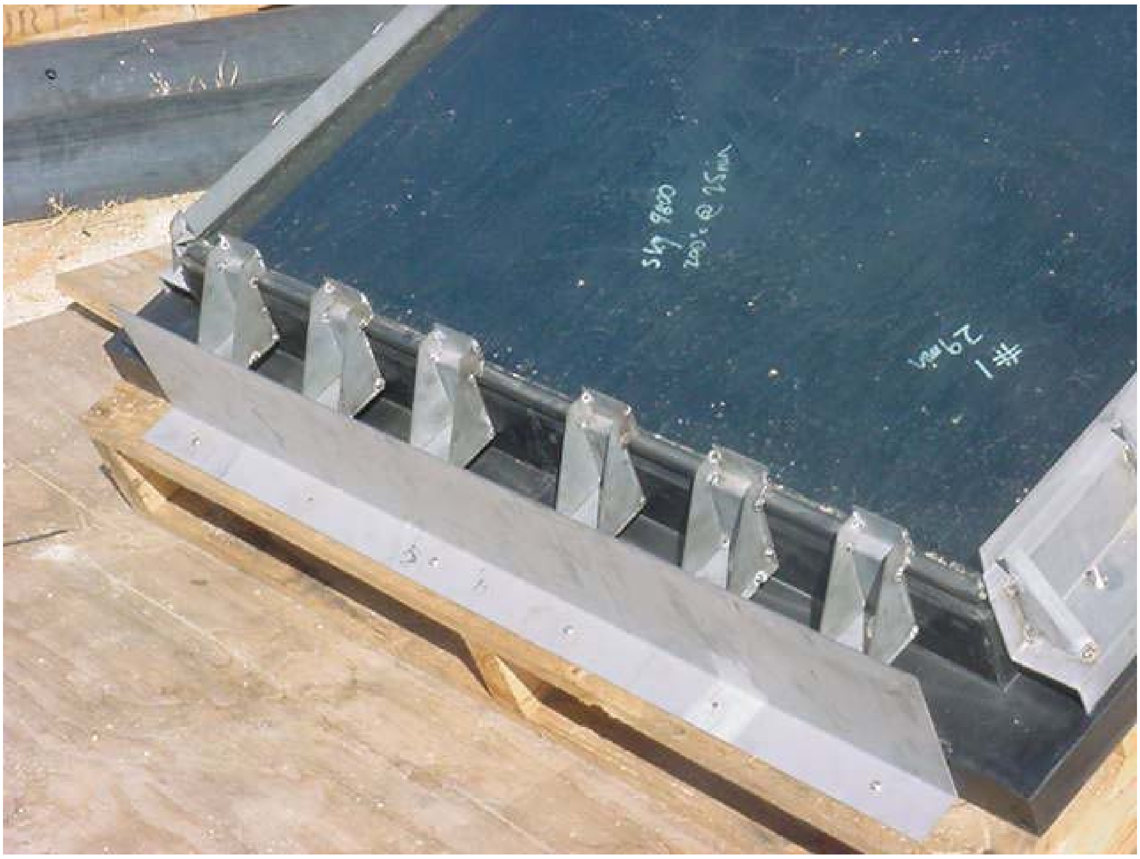

Figure 8.1. Early prototype collector with two variations of bolted clamps to retain inner glazing.

A conceptual drawing of a retaining system based on a fold back clip, designed to overcome the problems encountered with the bolted fasteners, may be seen in Figure 8.2. The design incorporates the elastic element of the paper clip and location of the clip directly below the seal to reduce deformation of the part under load.

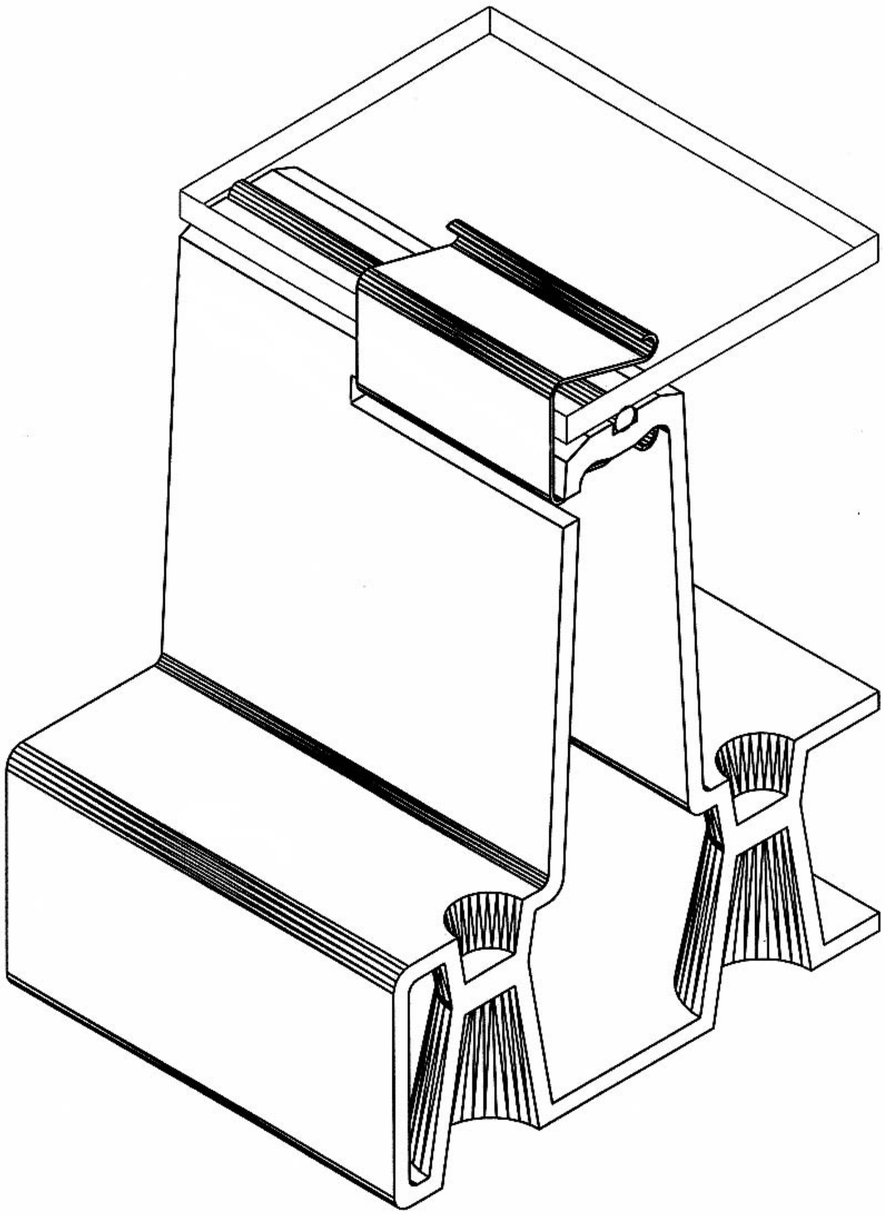

Figure 8.2. Conceptual drawing of retaining system based on fold back clips.

The clamping force provided by the clips is selected to only be as large as necessary, so that the effects of creep are minimised. In addition, if any creep does occur the spring maintains the clamping force, unlike a bolted connection.

The design refinement process for the inner glazing retaining clips proved to be both challenging and rewarding. The author and other product development staff from Gough Plastics have gained invaluable experience in the design of plastic products throughout the course of this design process.

8.1 Function of the spring steel retaining clips

The primary function of the clips is to clamp the inner glazing (6 mm clear toughened glass) of the solar collector to the polypropylene absorber/container with a seal between the two components. The fundamental design of the clips is similar to that of 50 mm fold back paper clips. In fact early prototype trials were conducted using paper clips to demonstrate that the principle of using a spring steel clip to retain the inner glazing was feasible. A photograph of the first prototype trial is shown in Figure 8.3.

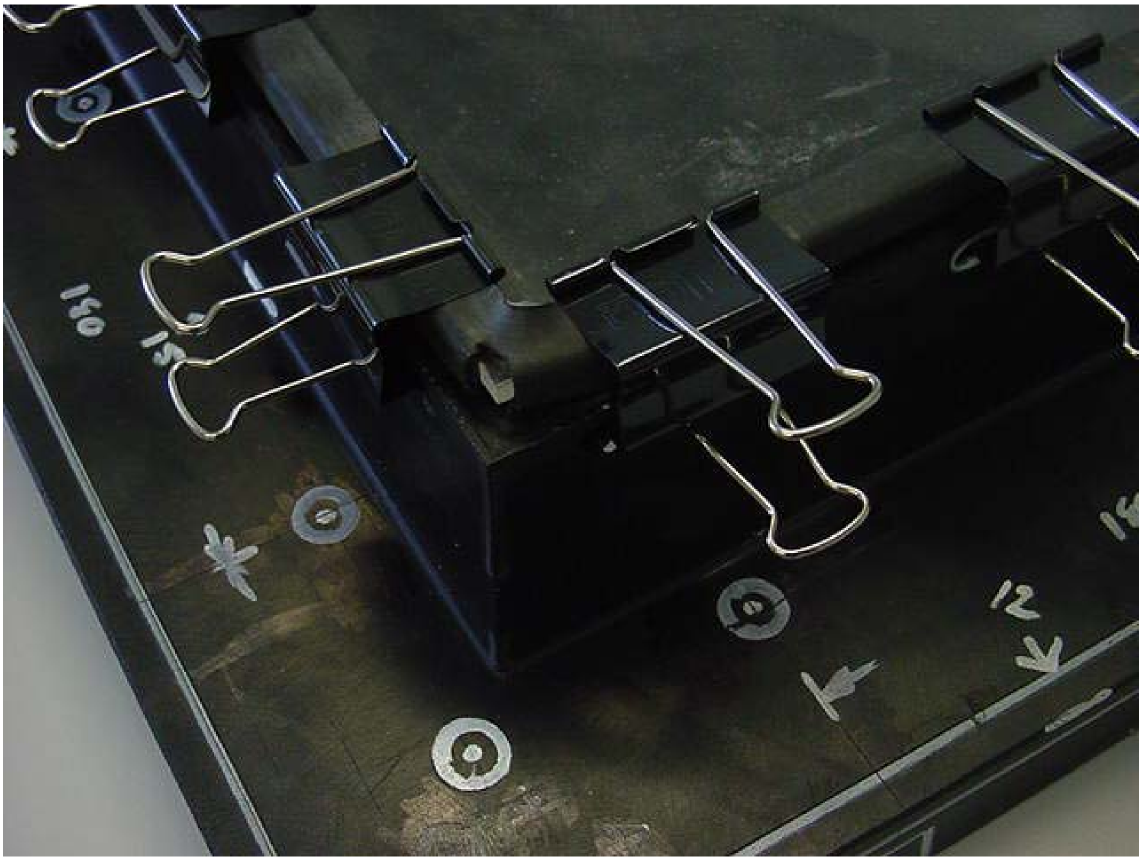

Figure 8.3. 50 mm fold back paper clip trial with rubber U-channel gasket.

The prototype trial was successful and further trials were undertaken to determine that the seal could be effective against the resultant forces due to hydrostatic pressure in the container. A mock corner section of the proposed absorber component was fabricated to facilitate pressure tests and resistance of the sealing arrangement to leakage past the o-ring seal. A photograph of the internal pressure test of the clip and seal arrangement is shown in Figure 8.4.

Figure 8.4. 50 mm fold back clips clamping glazing onto prototype base with 6 mm o-ring (trial section filled with water – approximately 300 mm head).

A preliminary novelty search for such a clip retaining mechanism was conducted by Cullen & Co., (2001). While it was found that the concept of using a spring clip to retain the collector inner glazing is not completely new, the specific application to this water heater is not infringing on any other existing patented designs.

8.2 Preliminary design of a spring clip to retain the glazing

A spring clip was designed to meet the requirements of sealing the collector inner glazing to the absorber. Design parameters such as dimension envelope, nominal spring rate and failure displacement were determined. A functional specification for the design of the clips was written and may be seen in Appendix E. The original design of the clip was based very closely on the design of a 50 mm fold back paper clip with increased material thickness (0.9 mm) to increase the clamping force provided by the clip. Free body diagrams of the collector tilted to 30 degrees may be seen in Appendix F. The maximum reaction force the glazing exerts on the spring clips was found to be 1770 N/m. Spacing the clips in this region at 100 mm centres results in a required clamping force of 177 N per clip to resist the internal hydrostatic pressure. Additional clamping force is required to effect a seal between the glazing and o-ring, and the o-ring and the plastic base component.

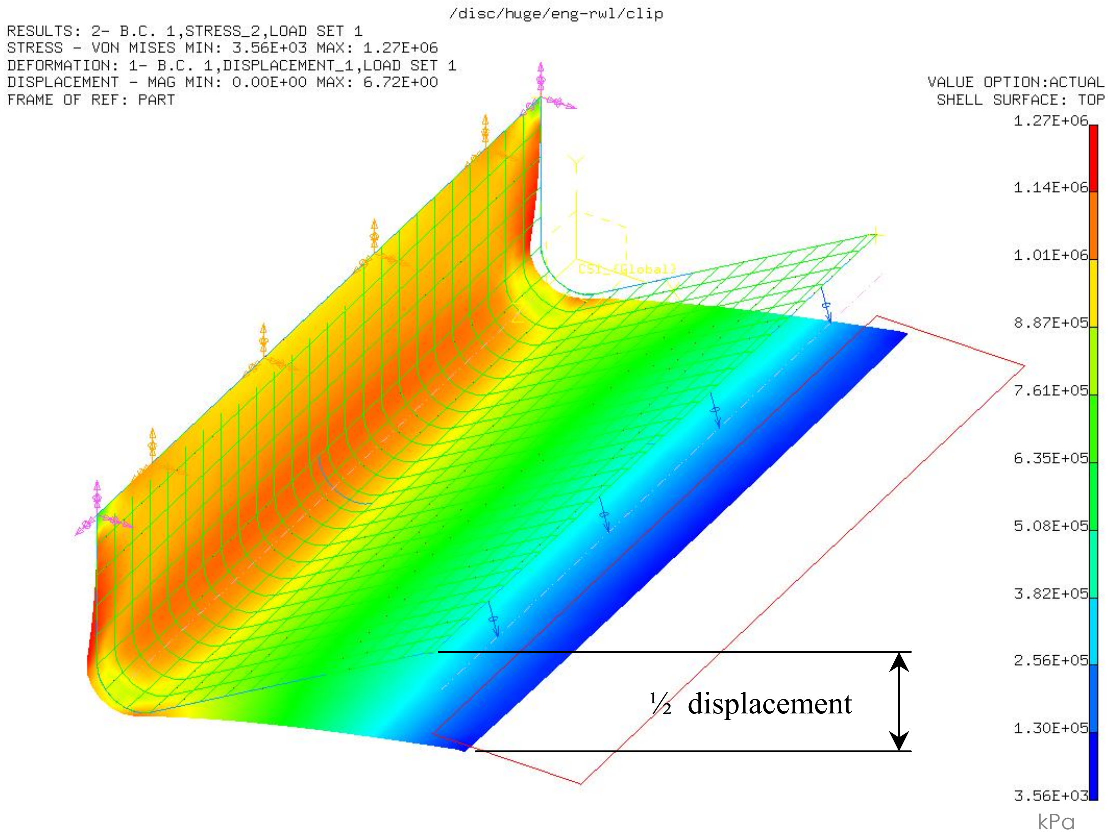

Figure 8.5. Typical stress plot obtained using finite element analysis (13.5 mm displacement of the entire clip).

Finite element analysis was performed on the original design of the clip to determine that the resultant clamping force was acceptable and the stresses within the clip were less than yield strength of the material at fully open position. It was found that for a nominal clamping force of 350 N/clip, the clip displaced approximately 13.4 mm and the maximum von Mises stress in the clip was approximately 1.3 GPa. A stress plot for a symmetric half section of the spring clip showing typical stress contours within the clip during operation may be seen in Figure 8.5. The clip was analysed using IDEAS Master Series 4 finite element analysis software, with parabolic thin shell elements. These findings were acceptable compared with the design criteria for the clip, so a search for a manufacturer of the clips began. With assistance from Russell Clark of Industry Search & Opportunities (a supplier search company), a specialist spring manufacturing company, Thomas Marsh and Co. were approached to assist with development of the spring clip. The functional specification and drawings of the clip were sent to Thomas Marsh and Co. for the manufacture of prototype sample clips.

8.3 Prototype testing and clip design refinement

The first batch of prototype clips received from Thomas Marsh & Co. in July 2001 were manufactured from 0.9 mm annealed steel strip. The clips were heat treated in-house at Thomas Marsh & Co. using an unsophisticated process. The clips were tested for spring rate, failure load by the author using an Instron materials testing machine at James Cook University. A photograph of a clip being tested may be seen in Figure 8.6. The clips were also tested for Rockwell hardness (scale C) in the same laboratory. The spring clips were found to have a lower spring rate than was specified (30 N/mm). Results of the clip testing process may be seen in Table 8.1.

Table 8.1. Results of testing the first batch of prototype spring clips (0.9 mm).

CLIP	AVERAGE SPRING RATE [N/mm]	FAILURE LOAD [N]	FAILURE DISPLACEMENT [mm]	AVERAGE HARDNESS ROCKWELL ' C '
1	21.2	324	15.3	36.4
2	19	286	14.9	29
3	22.1	286	12.8	20.2
AV.	20.8	299	14.3	28.5

Figure 8.6. Clip being tested on Instron materials testing machine at JCU.

Yield displacement of the clips was also less than specified due to poor control of the hardening and tempering process. The clips needed to be hardened to approximately 45 HRc to withstand the stresses imparted during installation with some margin for safety. This level of hardness gives an approximate yield strength of 1460 MPa and was determined from literature supplied by Firth Cleveland Steel Strip (2001) as well as the efunda website (see Appendix G for efunda hardness conversion). A photograph of the hardness testing may be seen in Figure 8.7.

To increase the spring rate of the clips and increase the yield strength, a second batch of prototype clips were ordered, to be manufactured from 1.0 mm annealed steel strip and hardened to 45 Rockwell ‘C’. The clips were received on 25 July 2001, and were immediately tested for physical and mechanical properties as with the first batch. Results of testing the second batch of prototype clips may be seen in Table 8.2.

Table 8.2. Results of testing the second batch of prototype spring clips (1.0 mm).

CLIP	LOAD WHEN OPEN TO 14 mm GAP [N]	LOAD WHEN OPEN TO 18.5 mm GAP [N]	LOAD WHEN RETURN TO 14 mm GAP [N]	NOMINAL SPRING RATE 'K' [N/mm]	AVERAGE HARDNESS ROCKWELL 'C'
1	388	548	372	33.2	43.6
2	386	544	370	33.0	43.2
3	378	528	358	32.0	42.9
4	382	538	366	32.7	42.8
5	378	534	362	32.3	43.6
AV.	382.4	538.4	365.6	32.6	43.22

Note the relative uniformity of the results from the second batch of clips compared with the first batch of prototype clips. The primary reason for this is because the second batch of clips were hardened and tempered by specialists using a well controlled process. This second batch of clips design were accepted as complying with the current specification. An order was placed for mass production tooling of the clips, along with an order for 1000 clips.

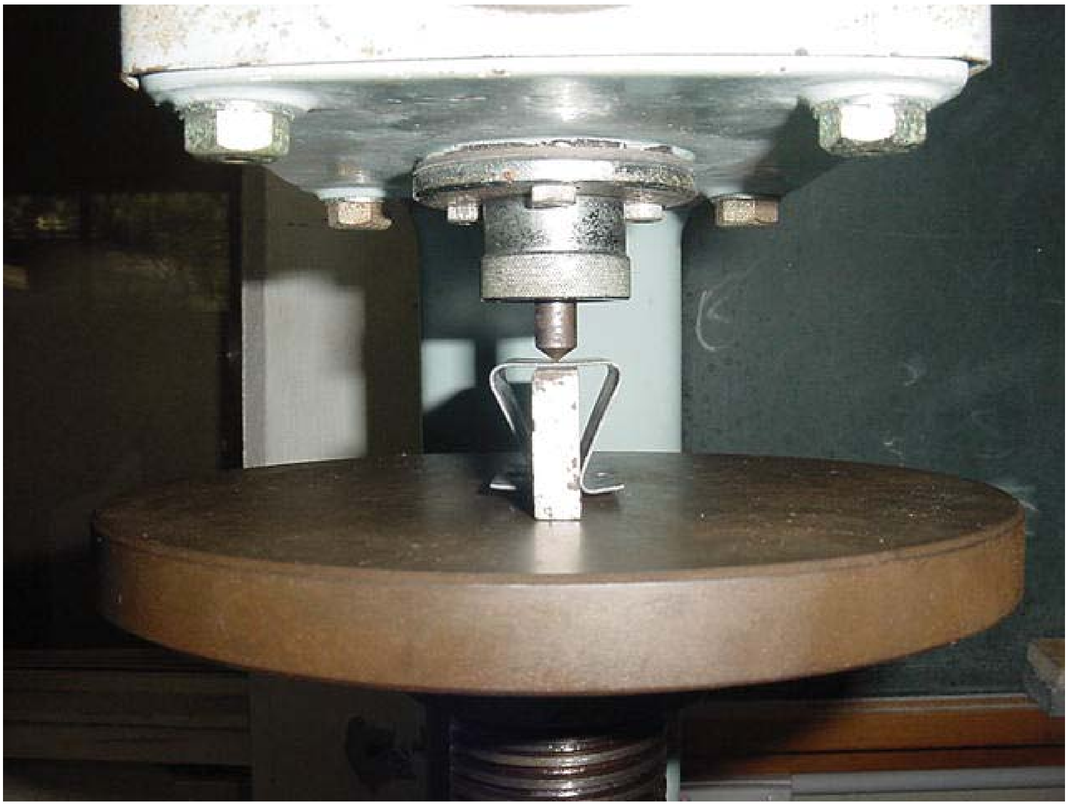

Figure 8.7. Clip being tested for Rockwell hardness at JCU.

By the time the first bulk order of 1000 clips arrived at Gough Plastics factory, the rotomoulded collector storage component had been developed. Trials were carried out to determine the ability of the clips to sustain a seal against the hydrostatic pressure applied at maximum tilt angle of the collector.

According to AS/NZS 2712 (2002), the collector must to be tested at a tilt angle resulting in 1.5 times the pressure at recommended maximum tilt angle. A photograph of the first prototype collector at 30 degrees tilt angle being filled with water may be seen in Figure 8.8. Calculation of the reaction forces on the glazing for tilt angle of 30 degrees may be seen in Appendix F.

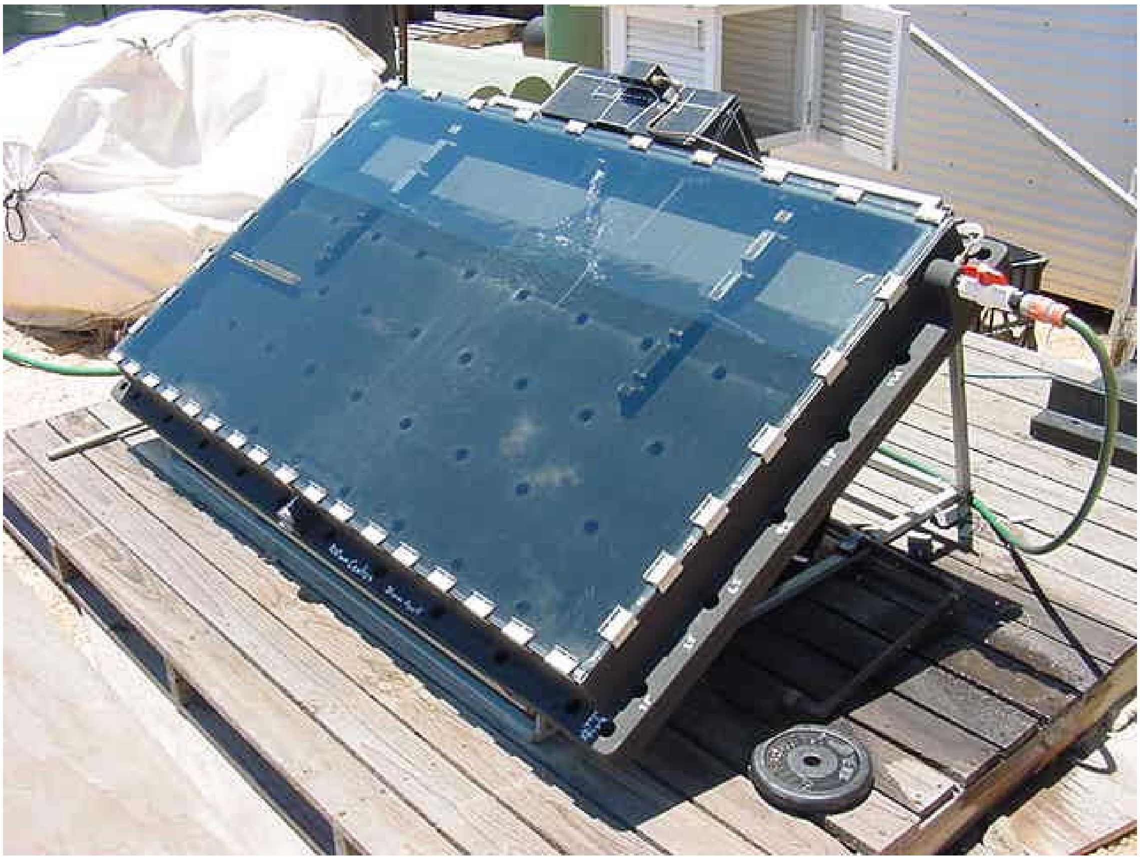

Figure 8.8. First prototype collector being filled with water (6 February 2002).

The 1.0 mm clips were used to assemble several field trial solar hot water systems. After several months of exposure to service conditions, the field trial units began to leak, seemingly at the o-ring seal. After disassembling the trial units, it was found that cracks were forming in the polypropylene part at the o-ring groove due to excessive clamping force from the spring clips. The need for modification of the polypropylene base component became apparent, in particular the radius in the corners of the o-ring groove. This detail of component design was assessed using finite element analysis CosmosExpress, a design check tool integrated in Solidworks solid modelling and drafting software. Due to assumptions employed in the finite element analysis (e.g. linear material behaviour) the results of the analysis are expected to yield conservative (high) stress results.

Finite element analysis showed that the 1.0 mm clips were causing stresses of almost 21 MPa in the polypropylene base component. Increasing the radius in the o-ring groove from 0.6 mm to 1.2 mm reduced the stress in the plastic part to approximately 13 MPa. A further increase of radius to 2.0 mm resulted in the stress falling to approximately 9.9 MPa. The clip force applied to the part in the three aforementioned analyses was 424 N/clip. A schematic diagram indicating the pressure field distributions applied to the finite element model may be seen in Figure 8.9.

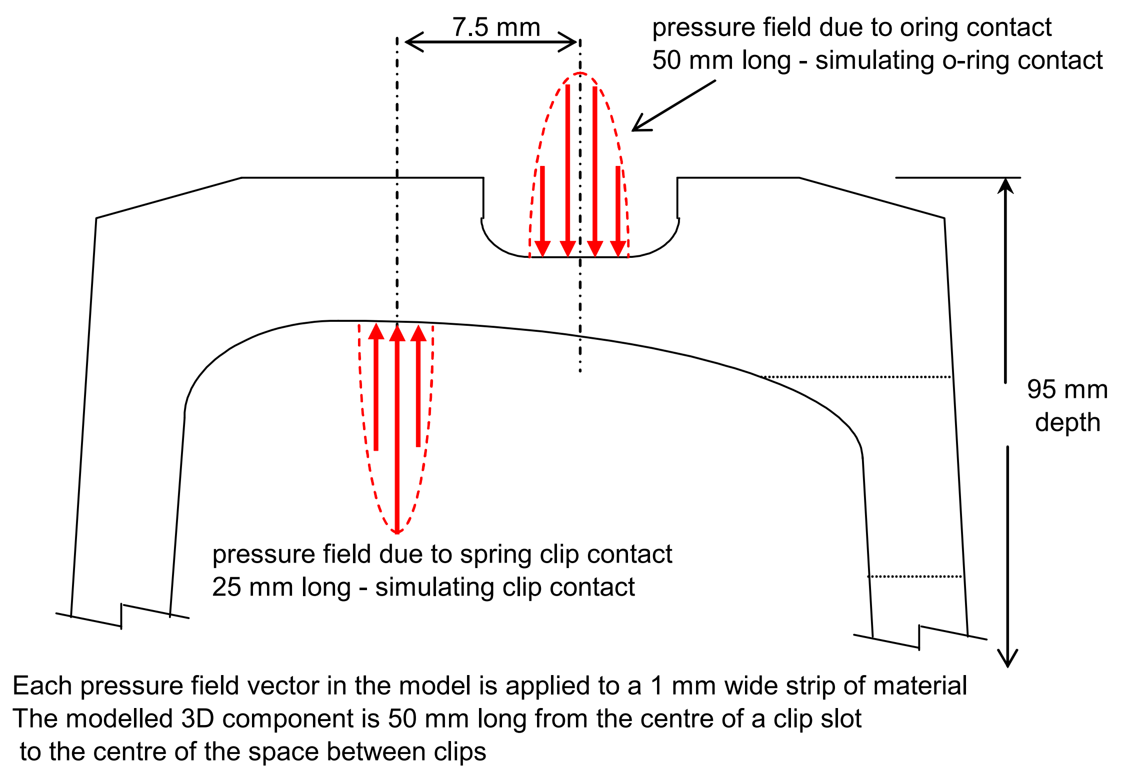

Figure 8.9. Schematic diagram indicating pressure field distributions used in finite element analysis of the polypropylene base component.

Increasing the shot weight of the polypropylene base from 20 kg to 30 kg caused a theoretical increase in clamping force to 496 N/clip due to an extra 2.2 mm of material added to the wall thickness of the part in the region of contact with the clip. Regardless of the larger clamping force, the additional material provided a further decrease in stress to approximately 5.5 MPa. That value seemed to be the minimum achievable stress given the current configuration of the base and clip. No further increase of groove radius was possible because of the difficulty of access to the o-ring groove detail in the mould. Nor was any significant increase in component shot weight possible due to the mould volume being completely filled with powdered resin when loaded at 30 kg shot weight. A stress plot from the latter finite element analysis is shown in Figure 8.10.

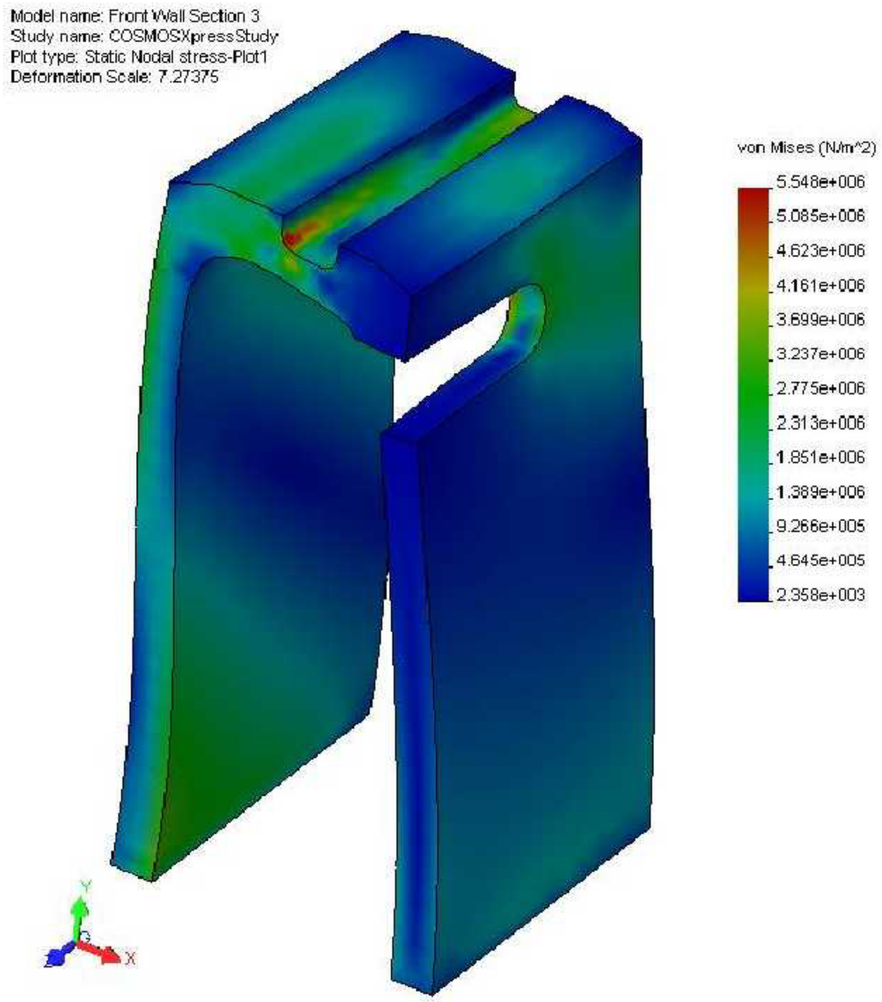

Figure 8.10. Stress plot from finite element analysis of 30 kg base with 2 mm radius in o-ring groove and 1.0 mm clip applying 496 N clamping force.

So far, all finite element analysis had been performed assuming the collector to be at zero tilt angle. At zero tilt angle, no unloading of the o-ring pressure results from the internal hydrostatic pressure on the glazing (as if the collector were empty). This represents what was assumed to be the worst case scenario when considering the stress in the o-ring groove of the polypropylene base component.

The allowable long term hydrostatic stress in the plastic base component was assessed from curves published by George Fischer (1996). The allowable stress is dependent on both service temperature and required lifetime. An effective constant long term temperature was calculated from recordings of a typical collector temperature profile over several days with no load withdrawal. Fixing the required lifetime of the product to a minimum of 10 years yielded a maximum allowable stress of 2.6 MPa in the plastic base component. A reproduction of the long term hydrostatic stress curves may be seen in Appendix H.

To further reduce the stress in the polypropylene part to an acceptable level, Thomas Marsh & Co. were issued with an order for a sample batch of clips made from 0.81 mm material. The clips were tested for physical and mechanical properties at James Cook University and the results of the testing may be seen in Table 8.3.

Table 8.3. Results of testing the third batch of prototype spring clips (0.81 mm).

CLIP	INITIAL OPENING OF CLIP AT REST [mm]	LOAD WHEN OPEN TO 17 mm GAP [N]	LOAD WHEN OPEN TO 20 mm GAP [N]	LOAD WHEN RETURN TO 17 mm GAP [N]	NOMINAL SPRING RATE ‘K’ [N/mm]
1	3.1	232	285	228	16.4
2	2.1	256	310	251	16.8
3	2.7	238	290	232	16.2
4	2.2	244	298	242	16.4
5	3.2	224	276	220	15.9
AV.	2.66	239	292	235	16.35

An assessment of the stress within the spring clips was performed using finite element analysis package CosmosExpress. Naturally the stress developed in clips decreased with material thickness for any given displacement.

In addition to maximum von Mises stress, each of the three clips (1.0, 0.9 and 0.8 mm thick material) were assessed for spring rate at various displacements. Results of the finite element analyses may be seen in Appendix I. An example of a stress plot from the finite element analyses may be seen in Figure 8.11.

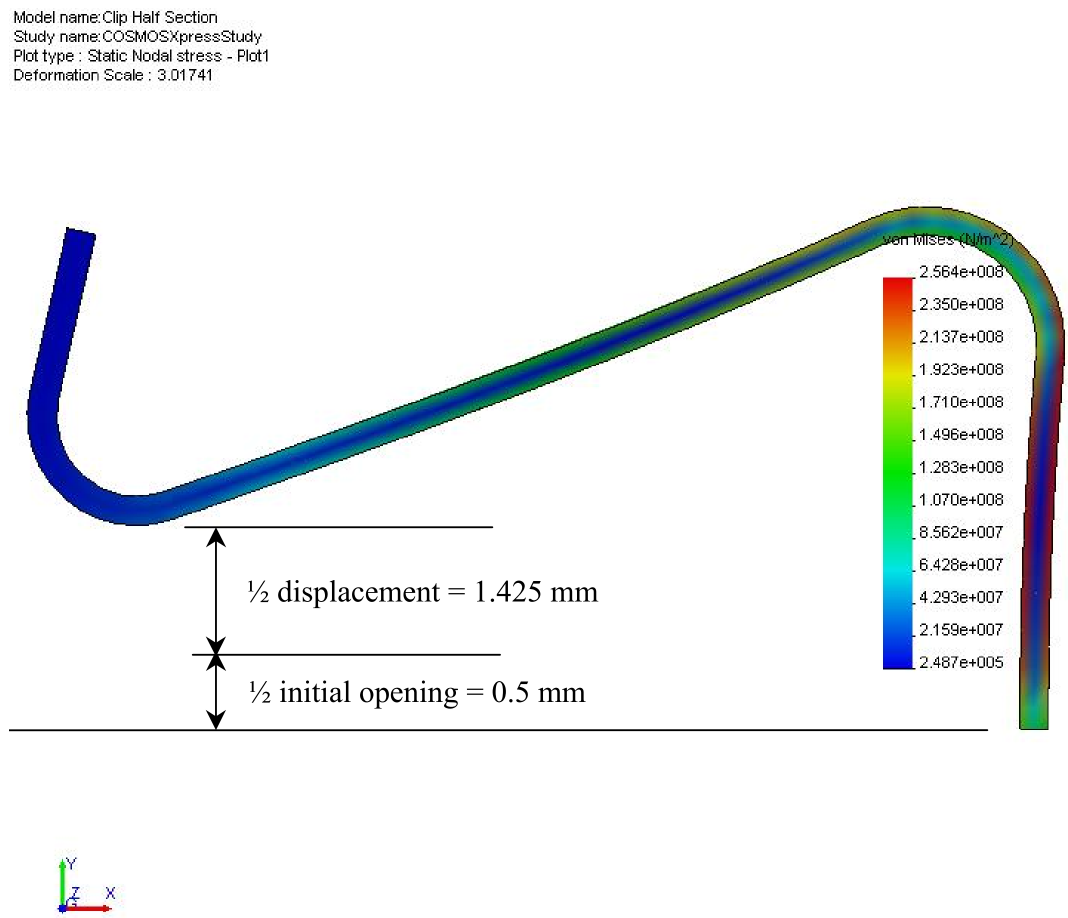

Figure 8.11. Example of von Mises stress in symmetric section of 0.8 mm spring clip at 2.85 mm total displacement (approximately 48.5 N clamping force).

With the knowledge gained through the process of spring clip design, it was decided that no further optimisation of the spring clips was required. Given the maximum predicted stress in the polypropylene (5.6 MPa) was greater than the allowable stress (2.6 MPa), it was necessary to find a method to further reduce the stress. The option of incorporating an aluminium extrusion into the product and thus reducing stresses through more uniform clamping force on the plastic part was investigated. The results of this investigation are discussed in the following section of this chapter.

8.4 Design and Analysis of the Aluminium Clip Backing Strip

To better distribute the clamping force applied by the spring clips, an aluminium backing strip extrusion was proposed, to be installed under the o-ring groove of the polypropylene base component. Initial calculations were performed to optimise the geometry of the aluminium backing strip, making full use of the available space within the walls of the plastic part. A schematic diagram of the wall section and backing strip may be seen in Figure 8.12.

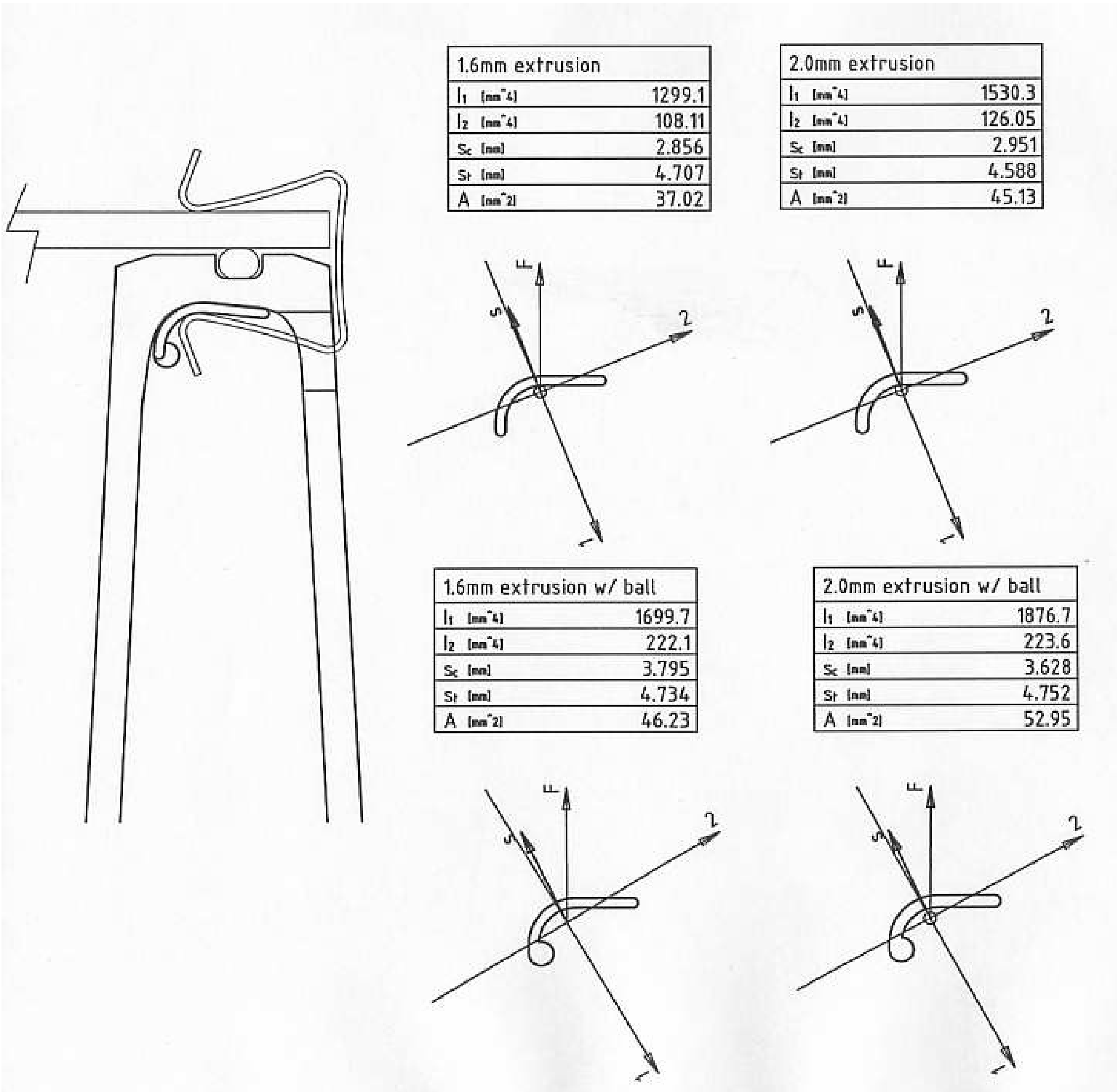

Figure 8.12. Schematic development of aluminium backing strip for uniform distribution of clamping force applied by spring clips.

Although inclusion of the backing strip increases the clamping force due to 2 mm additional displacement of the clip, the advantage of distributing the clamping force more evenly onto the plastic part was considered positive. Considering the stiffness of the aluminium strip compared with the plastic part, the clamping force will be shared both laterally and longitudinally above the backing strip.

The effect of the aluminium backing strip on the stress in the polypropylene was assessed by incorporating the strip into the finite element model. A schematic diagram indicating the pressure field distributions applied to the preliminary finite element model including the backing strip may be seen in Figure 8.13.

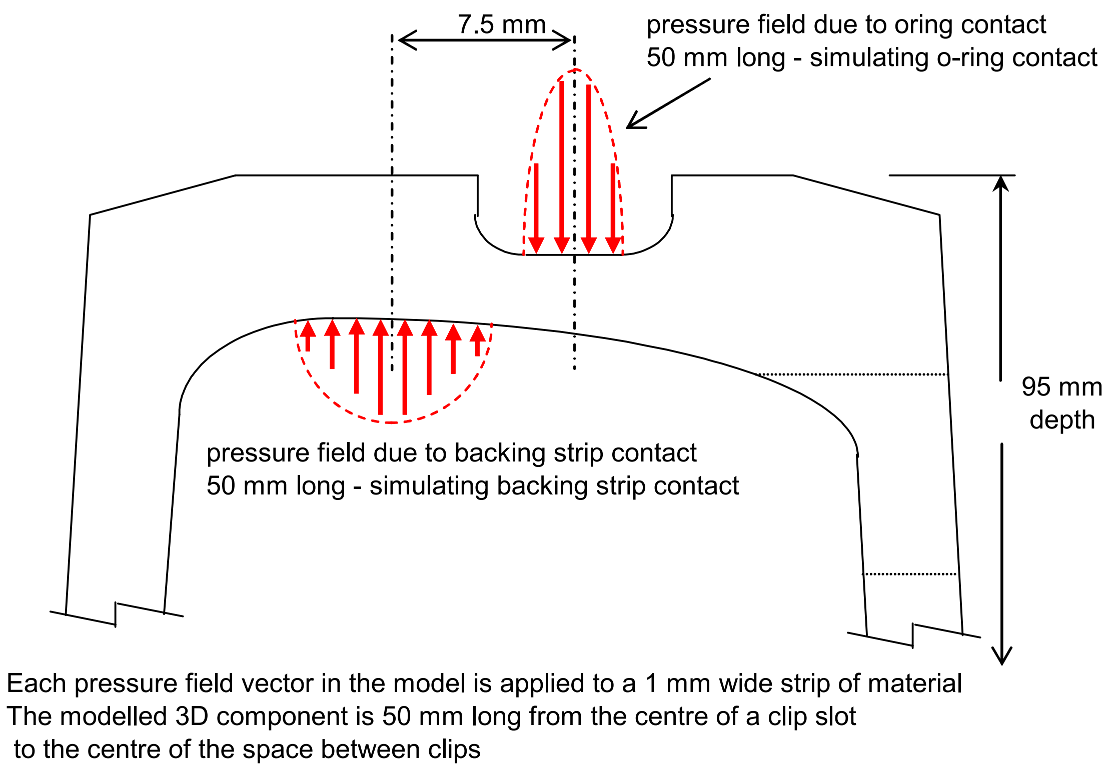

Figure 8.13. Schematic diagram indicating pressure field distributions used in finite element analysis incorporating aluminium backing strip.

Also consider that as the aluminium backing strip becomes loaded, the plastic part above it would deform to the shape of the aluminium. This would further distribute the contact pressure from the strip to the plastic part, possibly to the very extremes of the aluminium strip.

For the sake of completion and confidence an approximate model of the backing strip was included in the finite element model with contact boundary conditions applied. CosmosWorks finite element analysis software was used to model the base component and backing strip. Typical stress plot results may be seen in Figure 8.14.

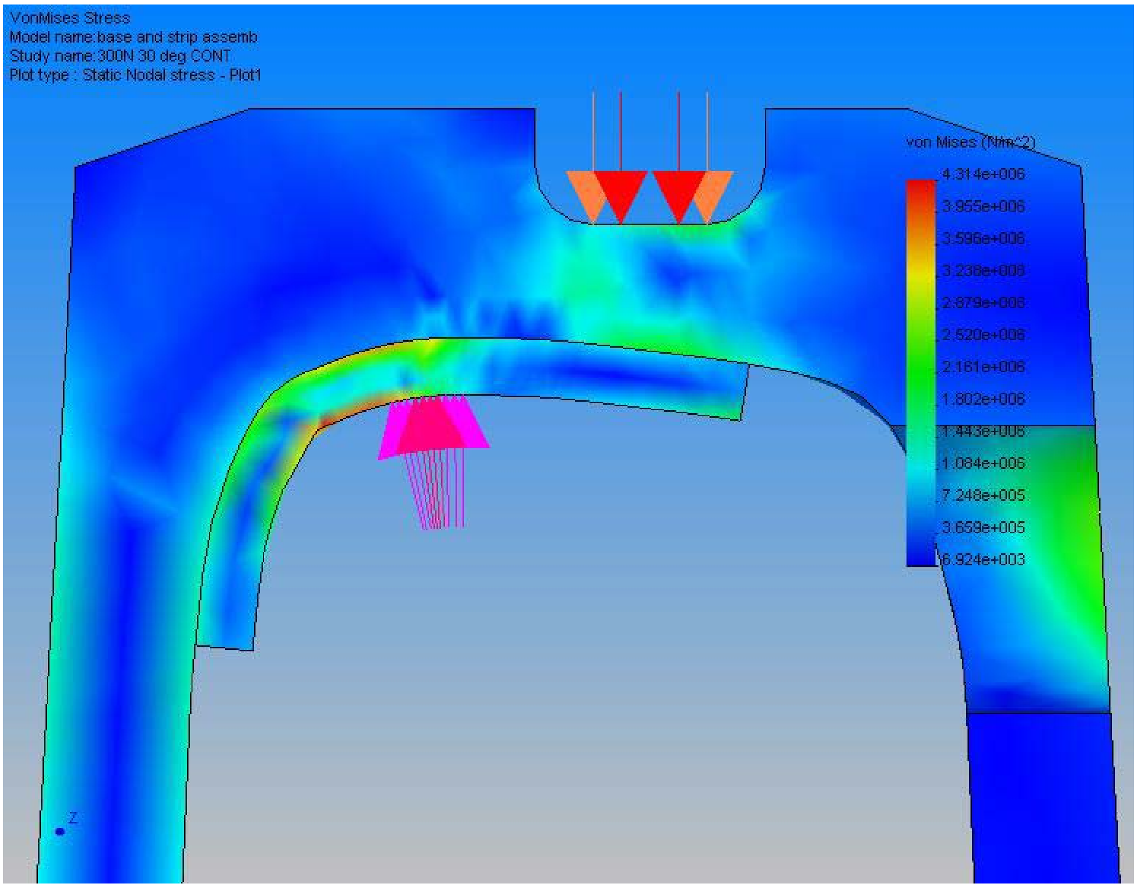

Figure 8.14. Example stress plot from CosmosWorks finite element analyses with aluminium backing strip and contact boundary conditions.

Instead of applying loads which relate to the clamping force applied by the various clips, nominal clamping forces of 200, 250 and 300 N were applied to the model to bracket the possible clamping forces likely to be employed. Cases of zero tilt angle and 30 degrees tilt angle were analysed. The results of the analyses may be seen in Table 8.4.

Table 8.4. Results of Finite Element Analysis including backing strip.

Clip Force [N]	Tilt Angle [degrees]	Von Mises Stress [MPa]		
		In Groove	Under Groove	In Slot
200	0	1.7	1.9	1.6
200	30	2.5	1.6	3.2
250	0	2.1	2.4	1.9
250	30	2.6	1.7	3.3
300	0	2.5	2.9	2.3
300	30	2.8	1.8	3.4

The peak stress region of most interest in the analysis is in the groove, as both under the groove and the clip slot are separated from contact with the hot water inside the collector storage chamber. Therefore the allowable long term hydrostatic in these regions is increased. Note the legend shown in the above stress plot (Figure 8.14) shows the maximum stress in the assembly. The maximum stress occurs where the concentrated clamping force of the spring clip is applied to the underside of the aluminium backing strip. Initially, this caused some difficulty in determining the stress in the plastic part alone. The aluminium backing strip was able to be hidden in the stress results window and the stress in the plastic part determined by using a design check tool. A sample of the design check plots may be seen in Figure 8.15.

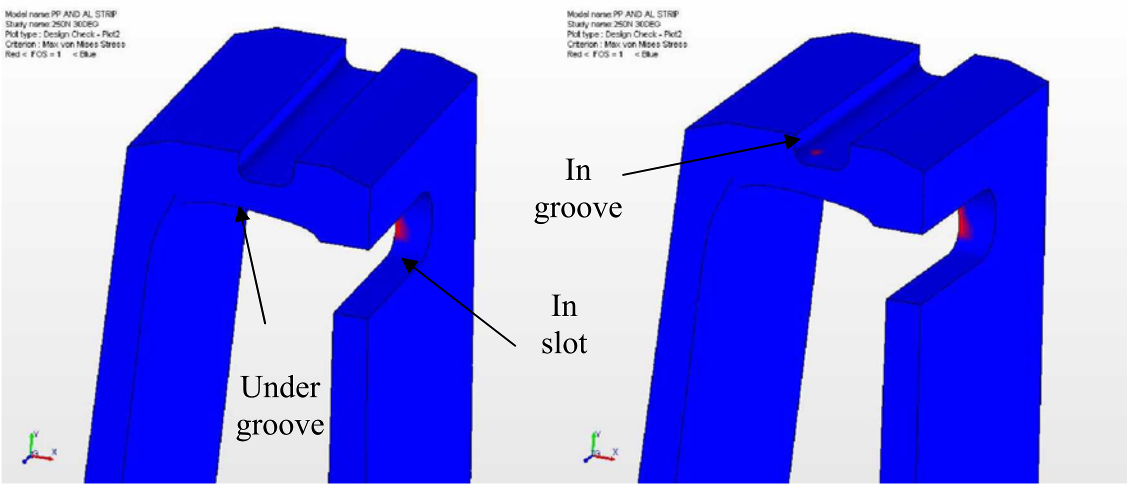

(a) (b)

Figure 8.15. Example of Design Check Plots.
(a) Design check with 2.6 MPa specified as yield stress.
(b) Design check with 2.5 MPa specified as yield stress.

The design check tool allows the user to specify a level of yield stress and factor of safety. The resulting plot highlights all areas in the model where the stress exceeds the product of the yield stress and factor of safety. A summary of each progression of the design and analysis discussed in this report may be seen in Appendix J.

Considering that the linear finite element model will overestimate the stress for a viscoelastic material (as it neglects the stress redistribution between high and low stress areas), the results appear quite satisfactory. Testing of the base with the increased shotweight of 30 kg and backing strip suggest that the problem of cracking at the o-ring groove may have been overcome. Accelerated full scale product testing is underway to confirm the product performance prior to release. The tests so far indicate the actual stress in the base component is low enough to avoid premature failure in the field.

Coupling the knowledge gained from the above contact analysis with that from the testing and analysis of the spring clip allows specification of a combination of components. The finite element results indicate that the addition of the backing strip in conjunction with 0.8 mm clips reduces the stresses in the polypropylene significantly, to or below the allowable stress levels. A detailed sensitivity analysis with respect to manufacturing tolerances of the component combination may be seen in Appendix K.

9. PRODUCT CERTIFICATION AND RECS ASSESSMENT

Product certification is an important aspect of manufacturing and marketing of any product. Meeting the relevant levels of approval allows consumers to have confidence that the product they are considering is manufactured with quality components using a quality controlled process. The basic level of product certification for solar water heaters is WaterMark approval, which allows connection of a plumbing product to a mains supply water system. However, to also qualify for inclusion in the list of registered solar water heaters maintained by the Office of the Renewable Energy Regulator, a heater must attain StandardsMark approval to AS/NZS 2712:2002 - Solar and Heat Pump Water Heaters – Design and Construction. Certification to this standard allows consumers to claim Renewable Energy Certificates (RECs) against their purchase as well as State Government rebates. This chapter discusses the process by which the Hot Harry™ integral collector-storage solar water heater was tested for compliance to AS/NZS 2712:2002. StandardsMark approval is issued by Standards Australia International Global Limited (SAI Global).

9.1. StandardsMark approval requirements

To gain product certification to AS/NZS 2712:2002 it must be proven that all relevant requirements are satisfied. There are several broad requirements within the standard to be addressed as follows:

- Compliance with the requirements of AS 3498:2003 Authorisation requirements for plumbing products – water heaters and hot water storage tanks (WaterMark).
- Performance testing of the solar collector as per AS/NZS 2535.1:1999 Test methods for solar collectors – Thermal performance of glazed liquid heating collectors including pressure drop.
- Type testing of the solar collector as per Australian Standard AS/NZS 2712:2002 - Solar and Heat Pump Water Heaters – Design and Construction, including resistance to stagnation temperature conditions.

- Performance evaluation of the solar collector as per Australian Standard AS 4234:1994, Solar water heaters – Domestic and heat pump – Calculation of energy consumption.

In addition to the above requirements, documentation of quality control and procedural issues related to company management must be presented to SAI Global.

9.2 Product certification testing

The Hot Harry™ integral collector-storage solar hot water system was tested for compliance with the above requirements by the staff of Plumbing Testing Laboratories Pty Ltd (PTL), a division of WaterCorp, the local water supply authority of Perth, Western Australia. A photograph of a collector in the solar simulation test chamber at the PTL facility is shown in Figure 9.1.

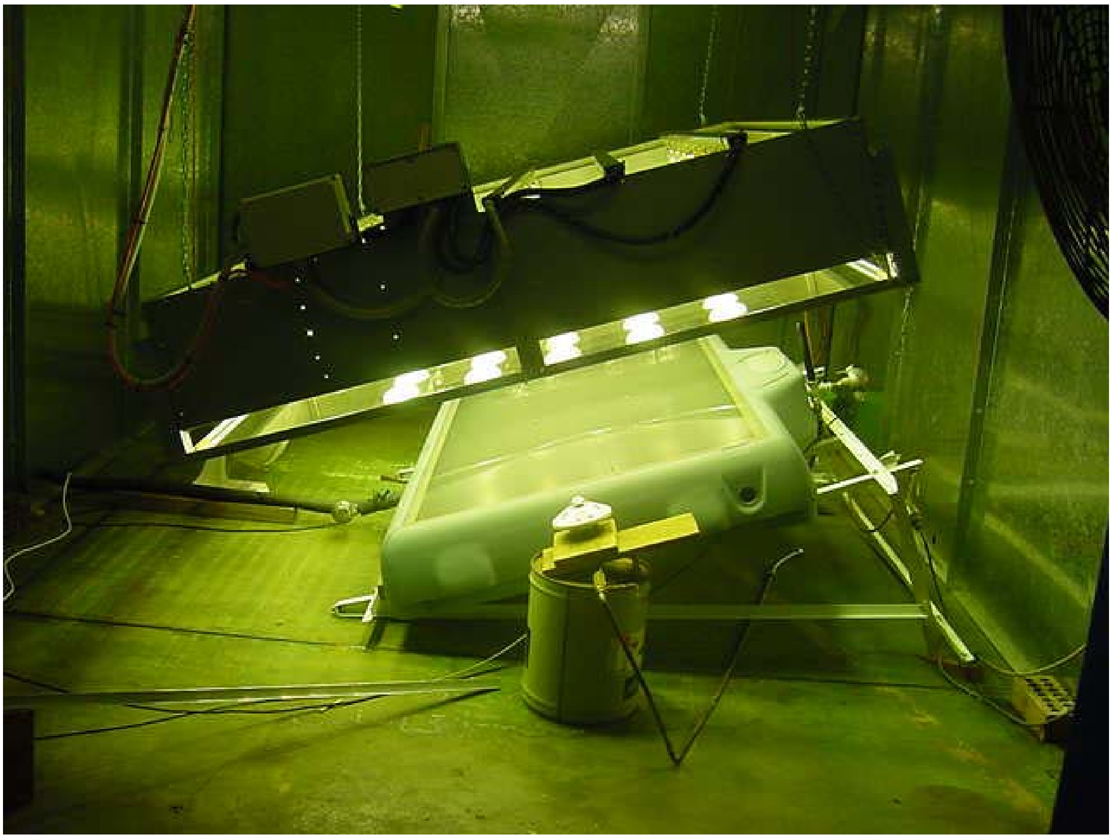

Figure 9.1 Collector in solar simulation chamber at PTL in Perth.

The solar simulator chamber is purpose built to produce conditions required for the resistance to stagnation temperature test as per AS/NZS 2712:2002. The stagnation temperature is that which is reached when the incident radiation and ambient temperature are at extremes and no energy is drawn from the collector. The simulated radiation is maintained at a minimum of 1200 W/m^2 for 12 hours, followed by 12 hours of no radiation. This cycle is repeated for 10 days. The ambient air temperature in the chamber is maintained at a minimum of 40^{o}C for the entire test. The collector is then assessed for any signs of permanent damage and for change in performance characteristics.

Prior to stagnation testing, the solar collector was tested to determine its performance characteristics as per the tests prescribed in AS/NZS 2535.1:1999. The indoor collector performance testing was supervised by Dr. Trevor Pryor of Murdoch University, Perth. The large thermal mass of the Hot Harry™ collector (equivalent to approximately 164 kg of water) precludes the heater from being assessed under the usual outdoor thermal performance tests. Modifications were made to the solar simulator chamber so that performance testing could be completed indoors. The simulator was fitted with a low iron glass filter to prevent radiation of wavelength greater than approximately 3 μm from the artificial lights reaching the collector surface. For the indoor performance testing the Hot Harry™ heater was operated as a collector with water inflow into the chamber through the drain plug and water outflow through the chamber cistern outlet.

The simulator radiation spectrum had a greater fraction of energy at longer wavelength than is present in outdoor solar radiation. This reduced the radiation transmission through the acrylic outer glazing and required a correction to be applied to the results (see AS2535.1:1999, Sect 9.2). Details of the correction may be seen in Appendix L.

The indoor simulator test suggested a corrected normal incidence optical efficiency of 0.83 and a typical collector heat loss coefficient of 3.3 $W/m^2.K$. The collector heat loss coefficient was verified in a further separate test where the heater was filled with hot water of uniform temperature and allowed to cooled down, the average water temperature and ambient temperature were measured (see Appendix M for details). A plot of the collector heat loss coefficient measured in this test is shown in Figure 9.2.

The below graph is based on the first 40 hours of the heat loss test (8 April 18:00 h to 10 April 10:00 h) where the heat loss coefficient has been evaluated as a moving average over 2 hour periods.

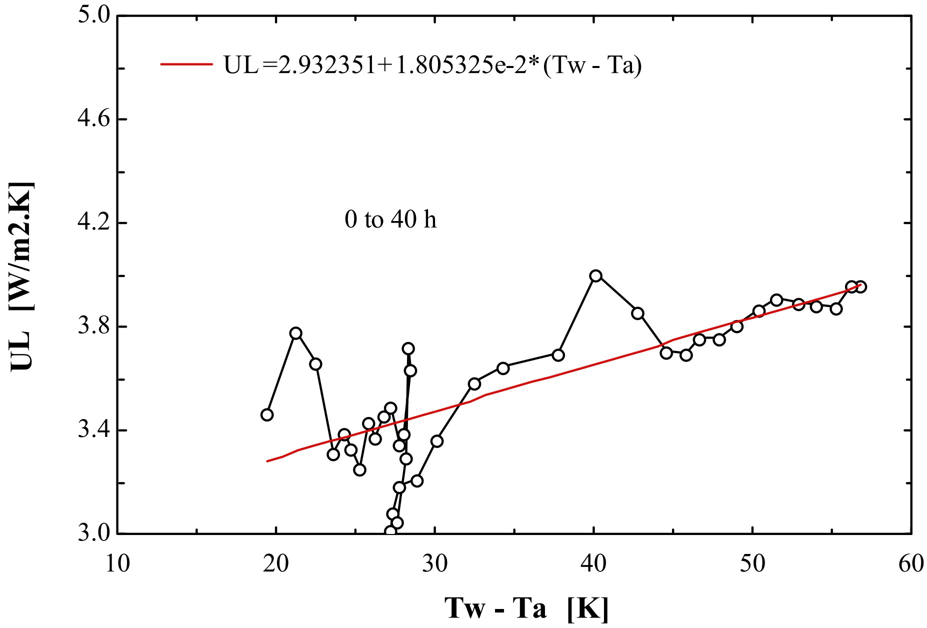

Figure 9.2 Collector heat loss data and fitted curve

The heat loss coefficient for the collector is:

$$U_L = 2.93 + 0.018(\mathrm{T_w} - T_a) \tag{9.1}$$

The resulting expression from indoor simulator and collector heat loss test for the Hot Harry collector overall normal incidence efficiency η_{oa} is:

$$\eta_{oa} = \eta_0 - a_1 \frac{(\overline{T}_w - \overline{T}_a)}{G} - a_2 \frac{(\overline{T}_w - \overline{T}_a)^2}{G} \tag{9.2}$$

where, $\eta_0 = 0.83$ is the optical efficiency of the collector

$a_1 = 2.93$ is the collector heat loss first order coefficient in W/(m^{2}K)

$a_2 = 0.018$ is the collector heat loss second order coefficient in W/(m^{2}K^2)

$\overline{T}_w$ is the mean collector storage fluid temperature in ^{o}C

$\overline{T}_a$ is the ambient temperature in ^{o}C

G is the incident radiation in W/m^2

Equation 9.2 may be used in evaluation of the performance of the unit, to determine the solar fraction and to calculate the RECs allocation for a nominated configuration and location.

The incidence angle modifier was measured in a separate outdoor test of the outer glazing and transparent insulation (ref Appendix L). The resulting expression for the Hot Harry™ heater is:

Incidence angle modifier $K_{\tau\alpha} = 1 - 0.27\left(\dfrac{1}{\cos(\theta)} - 1\right)$ (9.3)

To further verify the predicted performance of the heater from equation 9.2, an outdoor test measuring the temperature rise of the storage water was performed (see Appendix M for details). Using the heater model shown in equation 9.4 and the performance parameters predicted by equations (9.2) and (9.3), allowed the integrated heater performance to be simulated and compared to the performance measured in the outdoor test. The result for three successive days is shown in Table 9.2

$$mC_p \frac{dT}{dt} = A_c[K_{\tau\alpha}(\tau\alpha)_n G_T - U_L(T - T_a)] \tag{9.4}$$

where $(\tau\alpha)_n = \eta_{oa}$ (Duffie and Beckman, 1991). Using the measured solar radiation and ambient temperature as input, simulations were carried out for the time interval 7:30 to 16:30 h except for the last day where the simulation had to be stopped at 16:25 h (due to early load application). The temperatures that were obtained at the end of the time intervals are:

Table 9.1. Hot Harry™ Simulated and Measured Storage Temperature

Date	Simulated	Measured
2 April 03	72.22°C	72.2°C
3 April 03	59.23°C	59.7°C
4 April 03	70.31°C	70.8°C
Average	**67.25°C**	**67.57°C**

The simulated results are slightly below the experimentally measured results, which suggest that the assumed simulation performance parameters may be conservative. The proposed performance parameters are in good agreement with the results suggested from PTL testing, with the exception the heat loss coefficient shows a stronger temperature dependence (note that the above expression for the heat loss coefficient suggests $U_L = 3.47$ W/m^2.K when $(T_w - T_a) = 30$ K).

After the stagnation resistance test has been completed, performance of the collector is re-evaluated to ensure there is not a significant (< 15%) drop in the collector overall efficiency. A plot of the post-stagnation efficiency points are shown with the pre-stagnation efficiency points and a curve given by equation 9.2 in Figure 9.3

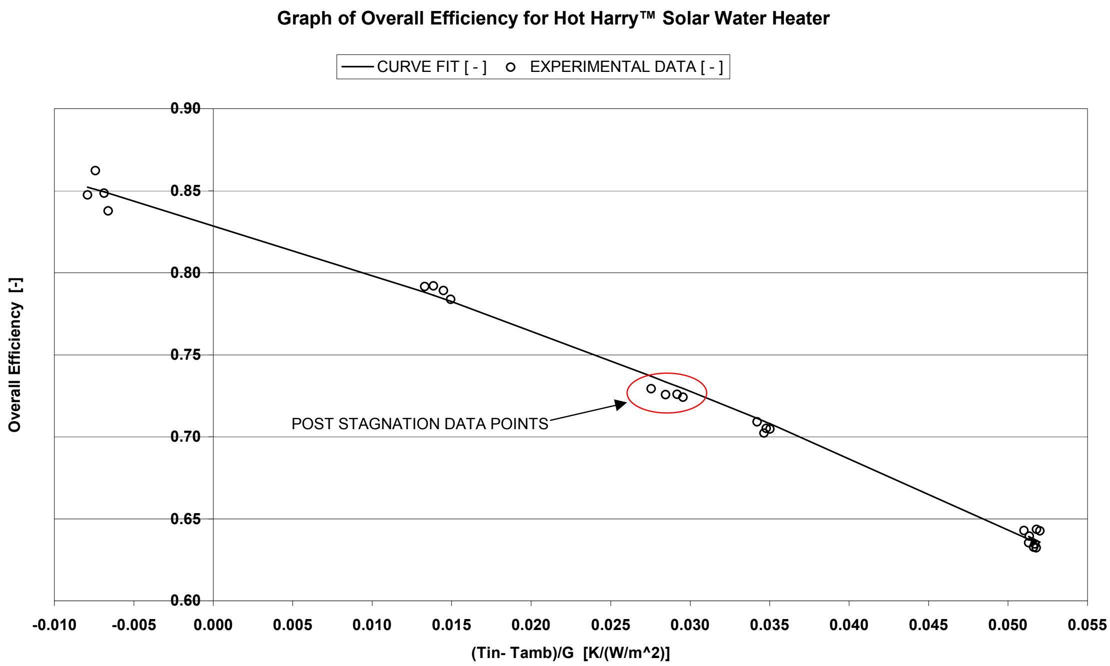

Figure 9.3 Plot of corrected Hot Harry™ collector overall efficiency

After performance, stagnation temperature resistance and post-stagnation performance testing, the collectors are type tested to prove structural integrity and function of the following:

- Glazing of collectors
- Hail resistance
- Protection against ingress of water

- Drain holes
- Air vent
- Structural strength

The Hot Harry™ collector was proven to meet the requirements of all of the tests above. The collector was not tested for "Protection against freezing" and is marked on the collector cover 'NOT SUITABLE FOR FROST AREAS'. Other markings as required by AS2717:2002 are also moulded into the top cover using permanent relief type text plates inside the mould.

The purpose of testing described is to determine performance parameters to be used in a TRNSYS numerical simulation for the calculation of solar contribution as per AS *4234:1994* Solar water heaters – Domestic and heat pump – Calculation of energy consumption. Professor Graham Morrison of the University of New South Wales performed the calculations that were then supplied to Standards Australia International Global for inclusion with the remainder of the product certification documents. Results of the performance calculation including energy contribution and annual energy savings for several heater configurations may be seen in Appendix N.

StandardsMark approval for the Hot Harry™ integral collector–storage solar water heater was granted to Gough Plastics by SAI Global on July 30, 2003. Copies of the StandardsMark Licence and StandardsMark Schedule may be seen in Appendix N.

9.3. Renewable Energy Certificates (RECs) assessment

Results of the TRNSYS simulation by Professor Morrison were also forwarded to the Office of the Renewable Energy Regulator with an application for the Hot Harry™ solar water heater to be included in the 'List of Eligible Solar Water Heaters'. The application was accepted by the Federal Minister for the Environment in January 2004. The Hot Harry™ Solar water heating system will be marketed in 7 configurations as shown in Table 9.2.

Table 9.2. Hot Harry model range (RECs shown for Zone 1 & 3)

Model	Load (RECs)	Description of Model Configuration
HH 1P E125	Medium (18)	A single Hot Harry™ Collector-Storage Panel with 125 litre Dux Model 125F2 Electric Storage Auxiliary Booster downstream
HH 1P E160	Medium (18)	A single Hot Harry™ Collector-Storage Panel with 160 litre Dux Model 160F2 Electric Storage Auxiliary Booster downstream
HH 1P G16	Medium (21)	A single Hot Harry™ Collector-Storage Panel in series with Bosch Model 16H Instantaneous Gas Auxiliary Booster downstream
HH 2P E125	Large (30)	Two Hot Harry™ Collector-Storage Panels in series with 125 litre Dux Model 125F2 Electric Storage Auxiliary Booster downstream
HH 2P E160	Large (30)	Two Hot Harry™ Collector-Storage Panels in series with 160 litre Dux Model 160F2 Electric Storage Auxiliary Booster downstream
HH 2P E250	Large (29)	Two Hot Harry™ Collector-Storage Panels in series with 250 litre Dux Model 250F2 Electric Storage Auxiliary Booster downstream
HH 2P G16	Large (32)	Two Hot Harry™ Collector-Storage Panels in series with Bosch Model 16H Instantaneous Gas Auxiliary Booster downstream

Purchasers of new Hot Harry™ systems may redeem their RECs allocation at market price. In October 2003, the spot price for RECs was \$38.75 / REC (Hanley, 2003). In addition to the RECs claim, Queensland purchasers will receive \$15 /REC from the Queensland Government Solar Hot Water System Rebate Scheme upon application approval. Other State Governments have similar rebates available for purchasers of new solar hot water systems.

A photograph of an early production 3 m^2 pre-heater system installed on a suburban rooftop may be seen in Figure 9.4.

Figure 9.4 2 panel pre-heater system on suburban rooftop.

Installation and Maintenance Instructions for the Hot Harry™ solar water heater may be seen in Appendix O.

10. CONCLUSION

This thesis has described the development of a novel rotationally moulded integral collector-storage solar water heater. The water heater has evolved from a small backyard experiment to a StandardsMark Approved product that is due for release to a local market in early 2004.

Particular aspects of the development focused on in this project included the transparent insulation and top cover system, the heat exchanger, thermal performance analysis and testing, structural design of the base unit, and aspects of the manufacturing process.

An investigation of available transparent insulation materials has been carried that has indicated an optimum top cover system to be specified for this heater design. The selected top cover insulation system is comprised of 50 mm high cellulose acetate honeycomb lying on 6 mm thick toughened glass and covered by a sheet of 3 mm thick, high impact, clear acrylic.

A medium high finned copper heat exchange tube with a rifled inner surface has been selected to allow efficient heat transfer from the stored collector fluid to the mains pressure potable water supply.

The background theory explaining advantages of a clear upper surface on the integral collector-storage chamber as opposed to an opaque upper surface have been presented. The uniform temperature profile developed within the collector-storage chamber has proven to increase overall performance of a tilted integral collector-storage device.

The process by which the heater will be manufactured has been defined. Design of the heater to be manufactured by rotational moulding has been discussed. Analysis of the long term structural integrity of a plastic water heater has been presented, and results of field testing have confirmed that a solar water heater can be successfully manufactured from plastic materials.

A novel rotationally moulded integral collector-storage solar water heater has been developed and certified to the requirements of AS/NZS 2712:2002 Solar and heat pump water heaters - Design and construction by Standards Australia International. The heater has been accepted by the Office of the Renewable Energy Regulator for inclusion in the List of Eligible Solar Water Heaters. Purchasers of a Hot Harry™ heater are eligible to apply for a rebate under the Queensland State Government Solar Hot Water Rebate Scheme and may also claim an allocation of Renewable Energy Certificates (RECs) against their purchase. Mathematical models have been developed that provide good agreement with physical testing. A simulation of the performance of a Hot Harry™ solar water heater in any specified location or configuration may be used to predict annual energy savings provided weather and load data are available.

Considering the potential to save electricity and the proportion of the purchase price that can be recovered by the purchaser immediately, the Hot Harry™ integral collector-storage solar water heater may be the beginning of a very efficient and successful family of domestic appliances.

11. BIBLIOGRAPHY

AEA Technologies (1999), *CFX V4.3 - Computational Fluid Dynamics Software*, Eldorado Hills, California, USA.

Australian and New Zealand Solar Energy Society Website, 2002
http://www.anzses.org/Gallery/Solah2.html

Australian Greenhouse Office Website, (2003)
http://www.greenhouse.gov.au/renewable/technologies/solar/lowtemp.html

Bejan, A. (1993), *Heat Transfer*, Wiley, New York, USA.

Butti, K. and Perlin, J. (1977), *Solar Water Heaters in California 1891 – 1930,* The CoEvolution Quarterly, 4-13, published by the Whole Earth Catalogue, Fall 1977.

Clark A.F. and Dickinson W.C., Chapter 12, Shallow solar ponds, pp. 377-402, *Solar Energy Technology Handbook*, Part A, Engineering Fundamentals, edited by W.C. Dickinson and P.N. Cheremisinoff, Marcel Dekker, New York, 1980.

Crawford, M. (1972), *Configuration factor between two unequal, parallel, coaxial squares*, Paper No. ASME 73-WA/HT-16.

Cullen & Co. (2001), *Preliminary Novelty Search for A Glazing Sealing Arrangement for a Solar Water Heater*, Confidential report produced by Cullen & Co., Patent and Trade Mark Attorneys, 239 George Street Brisbane.

Däldehög, D. (2002), *Heat transfer measurement with guarded hot plate apparatus*, Mechanical Engineering Thesis, School of Engineering, James Cook University, Townsville, Australia.

Duffie, J.A. and Beckman, W.A. (1991), *Solar Engineering of Thermal Processes.* John Wiley and Sons, New York, USA.

Efunda Website (2003). http://www.efunda.com/units/hardness/convert_hardness.cfm?HD=HRC&Cat=Steel#ConvInto

Ellis, M and Assocoiates (2001), Analysis of Potential for Minimum energy Performance Standards for Miscellaneous Water Heaters, Final Report, March 1st, 2001. http://www.energyrating.gov.au/library/pubs/tech-ewhmisc2001.pdf

Fairman, D., Hazan, H. and Laufer, I. (2001), *Reducing the Night Heat Loss from Solar Water Heater of the Integrated Collector-storage Type.* Solar Energy, Vol 71, No. 2, pp. 87–93.

Firth Cleveland Steel Strip (2001), *Hardness – Tensile Conversion Chart (Hardened Steel and Hard Alloys),* Technical Data Sheet, Firth Cleveland Steel Strip, Locarno Road, Tipton, England.

George Fischer (1996), *Plastics Technical Manual – A guide to the design and installation of plastics pipeline systems – First Edition*, Coventry, England.

Harris, J. A., (2000), *Personal communication*, School of Engineering, James Cook University, Townsville, Australia.

Hanley, M. (2003), *RECs on the Railroad*, Internet Magazine Article, http://www.cfoweb.com.au/stories/20031201/20962.asp.

Hollands, K. G. T. (1973), *Natural convection in thin-walled honeycomb panels*, Journal of Heat Transfer Vol 95, pp. 439-444.

Hollands, K.T.G. and Sibbitt, B.E. (1978), *Corrugated Cover Plate for a Flat Plate Collector,* U.S. Patent No. 4,078,544.

Hollands, K. G. T., Raithby, G. D., Russell, F.B. and Wilkinson, R.G. (1984), *Coupled Radiative and Conductive Heat Transfer Across Honeycomb Panels and Through Single Cells*. International Journal of Heat and Mass Transfer, Vol 27, pp. 2119-2131.

Incropera, F.P. and Dewitt, D.P. (1996), *Fundamentals of Heat and Mass Transfer,* Wiley, New York, USA.

Klein, S.A. and Alvarado, F.L. (1999), *Engineering Equation Solver (EES), V4.950,* FChart Software, Middleton, Wisconsin, USA.

Lin, S. H. and Sparrow, E. M. (1965), *Radiant Interchange Among Specularly Reflecting Surfaces, Application to Cylindrical and Conical Cavities.* Journal of Heat Transfer, Trans. ASME, Series C, Vol. 87, pp 299-307.

Lumsdaine, E, *Solar heating of a fluid through a semi-transparent plate: Theory and experiment,* Solar Energy, 12, pp. 457-467, 1969.

McBain, G. D. (1996), *Linear temperature variation in the sidewalls*, Personal communication, School of Engineering, James Cook University, Townsville, Australia.

NASA web site (2003), http://masterweb.jpl.nasa.gov/reference/paints.htm including Testors 1249 Flat Black spray enamel paint, Jet propulsion laboratory, California Institute of Technology.

Office of the Renewable Energy Regulator web site (2003), http://www.orer.gov.au/factsheets/recs-domestic-guideline.html.

Nugent, P. (2001), *Rotational Moulding – A Practical Guide.*

Perlmutter, M. and Siegel, R. (1963), *Effect of Specularly Reflecting Grey Surface on Thermal Radiation Through a Tube and From Its Heated Wall.* Journal of Heat Transfer, Trans. ASME, Series C, Vol. 85, pp 55-62.

Siegel, R. and Howell, J. R. (1972), *Thermal Radiation Heat Transfer*, 2nd ed, Hemisphere/McGraw Hill, New York.

Sodha, M.S., Nayak, J.K. and Kaushik, S.C., *Physics of shallow solar pond water heater,* Int. J. Energy Research, 4, pp. 323-337, 1980.

Standards Australia and Standards New Zealand (1999), *Australian/New Zealand Standard™ AS/NZS 2535.1:1999 Test methods for solar collectors – Thermal performance of glazed liquid heating collectors including pressure drop*, Jointly published by Standards Australia International, Sydney and Standards New Zealand, Wellington.

Standards Australia and Standards New Zealand (2002), *Australian/New Zealand Standard™ AS/NZS 2712:2002 Solar and heat pump water heaters - Design and construction*, Jointly published by Standards Australia International, Sydney and Standards New Zealand, Wellington.

Standards Australia (1996), *Australian Standard™ AS 2845.2:1996 Water supply backflow prevention devices – air gaps and break tanks*, Standards Australia International, Sydney.

Standards Australia (2003), *Australian Standard™ AS 3498:2003 Authorisation requirements for plumbing products – water heaters and hot water storage tanks*, Standards Australia International, Sydney.

Standards Australia (2003), *Australian Standard™ AS 4234:1994 Solar water heaters – Domestic and heat pump – Calculation of energy consumption*, Standards Australia International, Sydney.

Suehrcke, H. (2001), *Thermal performance simulation of a building using Engineering Equation Solver (EES)*, Northern Engineering Conference - Engineering Innovation and Sustainable Energy, 7-10 June, Cairns, Australia.

Suehrcke, H., Lowe, R. W. and Harris J. A. (2000), *Effect of Wall Emissivity on the Coupled Radiative and Conductive Heat Transfer Across Honeycomb Transparent Insulation.* Proc. 7th Australasian Heat and Mass Transfer Conference, 3-6 July, Townsville, Chalkface Press, Western Australia, pp. 301-307.

Suehrcke, H., (2000), *Personal communication*, School of Engineering, James Cook University, Townsville, Australia.

Suehrcke, H., Däldehög, D., Harris, J. A. and Lowe, R. W. (2001), *Heat Transfer across Transparent Zigzag Sheets*. Proc. ISES 2001 Solar World Congress, Adelaide, ANZSES, pp. 2057-2062.

Suehrcke, H., Däldehög, D., Harris, J. A. and Lowe, R. W. (2004), *Heat Transfer across Corrugated Sheets and Honeycomb Transparent Insulation*, Solar Energy, Volume 76, Numbers 1-3, pp. 351 – 358.

Suehrcke, H., Harris, J. A. and Lowe, R. W. (2003), An Integral Collector-Storage (ICS) Solar Water Heater with Transparent Upper Tank Surface, *Unpublished as yet.*

Tanishita, I. (1970), *Present Situation of Commercial Solar Water Heaters In Japan,* The Australian and New Zealand Section of the International Solar Energy Society, Melbourne, Australia.

Wieland Werke AG (2001), *Personal Communication with Technical Sales Representative*, Germany.

Wright, J.L. and Hollands, K.G.T. (1989), *Radiant and Free Convective Heat Transfer Through a Pleated (V-corrugated) Plastic Film,* Solar Energy, Volume 43, Number 6, pp. 379-384.

APPENDICES

APPENDIX A

Twin Parallel Flat Plates Program – Heat Transfer Theory

Engineering Equation Solver V4.950, program written to solve the theoretical solution for the heat transfer coefficient of a twin parallel flat plate cover system for a solar collector. Text in braces { }are comments in the program.

```
{Program to evaluate the resistance to heat transfer for an inclined, twin
parallel flat plate cover sytem.}

{Adapted from Duffie and Beckman, Chapter 6, 1991.}

{Written by Rod Lowe, 21-05-03}

{!Input variables}
Tsa = 100  { solar absorber temperature in degrees C}
T_sa = Tsa + 273.15 { solar absorber temperature in Kelvin}
Tamb = 10  {ambient temperature in Degrees C}
T_amb = Tamb + 273.15  {ambient temperature in Kelvin}
Tsky = Tamb - 0  {effective sky temperature in Degrees C}
T_sky = Tsky + 273.15  {effective sky temperature in Kelvin}
h_w = 10  {wind convective heat transfer coeffient in W/m2K}
epsilon_ac = 0.88 {emittance of cover plates}
epsilon_sa = 0.95 {emittance of  solar absorber}

{!Constants}
Patmos = 101.3  { atmospheric pressure in kPa}
g = 9.81  {gravitational constant in m/s^2}
sigma = 5.6700e-8  {Stefan-Boltzmann constant in W/m^2K^4}
L = 0.025  {distance between plates in m}
theta = 45  {tilt angle of collector in degrees}

{!Resistance to heat transfer from solar absorber to intermediate cover}
```

T_mean_sa_1 = (T_sa+T_c1)/2 { mean temperature between solar absorber and plate 1 in Kelvin}
Tmeansa1 = T_mean_sa_1 - 273.15 { mean temperature between solar absorber and plate 1 in Degrees C}

C_p_sa_1 = 1000*SPECHEAT(Air,T=T_mean_sa_1) {specific heat of air in J/kgK}
k_sa_1 = CONDUCTIVITY(Air,T=T_mean_sa_1) {thermal conductivity of air in W/mK}
mu_sa_1 = VISCOSITY(Air,T=T_mean_sa_1) {dynamic viscosity in Ns/m^2}
nu_sa_1 = mu_sa_1/rho_sa_1 {kinematic viscosity in m^2/s}
rho_sa_1 = DENSITY(Air,T=T_mean_sa_1,P=Patmos) {density in kg/m^3}

alpha_sa_1 = k_sa_1/(rho_sa_1 *C_p_sa_1) {thermal diffusivity in m^2/s}
beta_sa_1 = 1/T_mean_sa_1 {volumetric coefficient of expansion in 1/K}
Ra_sa_1 = g*beta_sa_1*(T_sa-T_c1)*L^3/(nu_sa_1*alpha_sa_1) {Rayleigh Number for air between absorber and 1}

Term_sa_1_a = 1-((1708*(sin(1.8*theta))^1.6)/(Ra_sa_1*cos(theta)))
Term_sa_1_b = 1-(1708/(Ra_sa_1*cos(theta))) {(if this term is negative, set to 0)}
Term_sa_1_c = (((Ra_sa_1*cos(theta))/5830))^(1/3)-1 {(if this term is negative, set to 0)}

Nusselt_sa_1 = 1+1.44*(Term_sa_1_a*Term_sa_1_b) + Term_sa_1_c {Nusselt number for air between absorber and 1}

h_c_sa_c1 = Nusselt_sa_1*k_sa_1/L {convective heat transfer coefficient between solar absorber and 1 in W/m^2K}

q_c_sa_c1 = h_c_sa_c1*(T_sa-T_c1) {convective heat flux from solar absorber to intermediate cover in W/m^2}

h_r_sa_c1 = sigma*(T_sa+T_c1)*(T_sa^2+T_c1^2)/(1/epsilon_sa + 1/epsilon_ac -1)
{radiative heat transfer coefficient between solar absorber and 1 in W/m^2K}

q_r_sa_c1 = h_r_sa_c1*(T_sa-T_c1) {radiative heat flux from solar absorber to intermediate cover in W/m^2}

{!Resistance to heat transfer from intermediate cover to outer cover}

T_mean_1_2 = (T_c1+T_c2)/2 { mean temperature between plates 1 & 2 in Kelvin}
Tmean12 = T_mean_1_2 - 273.15 { mean temperature between plates 1 & 2 in Degrees C}
Tc1 = T_c1 - 273.15 { intermediate plate temperature in Degrees C}
Tc2 = T_c2 - 273.15 { intermediate plate temperature in Degrees C}

C_p_1_2 = 1000*SPECHEAT(Air,T=T_mean_1_2) {specific heat of air in J/kgK}
k_1_2 = CONDUCTIVITY(Air,T=T_mean_1_2) {thermal conductivity of air in W/mK}
mu_1_2 = VISCOSITY(Air,T=T_mean_1_2) {dynamic viscosity in Ns/m^2}
nu_1_2 = mu_1_2/rho_1_2 {kinematic viscosity in m^2/s}
rho_1_2 = DENSITY(Air,T=T_mean_1_2,P=Patmos) {density in kg/m^3}

alpha_1_2 = k_1_2/(rho_1_2 *C_p_1_2) {thermal diffusivity in m^2/s}
beta_1_2 = 1/T_mean_1_2 {volumetric coefficient of expansion in 1/K}
Ra_c1_c2 = g*beta_1_2*(T_c1-T_c2)*L^3/(nu_1_2*alpha_1_2) {Rayleigh Number}

Term_1_2_a = 1-((1708*(sin(1.8*theta))^1.6)/(Ra_c1_c2*cos(theta)))
Term_1_2_b = 1-(1708/(Ra_c1_c2*cos(theta))) {(if this term is negative, set to 0)}

Term_1_2_c = (((Ra_c1_c2*cos(theta))/5830))^(1/3)-1 {(if this term is negative, set to 0)}

Nusselt_1_2 = 1+1.44*(Term_1_2_a*Term_1_2_b) + Term_1_2_c

h_c_c1_c2 = Nusselt_1_2*k_1_2/L {convective heat transfer coefficient between 1 and 2 in W/m^2K}

q_c_c1_c2 = h_c_c1_c2*(T_c1-T_c2) {convective heat flux from 1 to 2 in W/m^2}

h_r_c1_c2 = sigma*(T_c1+T_c2)*(T_c1^2+T_c2^2)/(1/epsilon_ac + 1/epsilon_ac -1)
{radiative heat transfer coefficient between 1 and 2 in W/m^2K}

q_r_c1_c2 = h_r_c1_c2*(T_c1-T_c2) {radiative heat flux from 1 to 2 in W/m^2}

{!Resistance to heat transfer from outer cover to surroundings}

q_c_c2_a = h_w*(T_c2-T_amb)   {convective heat flux between 2 and surroundings in W/m^2K}

h_r_c2_a = sigma*epsilon_ac*(((T_c2 + T_sky)*(T_c2^2 + T_sky^2))*(T_c2 - T_sky))/(T_c2 - T_amb)
{radiative heat transfer coefficient between 2 and surroundings in W/m^2K}

q_r_c2_a = h_r_c2_a*(T_c2 - T_amb) {radiative heat flux between 2 and surroundings in W/m^2K}

{!Overall top cover resistance to heat transfer for twin flat parallel plates - by energy conservation} q_loss = q_c_sa_c1 + q_r_sa_c1{total heat flux from solar absorber to intermediate cover in W/m^2}

q_loss = q_c_c1_c2 + q_r_c1_c2 {total heat flux from intermediate cover to outer cover in W/m^2}

q_loss = q_c_c2_a + q_r_c2_a {total heat flux from outer cover to surroundings in W/m^2}

U_t_tp = q_loss/(T_sa - T_amb) {top cover system heat transfer coefficient in W/m^2.K}

The results of the exact solution are given below:

alpha_1_2=0.00002547 [m^2/s]	L=0.025 [m]
alpha_sa_1=0.00003042 [m^2/s]	mu_1_2=0.00001968 [Ns/m^2]
beta_1_2=0.003079 [1/K]	mu_sa_1=0.00002117 [Ns/m^2]
beta_sa_1=0.002791 [1/K]	Nusselt_1_2=2.929 [-]
C_p_1_2=1007 [J/kg.K]	Nusselt_sa_1=2.439 [-]
C_p_sa_1=1008 [J/kg.K]	nu_1_2=0.00001811 [m^2/s]
epsilon_ac=0.88 [-]	nu_sa_1=0.00002149 [m^2/s]
epsilon_sa=0.95 [-]	Patmos=101.3 [kPa]
g=9.81 [W/m^2. K]	q_c_c1_c2=121.3 [W/m^2]
h_c_c1_c2=3.265 [W/m^2. K]	q_c_c2_a=230.9 [W/m^2]
h_c_sa_c1=2.948 [W/m^2. K]	q_c_sa_c1=87.68 [W/m^2]
h_r_c1_c2=6.127 [W/m^2. K]	q_loss=349.1 [W/m^2]
h_r_c2_a=5.116 [W/m^2. K]	q_r_c1_c2=227.7 [W/m^2]
h_r_sa_c1=8.788 [W/m^2. K]	q_r_c2_a=118.1 [W/m^2]
h_w=10 [W/m^2. K]	q_r_sa_c1=261.4 [W/m^2]
k_1_2=0.02786 [W/m. K]	Ra_c1_c2=38021 [-]
k_sa_1=0.03021 [W/m. K]	Ra_sa_1=19463 [-]

rho_1_2=1.087 [kg/m^3]

rho_sa_1=0.9851 [kg/m^3]

sigma=5.6700E-08 [W/m^2. K^4]

Tamb=10 [Deg C]

Tc1=70.26 [Deg C]

Tc2=33.09 [Deg C]

Term_1_2_a=0.9377 [-]

Term_1_2_b=0.9365 [-]

Term_1_2_c=0.6645 [-]

Term_sa_1_a=0.8783 [-]

Term_sa_1_b=0.8759 [-]

Term_sa_1_c=0.3315 [-]

theta=45 [degrees]

Tmean12=51.67 [Deg C]

Tmeansa1=85.13 [Deg C]

Tsa=100 [Deg C]

Tsky=10 [Deg C]

T_amb=283.2 [K]

T_c1=343.4 [K]

T_c2=306.2 [K]

T_mean_1_2=324.8 [K]

T_mean_sa_1=358.3 [K]

T_sa=373.2 [K]

T_sky=283.2 [K]

U_t_tp=3.878 [W/m^2. K]

APPENDIX B

Twin Parallel Flat Plates Computer Program – Klein Empirical Equation

Engineering Equation Solver V4.950, program written to solve the empirical solution (Klein, 1979) for the heat transfer coefficient of a twin parallel flat plate cover system for a solar collector. Text in braces { }are comments in the program.

```
Program to evaluate the resistance to heat transfer for an inclined, twin
parallel flat plate cover sytem.}


{Adapted from Duffie and Beckman, Chapter 6, 1991. After Klein, 1979}
{Written by Rod Lowe, 26-05-03}

{!Input variables}
Tsa = 100  { solar absorber temperature in degrees C}
T_sa = Tsa + 273.15 { solar absorber temperature in Kelvin}
Tamb = 10  {ambient temperature in Degrees C}
T_amb = Tamb + 273.15  {ambient temperature in Kelvin}
h_w = 10  {wind convective heat transfer coeffient in W/m^2K}
epsilon_ac = 0.88 {emittance of cover plates}
epsilon_sa = 0.06 {emittance of  solar absorber}
N = 2  {Number of covers in cover system}

{!Constants}
Patmos = 101.3  { atmospheric pressure in kPa}
g = 9.81  {gravitational constant in m/s^2}
sigma = 5.6700e-8  {Stefan-Boltzmann constant in W/m^2K^4}
L = 0.025  {distance between plates in m}
theta = 45  {tilt angle of collector in degrees}



{!Heat transfer coefficient calculations}


C = 520*(1-0.000051*theta^2)
```

```
f = (1+0.089*h_w - 0.1166*h_w*epsilon_sa)*(1+0.07866*N)
e = 0.430*(1-100/T_sa)

Term1 = (C/T_sa)*((T_sa-T_amb)/(N+f))^e {top cover system heat transfer coefficient in W/m^2.K}
Term2 = sigma*(T_sa+T_amb)*(T_sa^2+T_amb^2)
Term3 = 1/(epsilon_sa+0.00591*N*h_w)
Term4 = (2*N+f-1+0.133*epsilon_sa)/epsilon_ac

U_t_tp = 1/(N/Term1 + 1/h_w)+Term2/(Term3+Term4-N)
```

The results of the empirical solution are given below:

C=466.3

e=0.3148

epsilon_ac=0.88 [-]

epsilon_sa=0.06 [-]

f=2.106

g=9.81 [W/m^2. K]

h_w=10 [W/m^2. K]

L=0.025 [m]

N=2

Patmos=101.3 [kPa]

sigma=5.6700E-08 [W/m^2. K^4]

Tamb=10 [Deg C]

Term1=3.302

Term2=8.165

Term3=5.612

Term4=5.812

theta=45 [degrees]

Tsa=100 [Deg C]

T_amb=283.2 [K]

T_sa=373.2 [K]

U_t_tp=2.284 [W/m^2. K]

APPENDIX C

Honeycomb Heat Transfer Computer Program

Engineering Equation Solver V4.950, program written to evaluate the heat transfer coefficient of honeycomb transparent insulation cover system for a solar collector. Text in braces { }are comments in the program.

```
"Program to calculate the coupled radiative-conductive heat transfer in a
honeycomb".
"Ref: Hollands et al., 'Coupled radiative and conductive heat transfer across honeycomb
panels and through single cells', Int. J. Heat & Mass Transfer, Vol. 27, No 11, pp. 2119-
2131, 1984".
"Note the position coordinate z is defined with respect to the hot plate.
By: H. Suehrcke, March 2000"

{Differential Viewfactor functions for a cylindical cavity}

Function dFww`dz`(z, z`, L, R) {View factor per unit target ring element
length between two cylinders}

{ring differential elements for one unit source ring area}
{Source: R. Siegel & J.R. Howell, Thermal Radiation Transfer, 2nd ed.,
Appendix C, McGraw-Hill, 1981.}
{z  = source ring element mid position}
{z` = target ring element mid position}

 x := abs(z`-z)/(2*R);
 dFww`dz` := (1 - (x^3 + 1.5*x)/((x^2 +1)^1.5))/(2*R);
End

Function dFSww`dz`(z, z`, L, R, ew, Kdelta) {View factor rate dFww`dz`
including specular wall}
```

```
{reflections.  Source: R. Siegel & J.R. Howell, Thermal Radiation Transfer,
2nd ed., pp. 313-315,}
{McGraw-Hill, 1981.  Note error in above cited derivation - dx should be
dx/D}
rhos := (1-ew); {honeycomb wall reflectance}
 dFSww`dz` := dFww`dz`(z, z`, L, R) {+ (1-
Kdelta)*sum(rhos^n/(n+1)*dFww`dz`(z/(n+1), z`/(n+1), L, R), n=1,40)};
End                         {n = number of wall reflections}

Function Fwh(z, L, R) {View factor between a differential area cylinder ring
element and the hot plate}
                            {on a per unit ring element area basis}
 x := z/(2*R); {z  = ring element mid position}
 Fwh := (x^2 + 0.5)/((x^2 +1)^0.5) - x;
End

Function FSwh(z, L, R, ew, Kdelta) {View factor Fwh including specular wall
reflections.  Source:}
{M. Perlmutter & R. Siegel, The effect of sepcularly reflecting gray surface
on thermal radiaton}
{through a tube and from its heated wall, Journal of Heat Transfer, Vol. 85,
pp. 55-62,1963.}
 rhos := (1-ew); {honeycomb wall reflectance}
 FSwh := Fwh(z, L, R) {+ (1-Kdelta)*sum(rhos^n*(Fwh(z/(n+1), L, R) -
Fwh(z/n, L, R)), n=1,40)};
End

{Interated view factors between area elements of finite size in a cylindical
cavity}

Function AveFwh(R,L,deltaz, ew, Kdelta, i) {Calculate the (average) view
factor between a ring}
 zlow  := (i-1.0)*deltaz; {element of finite size located between zlow and
zhigh and the hot plate}
```

```
 zhigh := i*deltaz; {on a per unit area ring element basis}
 dz := (zhigh-zlow)/20;
 AveFwh := sum(FSwh(zlow+j*dz+dz/2, L, R, ew, Kdelta)/20, j = 0, 19);
End

Function TrapezFww`(R,L,deltaz,z,j, ew, Kdelta) {Calculate the view factor
between a source ring}
 z`low  := (j-1.0)*deltaz; {differential element and a ring element of finite size
located at z`low }
 z`high := j*deltaz; {between z`high on a per unit source area basis using
trapezoidal approximation}
 dz` := (z`high-z`low)/20;
 TrapezFww` := sum(dz`*(dFSww`dz`(z, z`low+k*dz`, L, R, ew,
Kdelta)+dFSww`dz`(z, z`low+k*dz`+dz`, L, R, ew, Kdelta))/2, k = 0, 19);
End

Function AveFww`(R,L,deltaz,i,j, ew, Kdelta) {Calculate the (average) view
factor between a  two}
 zlow  := (i-1.0)*deltaz; {ring elements of finite size with the source element
located at zlow}
 zhigh := i*deltaz; {between zhigh and the target element located between
z`low and z`high}
 dz := (zhigh-zlow)/20;
 AveFww` := sum(TrapezFww`(R,L,deltaz,zlow+m*dz+dz/2,j, ew, Kdelta)/20,
m = 0,19)
End

Function Few(Kdelta, ew) {Function to set wall emissivity factor according to
specular or diffuse reflection}
 Few := ew;
 If (Kdelta > 0) Then Few := 1;
End

{Set constants and boundary conditions}
```

```
sigma = 5.67e-8 {Stefan-Boltzmann constant in W/m^2.K^4}
N = 32 {Number of interior nodes}
ew = 0.65; eh = 0.92; ec = 0.92 {Emittances of wall, hot and cold plate}
L = 0.030; R = 0.00508; t = 0.025e-3 {Honeycomb length, radius and demi-
wall thickness in m}
deltaz = L/N {Height of control volume element}
Tc = 273.15 + 26.4 {Cold plate temperature in K}
Th = 273.15 + 51.1 {Hot plate temperature in K}
Tave = (Tc +Th)/2 {Average temperature in K}
kair = Conductivity(Air,T=Tave)
ke = 0.03018 {Area weighted average thermal conductivity in W/m.K}
Lair = 0.006 {Air gap in m}
Kdelta = 1 {0 specular wall reflection, 1 diffuse wall reflection}

{Define gid points}

Duplicate i = 1,N
 z[i] = (i-0.5)*deltaz
End

{Calculate view factors}

Duplicate i = 1,N
 Fhw[i] = Fwh[i]*(2*deltaz/R) {Calculate view factor from receprocity}
 Fcw[i] = Fwc[i]*(2*deltaz/R)  {Calculate view factor from receprocity}
 Fwh[i] = AveFwh(R,L,deltaz, ew, Kdelta, i)
 Fwc[i] = Fwh[N-i+1] {Use symmetrie with Fwh to determine Fwc}
 Duplicate j = 1,N
  Fww`[i,j] = AveFww`(R,L,deltaz,i,j, ew, Kdelta)
 End
End
Fhc = 1 - sum(Few(Kdelta, ew)*Fhw[i],i=1,N) {Use view factor summation to
determine Fhc}
```

```
{Solve equations to find the unknown J's and Tw's}
{The equation numbers refer to the above cited reference by Hollands et al.,
1984}

{1. Surface radiosities}

Jh = eh*sigma*Th^4 + (1-eh)*(Jc*Fhc + integralh) {eqn (2)}
integralh = sum(Jw[i]*Fhw[i], i = 1, N)

Jc = ec*sigma*Tc^4 + (1-ec)*(Jh*Fhc + integralc) {eqn (3)}
integralc = sum(Jw[i]*Fcw[i], i = 1, N)

Duplicate i = 1, N
 Jw[i] = ew*sigma*Tw[i]^4  + Kdelta*(1-ew)*(Jh*Fwh[i] + Jc*Fwc[i] +
integralw[i]) {eqn (1)}
 integralw[i] = sum(Jw[j]*Fww`[i,j], j = 1, N)
End

{2. Energy Balance equations}

{Interior elements}

Duplicate i = 2, N-1
 ke*(R+t)^2/(2*R)*(Tw[i+1] - 2*Tw[i] + Tw[i-1])/deltaz^2 = ew*(sigma*Tw[i]^4
- Jh*Fwh[i] - Jc*Fwc[i] - integralw[i]) {eqn (17)}
End

{Boundary elements}

(R+t)^2/(2*R)*((Tw[2] - Tw[1])/(deltaz/ke) - (Tw[1] -
Th)/(deltaz/(2*ke)))/deltaz = ew*(sigma*Tw[1]^4 - Jh*Fwh[1] - Jc*Fwc[1] -
integralw[1]) {eqn (17)}
```

```
(R+t)^2/(2*R)*((Tc - Tw[N])/(Lair/kair + deltaz/(2*ke)) - (Tw[N] - Tw[N-1])/(deltaz/ke))/deltaz = ew*(sigma*Tw[N]^4 - Jh*Fwh[N] - Jc*Fwc[N] - integralw[N]) {eqn (17)}

{Calculate the heat transfer coefficient between the hot and cold plate}

hhot = (qhc + qhr)/(Th-Tc) {eqn (10)} {at hot plate}
qhc = ke*(Th - Tw[1])/(deltaz/2)
qhr = eh*(sigma*Th^4 - Jc*Fhc - integralh) {eqn (12)}

hcold = (qcc + qcr)/(Th-Tc) {eqn (10)} {at cold plate}
qcc = (Tw[N] - Tc)/(Lair/kair + deltaz/(2*ke)) {eqn (11)}
qcr = -ec*(sigma*Tc^4 - Jh*Fhc - integralc) {eqn (12)}

{Check that view factors sum to 1.0}

Sh = sum(Few(Kdelta, ew)*Fhw[i], i = 1, N)+ Fhc
Sc = sum(Few(Kdelta, ew)*Fcw[i], i = 1, N)+ Fhc
Duplicate i = 1, N
  Sw[i] = sum(Few(Kdelta, ew)*Fww`[i,j], j = 1, N)+ Fwh[i] + Fwc[i]
End
```

The results of the numerical solution are given below:

deltaz=0.0009375	Jc=460.7
ec=0.92	Jh=623.8
eh=0.92	kair=0.02694
ew=0.65	Kdelta=1
Fhc=0.02714	ke=0.03018
hcold=2.731	L=0.03
hhot=2.726	Lair=0.006
integralc=491.9	N=32
integralh=576.9	qcc=19.31

qcr=48.14
qhc=32.95
qhr=34.4
R=0.00508
Sc=1
Sh=1
sigma=5.6700E-08
t=0.000025
Tave=311.9 [K]
Tc=299.6 [K]
Th=324.3 [K]
Local variables in FUNCTION
dFww`dz`
z=2.998E-02
z`=3.000E-02
L=3.000E-02
R=5.080E-03
x=2.307E-03
Local variables in FUNCTION
dFSww`dz`
z=2.998E-02
z`=3.000E-02
L=3.000E-02
R=5.080E-03
ew=6.500E-01
Kdelta=1.000E+00
rhos=3.500E-01
Local variables in FUNCTION Fwh
z=2.998E-02
L=3.000E-02
R=5.080E-03
x=2.950E+00
Local variables in FUNCTION FSwh
z=2.998E-02
L=3.000E-02
R=5.080E-03
ew=6.500E-01
Kdelta=1.000E+00
rhos=3.500E-01
Local variables in FUNCTION AveFwh
R=5.080E-03
L=3.000E-02
deltaz=9.375E-04
ew=6.500E-01
Kdelta=1.000E+00
i=3.200E+01
zlow=2.906E-02
zhigh=3.000E-02
dz=4.688E-05
Local variables in FUNCTION
TrapezFww`
R=5.080E-03
L=3.000E-02
deltaz=9.375E-04
z=2.998E-02
j=3.200E+01
ew=6.500E-01
Kdelta=1.000E+00
z`low=2.906E-02
z`high=3.000E-02
dz`=4.688E-05
Local variables in FUNCTION
AveFww`
R=5.080E-03
L=3.000E-02
deltaz=9.375E-04
i=3.200E+01
j=3.200E+01

ew=6.500E-01

Kdelta=1.000E+00

zlow=2.906E-02

zhigh=3.000E-02

dz=4.688E-05

Local variables in FUNCTION Few

Kdelta=1.000E+00

ew=6.500E-01

APPENDIX D

Heat Exchanger Efficiency Program

Engineering Equation Solver V4.950, program written to evaluate the heat transfer efficiency of a finned heat exchanger tube. Text in braces { }are comments in the program.

```
{ Finned tube heat exchanger calculations }
{ Originally written by Jonathan Harris, 7-11-97 }
{ Reference: Incropera & DeWitt, "Fundamentals of Heat and Mass Transfer }
{Adapted by Rodney Lowe, 21-06-99 }
{ ** This version for GEWA-DW 11 fpi D-1145.14110-15 tube. ** }

{ Notes: The fin efficiency has to be manually entered if the geometry is changed }
{Enter a guess value ( say 65% ), solve, and use param1 and param2 to find eta_f
from Fig 3.19 }

{ Input parameters }
{ T_c_o = 60 }  { Cold side outlet temperature, [ Deg C ] }
T_c_i = 20  { Cold side inlet temperature, [ Deg C ] }
Q_c = 0.1333e-3   { Cold side volumetric flow rate, [ m^3/s ] }
T_0 = 80   { Initial hot side temperature in storage tank, [ Deg C ] }
P_amb = 101.3  { Ambient air pressure,  [ kPa ] }
g = 9.81  { Gravitational acceleration,  [ m/s^2 ] }

{ Heat exchanger geometry }
D_i = 12.0e-3  { Heat exchanger internal diameter,  [ m ] }
D_p = D_i + 2.0e-3  { Heat exchanger pipe external diameter,  [ m ] }
D_f = D_i + 11.0e-3  { Heat exchanger fin diameter,  [ m ] }
t = 0.45e-3  { Heat exchanger fin thickness,  [ m ] }
k_x = 310  { Heat exchanger thermal conductivity,  [ W/mK ] }
L_f = 4.5e-3  { fin length from base of pipe,  [ m ] }
p_f = 2.3e-3  { fin pitch,  [ m ] }
L  = 7.5  { Heat exchanger tube length,  [ m ] }
A_c = pi*D_i^2/4  { Heat exchanger internal cross sectional area,  [m^2]}
```

```
{ Calculated HX properties }
r_2_c = D_f/2 + t/2  { Refer to Fig 3.19 in Incropera & DeWitt,  [ m ] }
r_1 = D_p/2  { Refer to Fig 3.19 in Incropera & DeWitt,  [ m ] }
N = L/p_f  { Total number of fins,  [ - ] }
A_f = N*2*pi*(r_2_c^2 - r_1^2)  { Total fin area,  [ m^2 ] }
A_t = A_f + (L-N*t)*2*pi*r_1  { Total fin area + base area,  [ m^2 ] }
eta_f = 0.92  { Individual fin efficiency,  [ - ], read off Fig 3.19 }
eta_0 = 1 - A_f/A_t*(1-eta_f)  { Overall fin efficiency,  [ - ] }
param1 = r_2_c/r_1  { Refer to Fig 3.19 in Incropera & DeWitt,  [ - ] }
L_c = L_f + t/2  { Refer to Fig 3.19 in Incropera & DeWitt,  [ m ] }
A_p = L_c*t  { Refer to Fig 3.19 in Incropera & DeWitt,  [ m^2 ] }
param_2 = L_c^(1.5)*sqrt(h_0/(k_x*A_p))  { Refer to Fig 3.19 in Incropera & DeWitt,  [ - ] }

{ Overall heat transfer rate }
q = DELTA_T_lm/R_t
q = m_dot*Cp_c*(T_c_o - T_c_i)

{ Log mean temperature difference }
DELTA_T_1 = T_inf - T_c_i
DELTA_T_2 = T_inf - T_c_o
DELTA_T_lm = (DELTA_T_2-DELTA_T_1)/ln(DELTA_T_2/DELTA_T_1)

{ Cold side properties ( evaluated at mean cold side temperature ) }
T_c_m = ( T_c_i + T_c_o )/2
rho_c = DENSITY(Water,T=T_c_m,P=P_amb)
k_c = CONDUCTIVITY(Water,T=T_c_m,P=P_amb)
Cp_c = 1000*SPECHEAT(Water,T=T_c_m,P=P_amb)
mu_c = VISCOSITY(Water,T=T_c_m,P=P_amb)
nu_c = mu_c/rho_c
m_dot = rho_c*Q_c
Re_c = 4*Q_c/(pi*nu_c*D_i)
Pr_c = (rho_c*Cp_c*nu_c)/k_c
```

```
{ Heat transfer coefficient on inside of HX tube }
f_h_c = 1+Vel
h_c = f_h_c*k_c*NuD/D_i  { ** enhanced heat transfer coeff - f_h_c }
NuD = 0.023*Re_c^(0.8)*Pr_c^(0.333)  { Nusselt number inside tube,  [ - ] }

{ Hot side properties ( evaluated at T_b ) }
T_b = T_c_m + q*( R_c + R_w)
rho_h = DENSITY(Water,T=T_b,P=P_amb)
k_h = CONDUCTIVITY(Water,T=T_b,P=P_amb)
Cp_h = 1000*SPECHEAT(Water,T=T_b,P=P_amb)
mu_h = VISCOSITY(Water,T=T_b,P=P_amb)
nu_h = mu_h/rho_h
alpha_h = k_h/(rho_h*Cp_h)

{ Heat transfer coefficient on outside of HX tube, free convection }
beta = 400.4e-6  { Thermal expansion coefficient for 315K,  [ 1/K ] }
D_eff = ( D_p + D_f )/2  { effective diameter,  [ m ] }
Ra_D = g*beta*(T_inf - T_b)*D_eff^3/(nu_h*alpha_h)  { Rayleigh number,  [ - ] }
Nu0 = 0.480*Ra_D^(0.250)  { **Nusselt No., Valid for 10^7<Ra_D<10^12,  [ - ] }
h_0 = k_h*Nu0/D_eff  { Hot side heat transfer coefficient,  [ W/m^2K ] }

{ Radial thermal resistance components }
R_c = 1/(pi*D_i*L*h_c)  { Cold side resistance,  [ K/W ] }
R_w = ln(D_p/D_i)/(2*pi*k_x*L)  { Heat exchanger wall resistance,  [ K/W ] }
R_h = 1/(eta_0*h_0*A_t)  { Hot side resistance,  [ K/W ] }
R_t = R_c + R_w + R_h  { Total radial thermal resistance,  [ K/W ] }

{ Global energy balance }
mass= 163.7  { thermal mass of collector,  [ kg ] }
Vol = mass/rho_h { Storage tank volume, [ m^3 ] }
E_0 = rho_h*Vol*Cp_h*T_0  { Initial energy contained in tank,  [ J ] }
E_st = rho_h*vol*Cp_h*T_inf  { Energy contained in tank at any time,  [ J ] }
```

DELTA_E_st = -rho_c*Q_c*Cp_c*(T_c_o - T_c_i) { Energy balance equation, [J/s] }

E_st = E_0 + integral(DELTA_E_st,Time) { Energy contained in tank at any time, [J] }

E_pipe = (7.5/Vel*m_dot)*Cp_h*(T_0 - T_c_i) { Add in slug of hot water in pipe at t=0, [J] }

E_useful = E_0 - E_st + E_pipe { Energy withdrawn from collector, [J] }
eta_HX = (T_c_o - T_c_i)/(T_inf - T_c_i)*100 { heat exchanger efficiency, [%] }

{ Pressure loss calculations }
f = 0.075 { Friction factor from Moody diagram, [-] }
k_90 = 0.9 { Head loss factor for 90 degree bend, [-] }
k_180 = 2 { Head loss factor for 180 degree bend, [-] }
k_f = 0.5 { Head loss factor for entry and exit fittings, [-] }
k_sum = 2*k_90 + 4*k_180 + 2*k_f { Total sum of head loss factors, [-] }
FL = f*L/D_i { Collected for comparison with k_sum, [-] }
Vel = Q_c/(pi*D_i^2/4) { Flow velocity in tube, [m/s] }
H_l = (FL + k_sum)*Vel^2/(2*g) { Head loss, [m] }
DELTA_P = H_l*rho_c*g/1000 { Pressure loss in tube, [kPa] }
DELTA_T = DELTA_T_1 {mean collector to inlet temperature difference, [Deg C] }
eta_c = (0.561*DELTA_T^0.11)*100 { heat exchanger efficiency approximation, [%] }

The results of the empirical solution are given below:

alpha_h=1.5735E-07 [m^2/s]
A_c=0.0001131 [m^2]
A_f=1.813 [m^2]
A_p=0.000002126 [m^2]
A_t=2.078 [m^2]
beta=0.0004004 [1/K]

Cp_c=4175 [J/kg.K]

Cp_h=4178 [J/kg.K]

DELTA_E_st=-28850 [J]

DELTA_P=39.65 [Pa]

DELTA_T=59.58 [K]

DELTA_T_1=59.58 [K]

DELTA_T_2=7.21 [K]

DELTA_T_lm=24.79 [K]

D_eff=0.0185 [m]

D_f=0.023 [m]

D_i=0.012 [m]

D_p=0.014 [m]

eta_0=0.9302 [-]

eta_c=87.95 [%]

eta_f=0.92 [-]

eta_HX=87.9 [%]

E_0=5.4720E+07 [J]

E_pipe=210481 [J]

E_st=5.4431E+07 [J]

E_useful=500108 [J]

f=0.075 [-]

FL=46.88 [-]

f_h_c=2.179 [-]

g=9.81 [m/s^2]

h_0=887.6 [W/m^2. K]

h_c=13293 [W/m^2 .K]

H_l=4.084 [W/m^2 .K]

k_180=2 [-]

k_90=0.9 [-]

k_c=0.6389 [W/m.K]

k_f=0.5 [W/m.K]

k_h=0.6483 [W/m.K]

k_sum=10.8 [-]

k_x=310 [W/m.K]

L=7.5 [m]

L_c=0.004725 [m]

L_f=0.0045 [m]

mass=163.7 [kg]

mu_c=0.000584 [N.s/m^2]

mu_h=0.000511 [N.s/m^2]

m_dot=0.1319 [kg/s]

N=3261 [-]

Nu0=25.33 [-]

NuD=114.6 [-]

nu_c=5.9006E-07 [-]

nu_h=5.1814E-07 [-]

param1=1.675 [-]

param_2=0.3769 [-]

Pr_c=3.817 [-]

P_amb=101.3 [kPa]

p_f=0.0023 [m]

q=28850 [W]

Q_c=0.0001333 [m^3/s]

Ra_D=7.7518E+06 [-]

Re_c=23970 [-]

rho_c=989.8 [kg/m^3]

rho_h=986.1 [kg/m^3]

r_1=0.007 [m]

r_2_c=0.01173 [m]

R_c=0.0002661 [K/W]

R_h=0.0005828 [K/W]

R_t=0.0008594 [K/W]

R_w=0.00001055 [K/W]

t=0.00045 [m]

Time=10 [s]

T_0=80 [Deg C]

T_b=54.16 [Deg C]

T_c_i=20 [Deg C]

T_c_m=46.18 [Deg C]

T_c_o=72.37 [Deg C]

T_inf=79.58 [Deg C]

Vel=1.179 [m/s]

Vol=0.166 [m^3]

APPENDIX E

Functional Specification for Spring Clip

1. SCOPE

The purpose of this document is to outline as completely as possible the performance requirements of a spring clip to be manufactured for Gough Plastics.

2. APPLICATION

The purpose of the spring clip is to apply a clamping force which will maintain a watertight seal between a sheet of 6 millimetre glass and a hollow walled polypropylene product. The gasket is a rubber o-ring. The spring clips will be installed 50 millimetres apart to provide an average load of approximately 3000 Newtons/metre on the gasket. See attached Autocad solid model for further conceptual description of the spring clip application.

3. SIZE

The cross section of the spring clip should be able to be contained within an envelope of 40mm high x 40mm wide. The spring clip will be 50mm long.

4. PHYSICAL CHARACTERISTICS

The spring clip should apply a clamping force of 330 $\pm$ 30 Newtons when opened to a dimension of 14 millimetres at the bite. A change in the bite dimension of $\pm$ 2 millimetres should result in a change of the clamping force no greater than 60 Newtons from the original clamping force at 14 millimetres separation. The spring clip must be able to be opened to a bite dimension of at least 18.5 millimetres without any plastic deformation occurring.

5. INSTALLATION

Provision must be made for pliers or some such tool to open the spring clip and release it into position on the product. The lower portion of the spring clip and installation tool must be able to be inserted into a 54 millimetre x 8 millimetre slot machined into the plastic product. Once fitted, the spring clip will remain in place for the duration of the life of the product.

6. LOCATION

Provision must be made for retaining the spring clip on the plastic product. It is desirable not to use mechanical fasteners to retain the spring clip. The retaining device should be incorporated into the spring clip such that is formed from the same piece of material as the spring clip.

7. ENVIRONMENTAL CONDITIONS

The spring clip must be able to withstand temperature fluctuations from 50 degrees Celsius to 80 degrees Celsius on a daily basis. The spring clip will be in contact with polypropylene, glass and foamed polyurethane materials. It is expected that the spring clip will be able to operate under these conditions, without significant loss of clamping force for a minimum period of ten years. A protective coating should be allowed for in the spring clip dimensions.

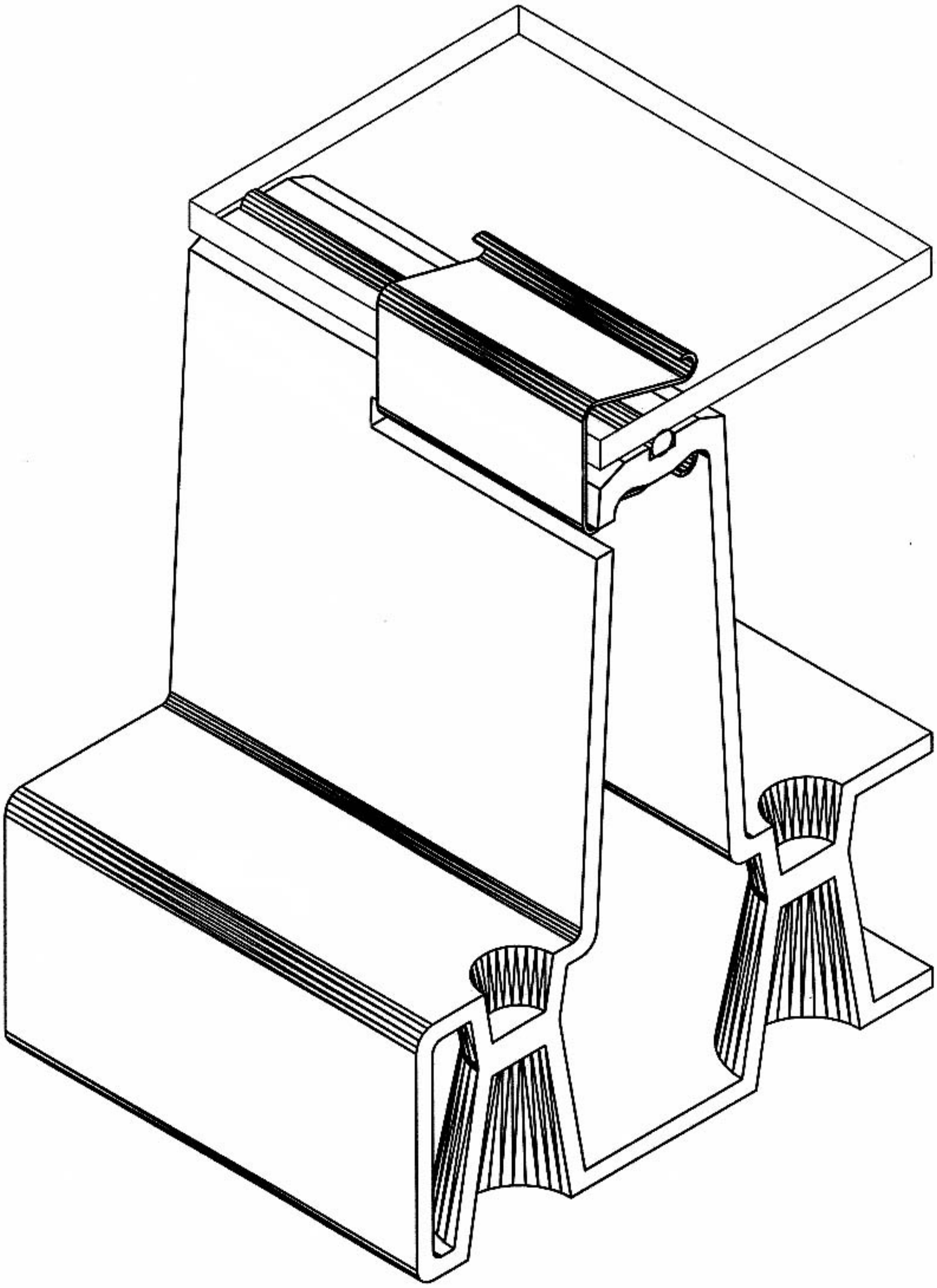

Conceptual AutoCad model of spring clip, glazing, o-ring and base component

APPENDIX F: Calculation of Reaction Forces on Inner Glazing

Analysis of Pressure Distribution in Hot Harry Solar Water Heater

Free body diagram of glass exposed to water pressure at 30 degrees tilt

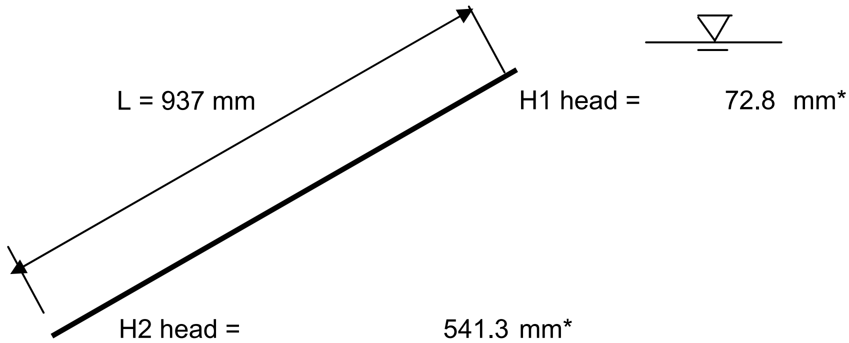

* Dimensions taken from AutoCad model of collector with water at overflow level

P =	H *	g	* rho		
P1 =	0.0728	9.81	1000 =	714	N/m^2
P2 =	0.5413	9.81	1000 =	5310	N/m^2

Assumptions

1) Density of water is 1000 kg/m^3

2) use simply supported case to simplify analysis of reactions

3) Analyse centre glass section unit width (1 metre wide)

4) Reaction forces uniform across unit width

Use the principle of superposition to analyse the uniform and triagular distributed loads seperately

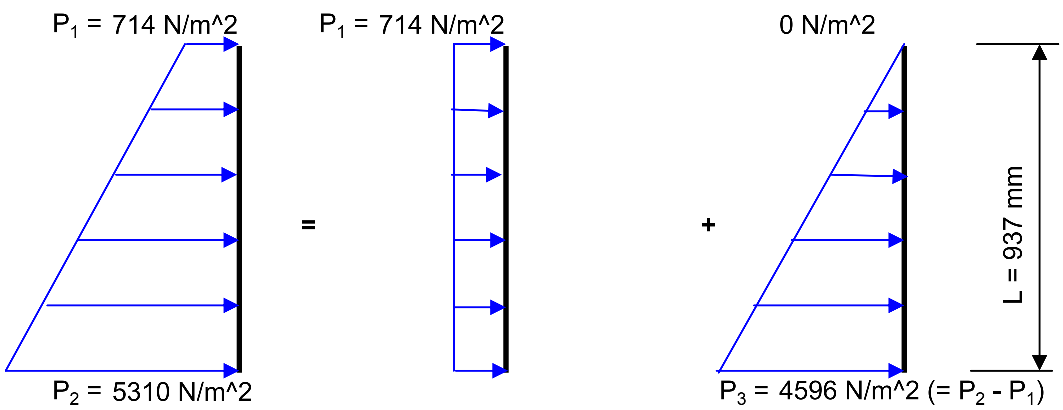

Total Pressure Field = Uniform Pressure + Hydrostatic Pressure

Analysis of Uniform Pressure on Glass for Reaction Forces / unit width

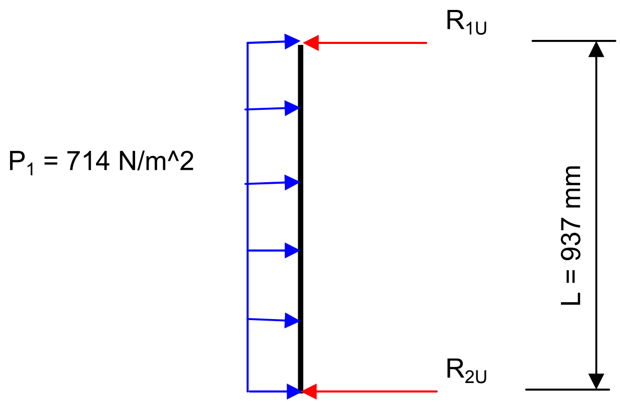

$R_{1U} = R_{2U} =$ P_1*L/2

= 334.5 N/m

Results for Stress and Deflection

EES program adapted from emprical formulas in R.J. Roark and W.C. Young, 1975:
Formulas for Stress and Strain - Fifth Edition

Fixed Supports			Simple Supports			Average Values		
Stress =	8.42	Mpa	Stress =	9.68	Mpa	Stress =	9.05	Mpa
Defl'n =	0.97	mm	Defl'n =	3.65	mm	Defl'n =	2.31	mm

Analysis of Hydrostatic Pressure on Glass for Reaction Forces / unit width

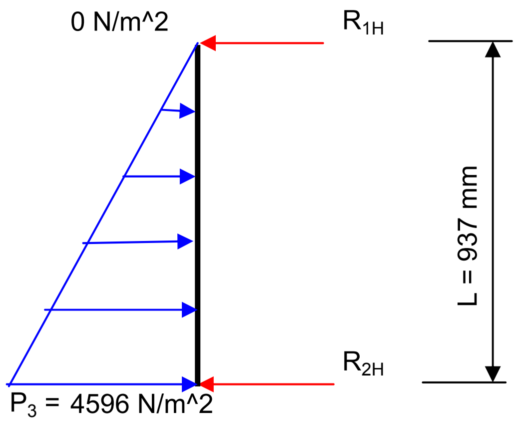

R_{1H} = P_3*L/6

= 718 N/m

R_{2H} = P_3*L/3

= 1435 N/m

Results for Stress and Deflection

EES program adapted from emprical formulas in R.J. Roark and W.C. Young, 1975:
Formulas for Stress and Strain - Fifth Edition

Fixed Supports			Simple Supports			Average Values		
Stress =	35.07	Mpa	Stress =	32.93	Mpa	Stress =	34	Mpa
Defl'n =	3.13	mm	Defl'n =	11.8	mm	Defl'n =	7.465	mm

Analysis of Total Pressure Field by Superposition

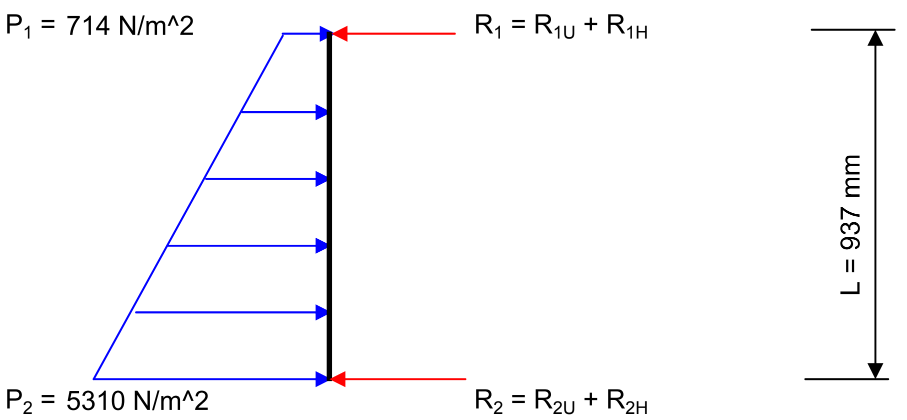

$R_1 = R_{1U} + R_{1H}$ = 1052 N/m

$R_2 = R_{2U} + R_{2H}$ = 1770 N/m

Stress and Deflections by Superposition

Uniform

Fixed Supports			Simple Supports			Average Values		
Stress =	8.42	Mpa	Stress =	9.68	Mpa	Stress =	9.05	Mpa
Defl'n =	0.97	mm	Defl'n =	3.65	mm	Defl'n =	2.31	mm

Hydrostatic

Fixed Supports			Simple Supports			Average Values		
Stress =	35.07	Mpa	Stress =	32.93	Mpa	Stress =	34	Mpa
Defl'n =	3.13	mm	Defl'n =	11.8	mm	Defl'n =	7.465	mm

TOTAL STRESS AND DEFLECTION VALUES (Uniform + Hydrostatic)

Fixed Supports			Simple Supports			Average Values		
Stress =	43.49	Mpa	Stress =	42.61	Mpa	Stress =	43.05	Mpa
Defl'n =	4.1	mm	Defl'n =	15.45	mm	Defl'n =	9.775	mm #

* Self weight of glass not accounted for in calculations

Actual measured deflection is approximately 10 mm
=> Average is reasonable value to use

APPENDIX G

Output From Efunda Hardness Convertor

http://www.efunda.com/units/hardness/convert_hardness.cfm?HD=HRC&Cat=Steel#ConvInto

Search AllMaterialsDesign CenterProcessesUnits and ConstantsFormulasMathematics for Rockwell C-Scale Hardness Brale indenter, 150 kgf load

Symbol: HRC

The Rockwell Hardness Test presses a steel or diamond hemisphere-conical penetrator against a test specimen and measures the resulting indentation depth as a gage of the specimen hardness. The harder the material, the higher the HR reading. In the test, a minor load (10 kgf) is first applied, and the test dial (measuring the indention depth) is reset to zero. Then a major load (60, 100, or 150 kgf) is applied to create the full indention. The major load is reduced back to the minor load, and the indention depth measurement is taken. The penetrator is usually 1/16 inch in diameter, although larger diameters (such as 1/8 inch) may be used for softer metals. Choosing the proper penetrator and the corresponding load requires experience. Some commonly used combinations are summarized below:

Scale Condition Application

A Brale indenter

60 kgf load Thin, hard sheet materials, such as tungsten carbide.

B 1/16 in diamond ball

100 kgf load Medium/low hard materials, such as annealed carbon steels.

C Brale indenter

150 kgf load Materials harder than HRB 100.

D Brale indenter

100 kgf load Case-hardened materials.

F 1/16 inch Brale indenter

60 kgf load Soft materials, such as bearing metals.

N 1/16 inch Superficial Brale indenter

15, 30, or 45 kgf load Unhardened materials, such as metals softer than hardened steel or hard alloys, or where shallow indentations are desired.

T 1/16 inch diamond ball
15, 30, or 45 kgf load Unhardened materials, such as metals softer than hardened steel, or where shallow indentations are desired.
Convert HRC
(suggested range: 19 ~ 69)

HRC 44 approximately* =

Hardness Symbol	Amount	Name	Suggested Range
HB (3000)	411	Brinell 10 mm Standard 3000 kgf	80~445
HB (500)	>>	Brinell 10 mm Standard 500 kgf	89~189
HB (Tungsten 3000)	411	Brinell 10 mm Tungsten 3000 kgf	80~620
HB (Indentation)	3.02 mm	Brinell Indentation	6~2
HK	456	Knoop	97~920
HM	4	Mohs	1~10
HRA	73	Rockwell A-Scale	59~86
HRB	>>	Rockwell B-Scale	41~100
HRD	59	Rockwell D-Scale	39~77
HRF	>>	Rockwell F-Scale	88~100
HR-15N	83	Rockwell Superficial 15N	69~94
HR-15T	>>	Rockwell Superficial 15T	77~93
HR-30N	63	Rockwell Superficial 30N	41~85
HR-30T	>>	Rockwell Superficial 30T	53~82
HR-45N	48	Rockwell Superficial 45N	19~76
HR-45T	>>	Rockwell Superficial 45T	28~71
HS	59	Shore Scleroscope	17~97
HV	436	Vickers	20~1800
Approx. TS	1434 MPa	Tensile Strength (Approx.)	390~2450

Legend

<< The hardness value is below the acceptable range of the particular hardness scale.

>> The hardness value is above the acceptable range of the particular hardness scale.

The hardness value is near the limit (within 15%) of the acceptable range of the particular hardness scale.

* The many hardness tests listed here measure hardness under different experimental conditions (e.g. indenters made in different sizes, shapes, and materials, and applied with different loads) and reduce their data using different formulae. As a result, there is NO direct analytic conversion between hardness measures. Instead, one must correlate test results across the multiple hardness tests.

This calculator is based on hardness data compiled from ASM Metals Reference Book 3rd ed, published by ASM International, and Machinery's Handbook 25th ed, published by Industrial Press. The calculator curve-fits multiple hardness data onto a common polynomial basis and then performs an analytic conversion. The accuracy of the conversion depends on the accuracy of the provided data and the resulting curve-fits, and on the valid ranges spanned by the different hardness tests. Converted hardness values should be used for comparative purposes only.

ASM Metals Reference Book , 3rd ed., by Bauccio, M. (ed.) Machinery's Handbook , 26th ed., by Oberg, E., Jones, F.D., Horton, H.L., Ryffel, H.H.

APPENDIX H

Hydrostatic Stress Curves for PP – B

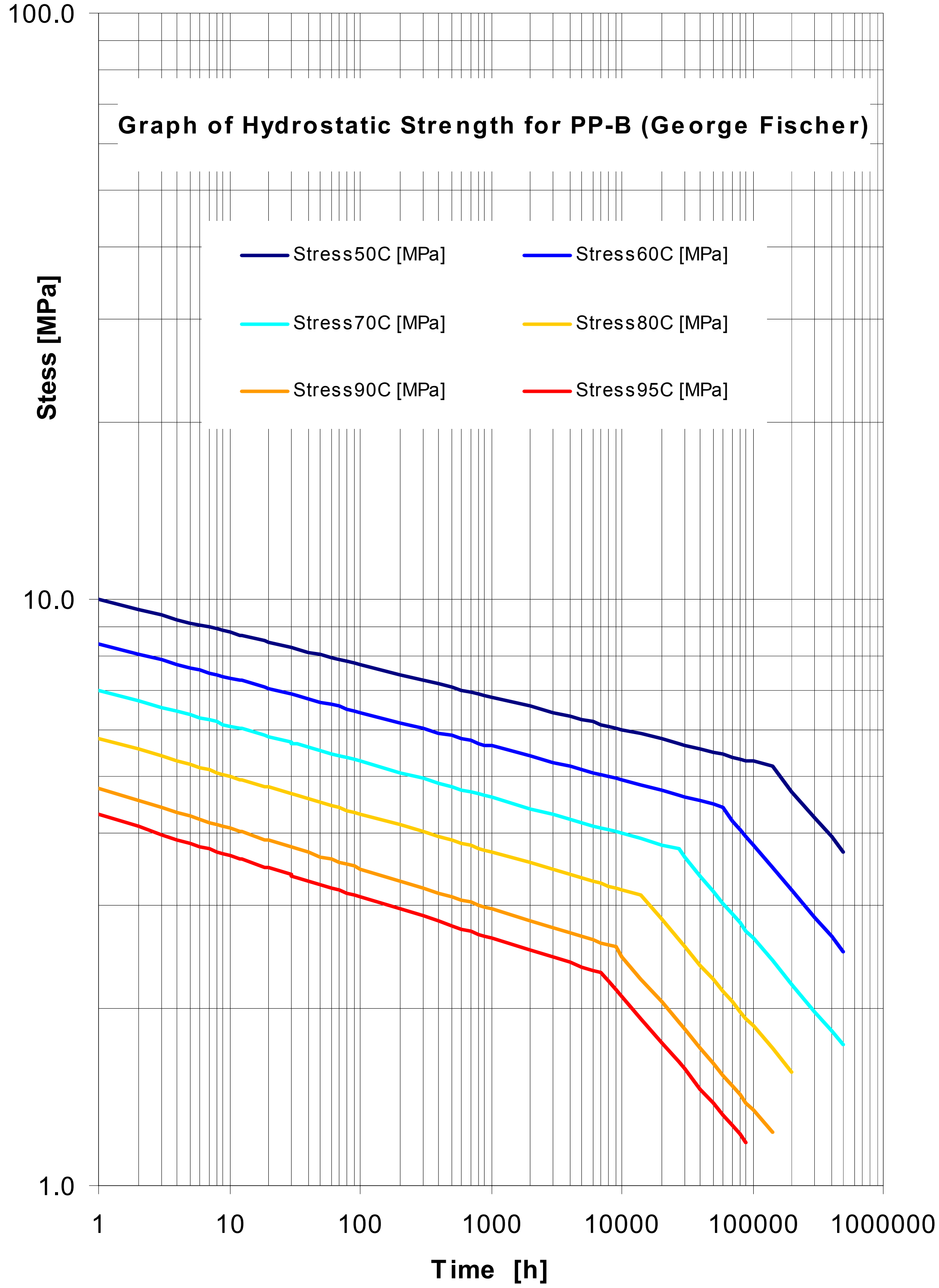

APPENDIX I: Results of Finite Element Analyses on Spring Clip

DEFLECTION [mm]	APPLIED FORCE 0.8 mm CLIP [N]	0.9 mm CLIP [N]	1.0 mm CLIP [N]
0	0	0	0
2.85	48.5	69	94
4.27	73	103.5	141
8.54	146	207	282
14.23	243.5	346	473
17.08	292	415	564
21.35	365	518	705

DEFLECTION [mm]	Von Mises STRESS 0.8 mm CLIP [MPa]	0.9 mm CLIP [MPa]	1.0 mm CLIP [MPa]
0	0	0	0
2.85	256.4	287.5	316.2
4.27	385.9	431.3	474.2
8.54	771.7	862.5	948.5
14.23	1287	1442	1591
17.08	1543	1729	1897
21.35	1929	2158	2371

DEFLECTION [mm]	SPRING CONSTANT 0.8 mm CLIP [N/mm]	0.9 mm CLIP [N/mm]	1.0 mm CLIP [N/mm]
0	0	0	0
2.85	17.0	24.2	33.0
4.27	17.1	24.2	33.0
8.54	17.1	24.2	33.0
14.23	17.1	24.3	33.2
17.08	17.1	24.3	33.0
21.35	17.1	24.3	33.0

DEFLECTION [mm]	FACTOR OF SAFETY AT 45 HRC (tensile strength = 1435 Mpa) 0.8 mm CLIP [N/mm]	0.9 mm CLIP [N/mm]	1.0 mm CLIP [N/mm]
0	0	0	0
2.85	5.6	5.0	4.5
4.27	3.7	3.3	3.0
8.54	1.9	1.7	1.5
14.23	1.1	1.0	0.9
17.08	0.9	0.8	0.8
21.35	0.7	0.7	0.6

DEFLECTION [mm]	FACTOR OF SAFETY AT 50 HRC (tensile strength = 1703 Mpa) 0.8 mm CLIP [N/mm]	0.9 mm CLIP [N/mm]	1.0 mm CLIP [N/mm]
0	0	0	0
2.85	6.6	5.9	5.4
4.27	4.4	3.9	3.6
8.54	2.2	2.0	1.8
14.23	1.3	1.2	1.1
17.08	1.1	1.0	0.9
21.35	0.9	0.8	0.7

APPENDIX J - SUMMARY OF RESULTS OF FINITE ELEMENT ANALYSIS												
Case	Clip size	Base shot weight	Oring groove radius	Clip opening initial	Clip opening installed	Clip load	Clip load contact area	Tilt angle	Oring load contact area = 4 mm	Backing strip	Backing strip contact area	Maximum von Mises Stress
[-]	[mm]	[kg]	[mm]	[mm]	[mm]	[N]	[mm]	[deg]	[N]	[-]	[mm]	[MPa]
1	1.0	20	0.6	1	14	424	3	0	424	no	na	20.82
2	1.0	20	1.2	1	14	424	3	0	424	no	na	12.85
3	1.0	20	2.0	1	14	424	3	0	424	no	na	9.89
Increase shot weight to 30 kg												
4	1.0	30	2.0	1	16.2	496	3	0	496	no	na	5.39
Change to 0.9 mm clips												
5	0.9	30	2.0	1	16.2	340	3	0	340	no	na	3.69
Incorporate backing strip pressure field approximation												
6	0.9	30	2.0	1	18.2	384	3	0	384	Yes	6	3.24
7	0.9	30	2.0	1	18.2	384	3	0	384	Yes	8	3.20
Apply tilt angle to collector												
8	0.9	30	2.0	1	18.2	384	na	10	322	Yes	8	2.90
9	0.9	30	2.0	1	18.2	384	na	15	292	Yes	8	3.20
10	0.9	30	2.0	1	18.2	384	na	20	263	Yes	8	3.50
11	0.9	30	2.0	1	18.2	384	na	25	234	Yes	8	3.79
12	0.9	30	2.0	1	18.2	384	na	30	207	Yes	8	4.07
Use contact analysis with aluminium strip in assembley												
13	na	30	2.0	na	na	200	3	0	200	Yes	na	1.7
14	na	30	2.0	na	na	200	3	30	23	Yes	na	2.5
15	na	30	2.0	na	na	250	3	0	250	Yes	na	2.1
16	na	30	2.0	na	na	250	3	30	73	Yes	na	2.6
17	na	30	2.0	na	na	300	3	0	300	Yes	na	2.5
18	na	30	2.0	na	na	300	3	30	123	Yes	na	2.8

APPENDIX K

Sensitivity analysis of the component combination

The purpose of this Appendix is to explore the sensitivity of the specified component combination to variations in component geometry due to normal manufacturing tolerances. There are three significant parameters that may effect a change in the stress imparted on the polypropylene base component. The parameters are:

a) The initial opening of the spring clip – I [mm]
   $I = 2.66 \pm 0.5$ mm
   An increase of initial opening decreases clamping force and stress
   A decrease of initial opening increases clamping force and stress

b) The spring constant of the spring clip[3] – K [N/mm]
   $K = 16.35 \pm 1$ N/mm
   An increase of spring constant increases clamping force and stress
   A decrease of spring constant decreases clamping force and stress

c) The thickness of the polypropylene base component in the region where the clip contacts the backing strip – T [mm]
   $T = 8\text{mm} \pm 0.5$ mm
   An increase in part thickness increases clamping force and stress
   A decrease in part thickness decreases clamping force and stress

The dimensions of the aluminium backing strip (2 mm), the inner glazing (6 mm) and the o-ring (adds 1 mm gap between glazing and base) are considered constant when compared with those of the above parameters. The nominal installed opening of the clip considering the above dimensions is 17 mm (see Figure 10 for general arrangement of components).

[3] The tolerance is assumed to be equal to 3 standard deviations of the sample set measured (std dev. = 0.33 mm) such that all expected variations are accounted for.

As the highest stress in the region of interest in the polypropylene component occurs at 30 degrees collector tilt angle, the following expression for stress was developed from data in Table 6 for 30 degrees tilt angle.

$\sigma_{vm} = 3.1 - 0.007 \times CF + 0.00002 \times CF^2$ [MPa]

where;

σ_{vm} = maximum von Mises stress in the polypropylene part [MPa]

and

CF = clamping force applied by the spring clips [N/clip]

Also

$CF = K \times (T + 9 - I)$

where;

K = spring constant [N/mm]

T = the plastic part wall thickness [mm]

I = the initial opening of the clip [mm]

9 = the combined dimension of the glass (6 mm), the oring gap (1 mm) and backing strip (2 mm) [mm]

Table K.1. shows the combinations of components that impart both the upper and lower limits of stress on the polypropylene base component.

Table K.1. Sensitivity of Component Combinations to Manufacturing Tolerances

	Clip Initial Opening I [mm]	Clip Spring Constant K [N/mm]	Part Wall Thickness T [mm]	Clamping Force CF [N]	FOS Clip Force [-]	Maximum Von Mises Stress [MPa]	FOS Von Mises Stress [-]
Nominal Stress	2.66	16.35	8.0	234.5	1.32	2.56	1.02
Upper Limit Stress	2.16	17.35	8.5	266.1	1.50	2.65	0.98
Lower Limit Stress	3.16	15.35	7.5	204.8	1.16	2.51	1.04

The factor of safety with respect to clip force assumes 177 N/clip being the clamping force required to overcome the reaction force applied by the inner glazing due to internal hydrostatic pressure.

The analysis of the reaction forces does not account for end effects due to the small aspect ratio of the collector dimensions. Taking the end effects into account may allow the nominal reaction force to be reduced. This in turn allows the nominal initial opening of the clips to be increased such that the maximum stress in the plastic part becomes less than 2.6 MPa. The chart of long term hydrostatic stress versus time used to determine the maximum allowable stress may be viewed in Appendix H. Further investigation of this aspect of the collector design was performed.

The factor of safety with respect to von Mises stress is relative to the aforementioned maximum allowable stress of 2.6 MPa to ensure a ten year lifetime of the product under very conservative temperature profile approximations. It may not be necessary to reduce the nominal clamping force applied by the clips as the probability of the upper limit stress occurring in a collector that is exposed to the very conservative temperature profile is considered minimal.

A collector filled with water was mounted on a frame such that the tilt angle of the collector was adjustable. According to the above analysis, a nominal collector should begin to leak past the o-ring seal when the reaction force due to the internal hydrostatic pressure reaches 1.32 times that at 30 degrees tilt. This reaction force corresponds to a collector tilt angle of 41.3 degrees. In practice, the collector did not begin to leak water past the o-ring seal until the tilt angle had reached 53.5 degrees. The difference in tilt angles for the practical and theoretical cases indicate that end effects due to small aspect ratio provide an additional factor of safety of 1.2 with respect to clamping force.

Considering the collector that was tested to represent the norm, the factor of safety with respect to clamping force shown in Table P.1 may be multiply by a factor of 1.2. This finding allows scope to reduce the clamping force applied by the clips via larger nominal initial opening. Values corresponding to this scenario may be seen in Table K.2.

Table K.2. Sensitivity of Component Combinations to Manufacturing Tolerances with Modified Factor of Safety with respect to Clamping Force

	Clip Initial Opening I [mm]	Clip Spring Constant K [N/mm]	Part Wall Thickness T [mm]	Clamping Force CF [N]	FOS Clip Force [-]	Maximum Von Mises Stress [MPa]	FOS Von Mises Stress [-]
Nominal Stress	4.9	16.35	8.0	197.8	1.34	2.50	1.04
Upper Limit Stress	4.4	17.35	8.5	227.3	1.54	2.54	1.02
Lower Limit Stress	5.4	15.35	7.5	170.4	1.16	2.49	1.05

APPENDIX L – Collector Efficiency Correction Report

Optical Efficiency of Hot Harry™ Solar Water Heater

By Harry Suehrcke & Rodney Lowe

March 2003

Executive Summary

Indoor performance testing of the Gough Plastics Hot Harry™ solar water heater was performed at the Plumbing Testing Laboratory (P.T.L.) in Perth using artificial lights. The artificial lights produced diffuse radiation with a spectrum of generally longer wavelength than that of the sun, resulting a significant reduction in transmittance through the top cover system (acrylic cover and honeycomb). The outdoor and indoor transmission through the top cover were measured as 0.875 and 0.628, respectively.

The strong reduction in transmission through the top cover system is largely a result of spectral absorption, which occurs at wavelengths greater than 1.1 μm in the acrylic cover and the cellulose acetate honeycomb. Section 9.2 of AS2535 requires a correction of the transmission-absorptance product when the simulator radiation spectrum differs from the solar spectrum and the top cover is affected by spectral absorption.

This communication details that correction by determining the relationship between the measured optical efficiency in the P.T.L. simulator and the normal incidence outdoor optical efficiency[4]. Based on several independent measurements and calculations it is shown that the measured indoor optical efficiency of 0.68 should be corrected to an outdoor value of 0.83.

---

[4] It is noted that in normal operation of the HH heater the optical efficiency is equal to the effective transmittance-absorptance product ($\tau\alpha$) as the heat removal is considered through the heat exchanger efficiency.

1. Introduction

During the recent indoor performance tests of the Hot Harry™ (HH) solar water heater at the Plumbing Testing Laboratory (P.T.L.) in Perth the following performance parameters were determined (neglecting the second order temperature dependence on the heat loss coefficient[5]):

Optical efficiency $F_R(\tau\alpha) = 0.678$
Product of heat removal factor and heat loss coefficient $F_RU_L = 3.21$ W/m^2.K

For the performance test the heater was operated as a collector with a mass flow rate of 0.02 kg/s per square meter aperture area. Using the measured F_RU_L product and eqn 6.7.5 from ref [1], the individual values of the heat removal factor, heat loss coefficient and transmittance-absorptance product can be determined. For a collector efficiency factor F' = 1.0[6] the heat removal factor F_R = 0.981, the heat loss coefficient U_L = 3.28 W/m^2.K and the transmittance-absorptance product $(\tau\alpha) = 0.692$.

While the heat loss coefficient is in line with expectations, the optical efficiency is significantly lower than anticipated. An optical efficiency of above 80% was expected from experience with, and measurements of, HH outdoor performance.

This anomaly has prompted us to investigate the radiation characteristics of the P.T.L. solar simulator. The investigation found that the low optical efficiency is the result of the solar simulator lights producing:

- Diffuse radiation; and

---

[5] The complete equation for the measured indoor Hot Harry collector efficiency is:

$$\eta = 0.6783 - 3.213\left(\frac{T_i - T_a}{G_T}\right) - 0.00115\left(\frac{(T_i - T_a)^2}{G_T}\right)$$

A plot of the efficiency can be found in Appendix C.

[6] The temperature transverse to the flow direction is assumed to be uniform for the Hot Harry solar water heater

- Radiation of longer wavelength than found in the solar spectrum

A picture of the performance testing set up is shown in Fig. 1.

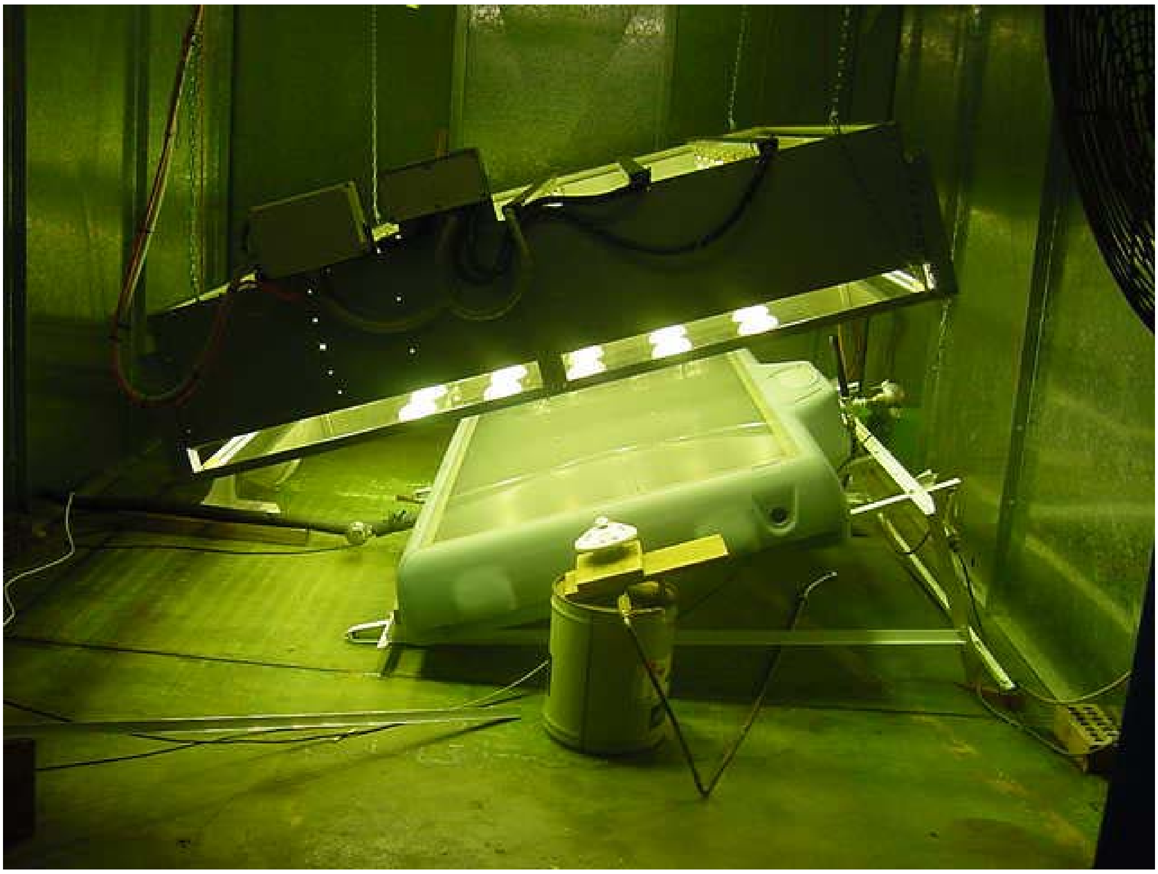

Fig. 1. Hot Harry™ indoor performance testing at P.T.L. with low iron glass filter.

2. Simulator Radiation Spectrum and Long Wave Radiation Filter

It was recognised before the test that a significant energy component of the radiation emitted from the P.T.L. simulator lights had wavelength $> 3\ \mu m$[7]. One problem with this long wave radiation is that it remains undetected by conventional glass dome pyranometers, which block radiation of wavelength longer than 3 μm (see Fig. 5.7.1 in ref [1] for spectral transmission characteristics of glass). Moreover, the thermal radiation caused an unacceptable heating of the collector.

In order to comply with the thermal irradiance requirements of AS2535 for indoor testing (Section 9.2), the testing was performed with a sheet of low iron glass between the simulator lights and the collector (see also Fig. 1). The purpose of the low iron glass filter was to block simulator radiation with a wavelength $> 3\ \mu m$.

The low iron glass filter greatly reduced the problem with thermal radiation of wavelength $> 3\ \mu m$. Subsequent measurements of the low iron glass temperature suggested that the glass was only about 20 K above ambient (the glass was well ventilated from above with a ceiling fan). The low iron glass filter, as apparent from Fig. 5.7.1 in ref [1], however, does not in any significant way alter the radiation spectrum from the artificial lights below 3 μm. Refer to Appendix A for a further discussion of the simulator radiation spectrum.

3. Solar and Simulator Radiation Transmission through Top Cover System

There is a significant difference between the transmission of the top cover system (acrylic outer glazing and honeycomb) under solar radiation and the radiation generated by the P.T.L. simulator lights. AS2535 recognizes that the performance of most collectors is generally better in direct solar radiation than in diffuse radiation from an indoor simulator (Section 9.1). The Standard requires a correction to be applied to the

---

[7] This is not surprising as the array of 40 Philips MUL 300 W F/28 light bulbs had a steady state glass bulb temperature of around 200°C (Measured with an infrared thermometer).

transmittance absorptance product ($\tau\alpha$) when there is spectral absorption in the top cover and the simulator spectrum differs from the solar spectrum (see Section 9.2).

The transmittance of the top cover system was measured under both outdoor and simulator radiation. The experimental results, obtained with a CM 21 Kipp & Zonen pyranometer and the experimental apparatus shown in Appendix B, are presented in Fig. 2.

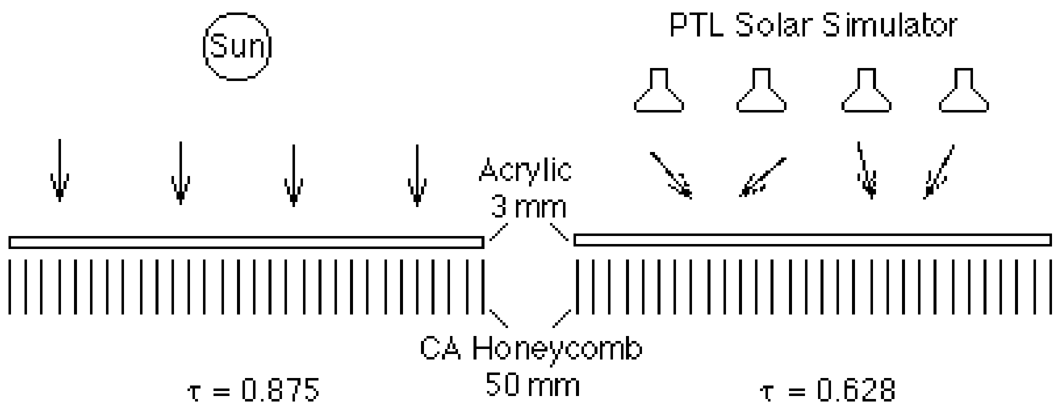

Fig. 2. Transmission through Hot Harry™ top cover (acrylic glazing and honeycomb) under normal incidence outdoor solar and indoor simulator radiation.

The outdoor normal incidence transmission test was performed under clear sky at the P.T.L. grounds in Perth. The outdoor results agree with expectations derived from the manufacturers' specifications for transmission of each component. However, the indoor transmission is significantly lower than anticipated and is a result of transmission loss due to both diffuse radiation and spectral absorption in the top cover system.

The spectral absorption in the outer cover system can be understood from the spectral transmission characteristic of the acrylic cover and the cellulose acetate honeycomb materials. At wavelength > 1.1 μm both materials exhibit strong spectral absorption. The spectral radiation transmission of the acrylic outer cover is shown in Fig. 3.

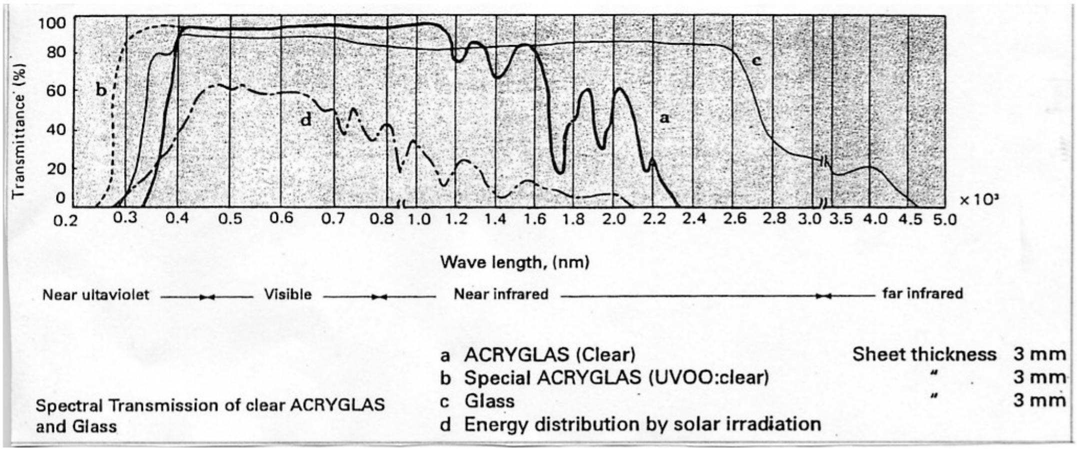

Fig. 3. Spectral Transmission through the outer 3 mm acrylic cover (from: Technical Data Brochure - ACRYGLAS cast acrylic sheet).

It is apparent from the black solid line in Fig. 3 that the transmission of the 3 mm Acylglas sheet used as the outer cover in the Hot Harry™ heater reduces for wavelength greater than 1.1 μm. Since 43% of energy of the P.T.L. simulator radiation has a wavelength greater than 1.1 μm (instead of 20% for solar radiation – see Annex C of AS2535) it is understandable that a reduced transmission (due to spectral absorption) should be observed. In fact in a transmission measurement of the Acryglas sheet alone it was found that the measured transmission was reduced from 91% to 68% when it was exposed to the simulator radiation instead of solar radiation!

The spectral absorption in the acrylic cover was also evident from its temperature, which reached 75°C during the performance testing when it was exposed to 875 W/m^2 radiation.

4. Suggested Correction to Optical Efficiency

One may be tempted to take the difference in transmission through the top cover system (= 0.875 – 0.628) as the correction for the optical efficiency. However, this simple approach ignores the fact that some of the absorbed radiation is useful, particularly if the absorption occurs deep below the outer glazing. The fraction of absorbed solar radiation that is useful can in principle be determined with the analysis presented in ref [1], "6.10 Effective Transmittance-Absorptance Product". However, that analysis assumes that the point of absorption and the heat transfer coefficients (overall and outside) are known.

Here a more direct analysis is employed. Consider the cross sectional view through the Hot Harry™ water heater shown in Fig. 4.

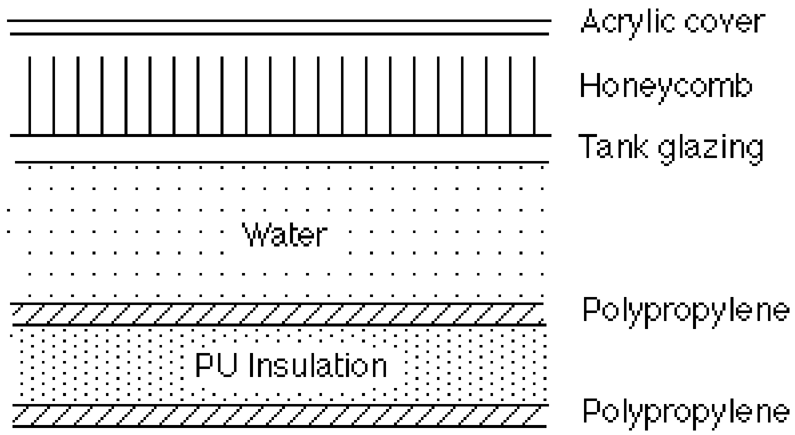

Fig. 4. Schematic diagram of cross section of Hot Harry™ water heater.

Once the radiation has passed through the outer acrylic cover and the honeycomb (transmittance = 0.875) there is one more interface for the radiation to go through before it is absorbed. This is the air-glass interface between the honeycomb and tank glazing (see Fig. 4). The reflection at a single air-glass interface can be calculated from Fresnel's equations (e.g., see ref. [1], Section 5.1). For unpolarised normal incidence light the single interface reflectance is:

$$r(0) = \left(\frac{n_1 - n_2}{n_1 + n_2} \right)^2 \tag{1}$$

where n_1 and n_2 denote the refractive indices of the material above and below the interface, respectively. For air (n_1 = 1.00) and glass (n_2 = 1.53) eqn 1 gives a normal incidence interface reflectance of 0.043. Once the radiation has penetrated the tank glazing the reflection is very small and nearly all radiation will be absorbed.

This latter claim of near complete absorption below the tank upper surface can be justified by considering the refractive indices of glass (1.53), water (1.33) and polypropylene (1.49). Using the tank glass-water interface, for example, eqn (1) yields a reflection of only 0.005 (= 0.5%). Approximately 84% of radiation incident on the tank glazing reaches the water glass interface and 42% the water-polypropylene interface[8]. Using a value of 4.3% + 0.84 × 0.5% + 0.42 × 0.5% = 4.9% for the total reflection loss from the glazed water chamber, suggests that the effective transmittance-absorptance product, as defined in AS2535, should be:

$$Effective(\tau\alpha) = \frac{\int_{0.3\,\mu m}^{3.0\,\mu m} \tau(\lambda)\alpha(\lambda)G(\lambda)d\lambda}{\int_{0.3\,\mu m}^{3.0\,\mu m} G(\lambda)d\lambda} = 0.875 \times 0.951 = 0.832 \qquad (2)$$

As already mentioned in Section 1, for the Hot Harry™ heater the optical efficiency in normal operation is equal to the effective (τα) as the heat removal is considered through the heat exchanger efficiency.

We can also estimate the effective transmission-absorptance product from the measured optical efficiency and transmission through the top cover system. For the collector in the P.T.L. simulator to have an optical efficiency F_R (τα) = 0.678 with a transmission of only 0.628 through the cover system and an extra water chamber reflection loss of about 4.9% implies that $0.678/F_R - (0.628 - 0.049)$ of the radiation absorbed in the top cover system must be useful.

Subtracting the useful absorption from the difference in outdoor and indoor transmission gives the correction that should be applied to the measured transmittance - absorptance product:

[8] The tank glazing that is made from ordinary glass absorbs approximately 12% of solar radiation. About half of the solar radiation penetrating the water is transmitted to the bottom of the tank [2].

$$\begin{aligned}&\{outdoor\ transmission - indoor\ transmission\} - \{useful\ absorption\}\\&= \{0.875 - 0.628\} - \{0.678/0.981 - 0.579\} = 0.135\end{aligned} \qquad (3)$$

Adding the above correction to the measured transmittance -absorptance product gives

$$\{Effective\ (\tau\alpha)\} = 0.678/0.981 + 0.135 = 0.826 \qquad (4)$$

The above calculations are not completely independent as they both assume a reflectance of 0.049 of water storage chamber. It is suggested that 0.83 be adopted as the effective ($\tau\alpha$) value for operating in the solar spectrum[9].

5. Cover System Absorption and Heat Loss Coefficient

It was shown in Section 3 that there is considerable absorption in the cover system (acrylic cover and honeycomb) when it is exposed to the P.T.L. simulator radiation. One may therefore ask if this absorption influences the heat loss coefficient from the collector.

If we assume the heat loss coefficient to be independent of temperature (linear heat transfer analysis), then the effect of the absorption is superimposed on the collector heat loss and the heat loss coefficient is not changed by the top cover absorption. A derivation for this is provided by Duffie and Beckman [1] in Section 6.10 "Effective Transmittance-Absorptance Product".

6. Corrected Performance Parameters for Outdoor Radiation

Based on the above measurement and calculations and incidence angle modifier results from Appendix B the following performance parameters are suggested for Hot Harry™

[9] This is a conservative assumption as the above calculations neglect any absorption in the top cover system and absorption of the radiation that gets reflected from the water tank.

outdoor use:

Effective transmittance-absorptance product ($\tau\alpha$) = 0.83

Heat loss coefficient U_L = 3.28 W/m^2.K

Incidence angle modifier $K_{\tau\alpha} = 1 - 0.27\left(\frac{1}{\cos(\theta)} - 1\right)$

The measured and corrected efficiency is plotted in Appendix C.

Acknowledgment

We would like to acknowledge the friendly and professional attitude of the manager, Mr. Hank Vandenberg of Plumbing Testing Laboratory (P.T.L.) and Dr. Trevor Pryor from Murdoch University, which enabled many of the measurement contained in this report to be carried out.

References

[1] Duffie, J. A. and Beckman, W. A., *Solar Engineering of Thermal Process*, 2nd edition, Wiley, 1991.

[2] R. Siegel and J.R. Howell, *Thermal radiation heat transfer*, p. 157, 2nd ed., McGraw-Hill, New York (1981).

[3] Dreuning, H. J., *Personnel Communication*, Philips, Netherlands, 2002.

Appendix A

Significant effort was made to find the spectral distribution of the P.T.L. simulator radiation. No distribution of the spectral emission characteristics of the simulator lights was available at the P.T.L. lab. The manufacturer Philips in Belgium was contacted, however, the manufacture of the MUL 300 W F/28 lights was discontinued more than 10 years ago and no records about the spectral emission characteristics were retrievable [3]. It was decided to make at least a rudimentary characterisation of the light energy distribution.

The energy distribution of the simulator radiation spectrum was quantified by measuring the radiation with a LiCor photovoltaic (PV) pyranometer, which does not register radiation above 1.1 μm wavelength, and a Kipp & Zonen CM 21 thermal pyranometer which measures radiation up to 3 μm wavelength. The measured output at about 500 mm separation distance between the low iron filter glass and the pyranometers was 367 W/m^2 for the PV pyranometer and 648 W/m^2 from the thermal pyranometer. This suggests that the (filtered) simulator light has less than 57% of energy below 1.1 μm. For comparison the solar spectrum has about 80% of energy below 1.1 μm wavelength (Annex C, AS2535). This confirms that the simulator radiation is generally of longer wavelength than solar radiation.

Using the above figures on the energy distribution, approximate blackbody radiation spectra have been drawn for both solar and simulator radiation in Fig. A.1. The spectral distribution for the simulator radiation has been drawn such that the black body radiation spectrum has 57% of radiant energy below 1.1 μm. This, of course, is only a very crude approximation and cannot provide the details of the actual distribution.

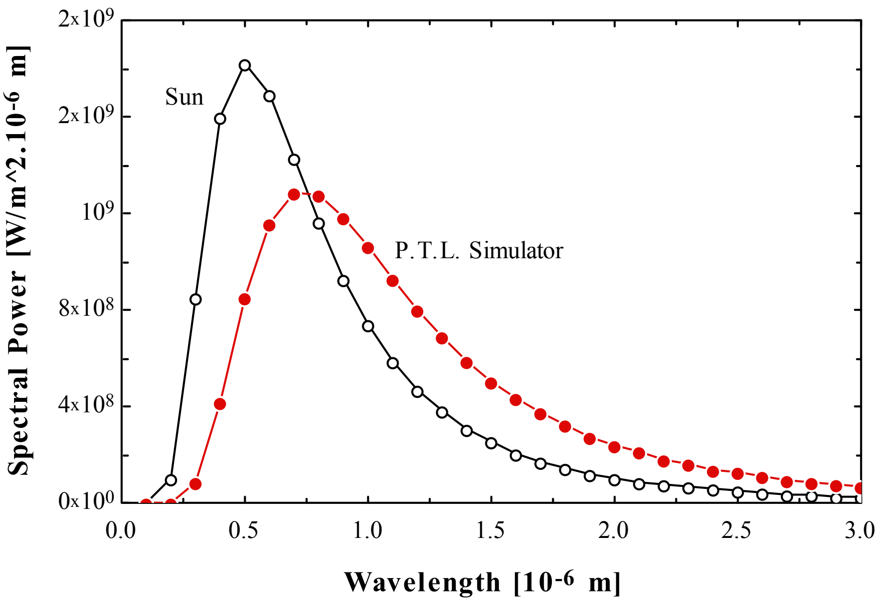

Fig. A.1. Radiation distribution for solar and P.T.L. simulator.

The diffuse nature of the simulator light is illustrated in Fig. A.2. It is clearly seen from the reflection on the white paper on the inside of the simulator light frame that the lights emit a radiation in "sideways" direction. The diffuse emittance of the simulator lights can also be understood from their design, which provides for a broad angle of emission and a mat surface finish.

Fig. A.2. Diffuse light incident on the inside of the simulator frame.

Appendix B

The diffuse nature of the simulator radiation required determination of the incident angle modifier from a separate outdoor test and calculation. For this purpose the apparatus shown in Fig. B.1 was used to measure the solar transmission of the acrylic cover and honeycomb.

Fig. B.1. Apparatus for the transmission test of the top cover system (3 mm acrylic cover + 50 mm cellulose acetate honeycomb).

The honeycomb was suspended with thin fishing wire so that (as in the HH heater) there was a 5 mm air gap between the acrylic cover and the honeycomb. Eppley and Kipp & Zonen and pyranometers were used to measure the incident radiation on top of the apparatus and the radiation below the honeycomb. The ratio between the two radiation measurements provided the transmission through the top cover system and is plotted in Fig. B.2.

The experimental data shown in Fig. B.2 are the result of transmission measurements of three days that were obtained by placing the inside pyranometer at different positions under the honeycomb. The latter repositioning of the inside pyranometer is required, as the honeycomb tends to locally concentrate the radiation, which cannot be averaged out with a single transmission measurement. The solid line represents a line of best fit to the data representing the average transmission. In this context it is noted that the normal incidence outdoor transmission of the top cover system that was presented in Fig. B2 was measured in a separate test and was <u>not</u> derived from the incident angle data presented in this section.

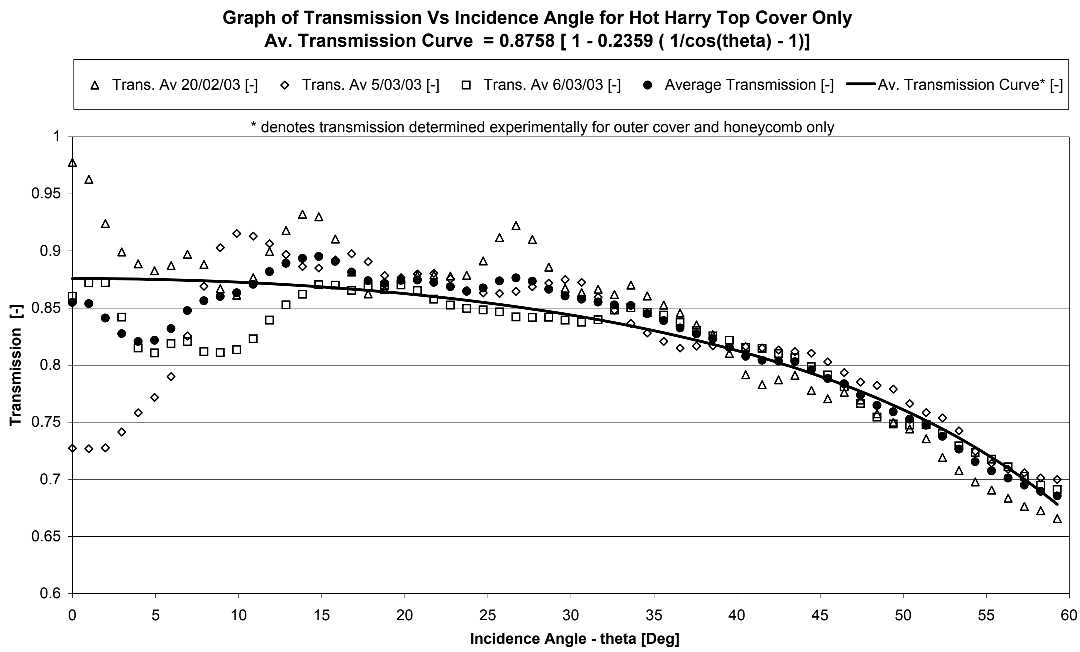

Fig. B.2. Transmission through the top cover system (acrylic cover + honeycomb).

Having obtained the average transmission through the top cover, we now also include the reflection from the water chamber below the honeycomb. It is very difficult to directly measure the chamber reflection with incident angle. However, we know from Section 4 this reflection almost entirely consists of light reflection from the upper tank glass surface, which can be accurately calculated from Fresnel's eqns. The small reflection from below the tank glass surface (< 0.6% at normal incidence) is assumed fixed independent of incidence angle. The transmitttance-absorptance product is obtained from the product of top cover transmission and water chamber absorption (= 1 – water chamber reflection). The result and approximating equation are shown in Fig. B.3.

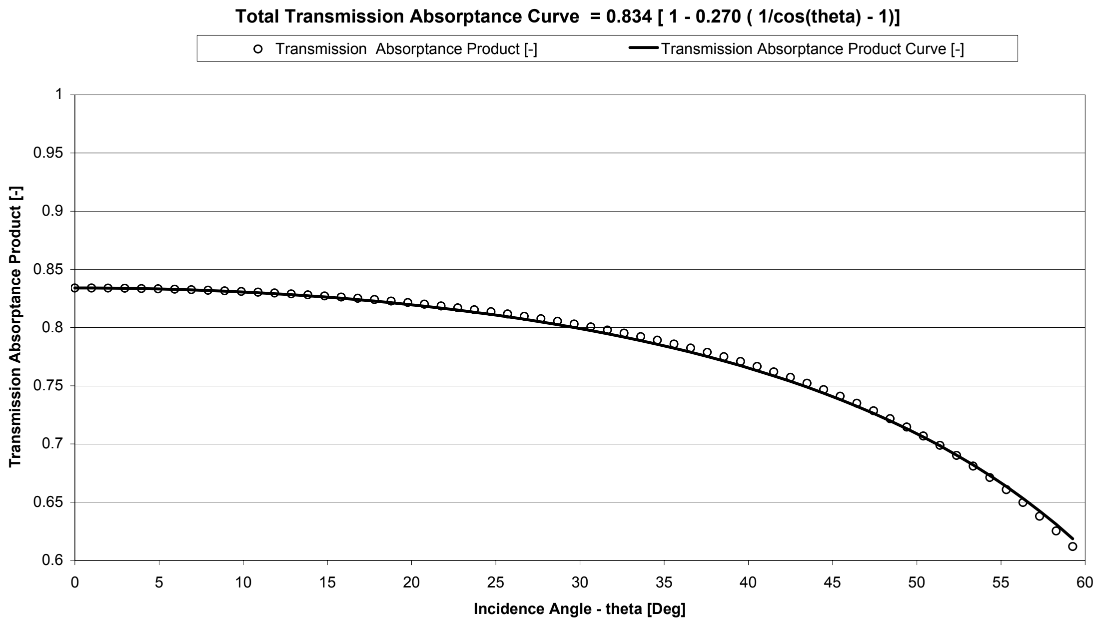

Fig. B.3. Transmission-absorptance product for Hot Harry™ solar water heater.

Note that the plotted transmission-absorptance product is the product of the top cover transmission (= 0.875) and the water chamber absorptance (= $1 - r_1 - 0.84 \times r_2 - 0.42 \times r_3 = 0.951$), where r_1 denotes the reflectance from the upper glass surface (0.043), r_2 the reflectance from the glass-water interface (0.005) and r_3 the reflectance from the water-chamber bottom interface (0.005).

Appendix C

The collector efficiency measured at the Plumbing Testing Laboratory and the corrected efficiency are plotted in Fig. C.1.

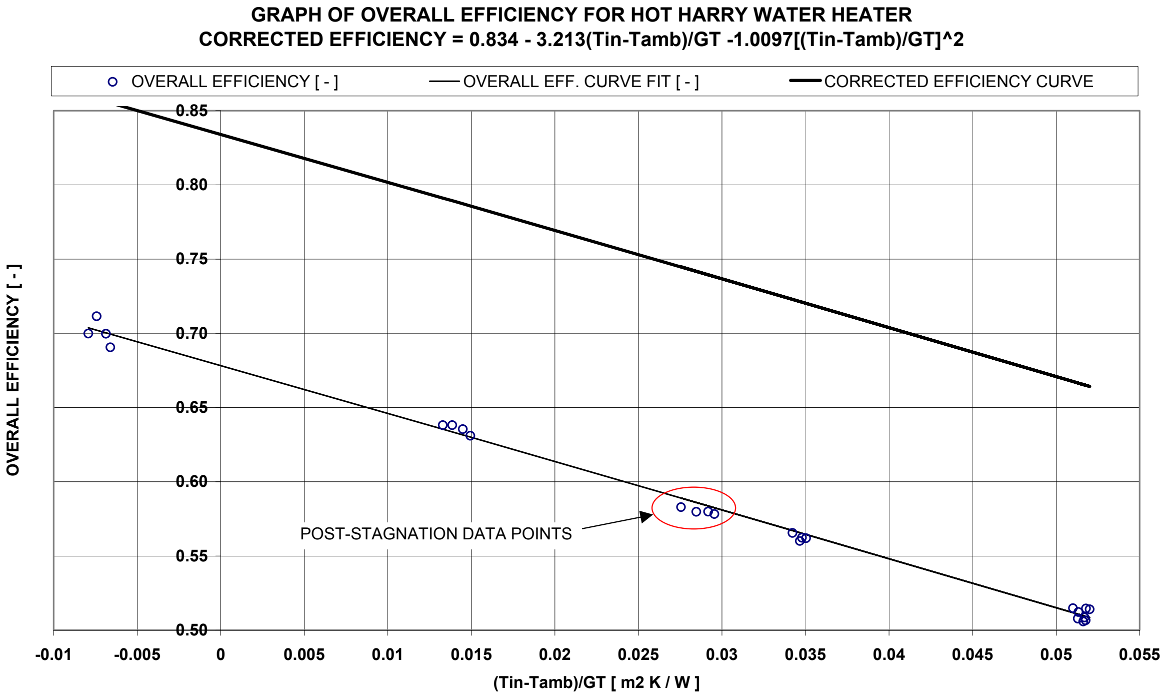

Fig. C.. Overall measured and corrected collector efficiency for Hot Harry Water Heater.

APPENDIX M – Outdoor Collector Testing

Performance Testing of Hot Harry™ Solar Water Heater

Rodney Lowe and Harry Suehrcke

April 2003

1. Description of Experimental Set Up

(a) Outdoor performance test

Daytime performance and heat loss tests of the Hot Harry™ solar water heater were performed at the Gough Plastics factory. In the performance test the heater was placed outdoors and exposed to solar radiation. For this test the heater was tilted 24^o towards North and filled with tap water. Recordings of the quantities listed below were then made with a DataTaker 605 at five minute intervals:

- Solar radiation with a Kipp & Zonen CM 21 pyranometer,
- Ambient air temperature using a type T thermocouple
- Average water temperature inside the storage chamber with type T thermocouples

The outdoor performance test up is shown in Fig. 1.

Fig. 1. Experimental set up for outdoor performance test.

From Fig. 1 the set up of the pyranometer, which was oriented in the plane of the collector, can be seen. Also visible from Fig. 1 is the white Stevenson screen (behind the pyranometer), which contained the thermocouple for the ambient temperature measurement.

The average temperature of heater storage water was measured with three type T thermocouples that were positioned half way between the bottom and top of the storage chamber (see Fig. 2). The three probes provide an accurate average of the water temperature (believed to be better than $0.5^{o}C$) as the water during solar heating becomes fully mixed in vertical direction. The mixing of the storage water can be understood from the fact that a significant portion of the solar radiation is absorbed at the bottom of the storage chamber, which results in the water being heated from below. The mixing in vertical direction also almost eliminates temperature differences in the collector plane as is evident from the experimental data.

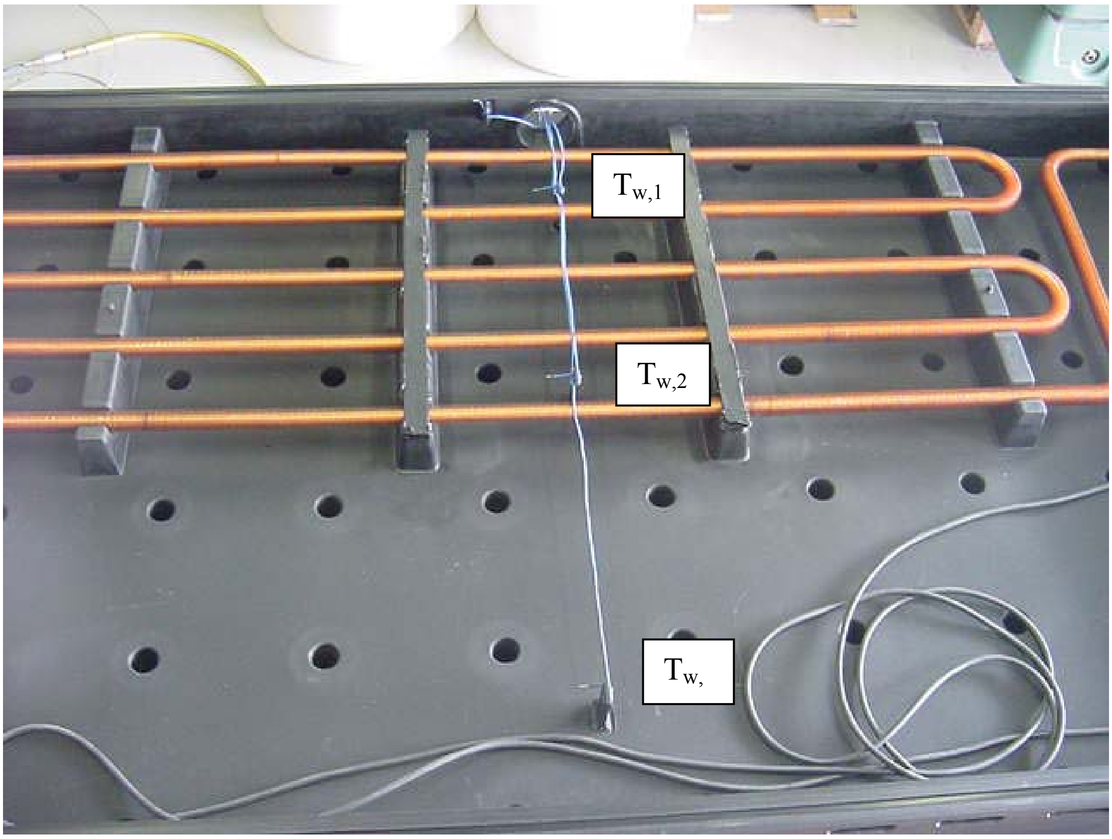

Fig. 2. Thermocouple probes position in heater water storage chamber. (O-ring seal sitting in absorber should have been removed before taking photograph.)

Approximately 200 litres of water was drawn off the collector each afternoon to adequately lower the temperature of the collector as would be the case if the collector would be installed in a domestic household.

(b) Heat loss test

The heat loss test was performed inside a factory shed (see Fig. 3) with the same instrumentation as used in the outdoor performance test. For this test the empty heater was filled via the top vent with water near boiling point. After the heater had been filled, the water was allowed to cool inside the ventilated shed and the (average) water temperature was recorded at 5 minute intervals.

Fig. 3. Experimental set up for indoor heat loss test

2. Data files

One Excel data file with a separate sheet for each day of the outdoor performance test and another file containing the heat loss test data is attached. The experimental data for the outdoor performance test consists of three consecutive days (2 to 4 April 03). The first day (2 April 03) is a partly cloudy day, the second day (3 April 03) is a cloudy day and the third and final day (4 April 03) is a mostly clear day. The data for the heat loss test are for the period 8 to 10 April 03. (not included in this thesis)

3. Test Results

We have performed some evaluation of the test data and hope that a short summary of our results may be useful for comparative purposes.

The heat loss coefficient has been calculated from the water temperature decrease during the heat loss test. For this purpose a mathematical solution for the cooling of a thermal mass of uniform temperature in an ambient with linearly changing temperature has been found. Applying this solution to the fully mixed storage water for every two hourly interval provided the heat loss coefficient U_L as a function of the water to ambient temperature difference (T_w - T_a). The result in $W/m^2.K$ for the first forty hours of the test is:

$U_L = 2.93 + 0.018\ (T_w - T_a)$

Next an Engineering Equation Solver (EES) program was formulated that simulates the water temperature of a heater with fully mixed storage and zero load as a function of time. For this simulation program the above expression of overall heater heat loss coefficient and the below performance parameters as suggested from PTL testing were used:

Collector aperture area: 1.50 m^2

Equivalent thermal water mass: 163.7 kg (see AS2535 HH thermal capacity calculation)

Effective transmittance-absorptance product ($\tau\alpha$) = 0.83

Incidence angle modifier $K_{\tau\alpha} = 1 - 0.27\left(\frac{1}{\cos(\theta)} - 1\right)$

Using the measured solar radiation and ambient temperature as input, simulations were carried out for the time interval 7:30 to 16:30 h except for the last day where the simulation had to be stopped at 16:25 h (due to early load application). The temperatures that were obtained at the end of the time intervals are:

Date	**Simulated**	**Measured**
2 April 03	72.22^{o}C	72.2^{o}C
3 April 03	59.23^{o}C	59.7^{o}C
4 April 03	70.31^{o}C	70.8^{o}C
Average	**67.25^{o}C**	**67.57^{o}C**

Our simulated results are slightly below the experimentally measured results, which suggest that the assumed simulation performance parameters may be conservative. The proposed performance parameters are in good agreement with the results suggested from PTL testing, with the exception the heat loss coefficient shows a stronger temperature dependence (note that the above expression for the heat loss coefficient suggests U_L = 3.47 W/m^2.K when (T_w - T_a) = 30 K). In our opinion the agreement between the model predictions and the measured outdoor performance data strongly supports the proposed correction to the optical efficiency measured at PTL, as set out in our previous correspondence.

APPENDIX N – StandardsMark Approval documents

Content has been removed
for privacy reasons

Content has been removed for privacy reasons

Content has been removed
for privacy reasons

APPENDIX O

Installation and Maintenance Instructions

Content has been removed due to copyright restrictions

PLUMBER'S
INSTALLATION INSTRUCTIONS

Content has been removed
due to copyright restrictions

Installing the Mounting Tray

Content has been removed due to copyright restrictions

Installing the Mounting Tray

Content has been removed due to copyright restrictions

Plumbing Connections

Content has been removed due to copyright restrictions

Plumbing Connections

Content has been removed due to copyright restrictions

Plumbing Connections

Content has been removed due to copyright restrictions

HotHarry

MAINTENANCE INSTRUCTIONS FOR SOLAR PANEL

Content has been removed due to copyright restrictions